iScience

CellPress

Article

Multi-omic Dissection of Oncogenically Active Epiproteomes Identifies Drivers of Proliferative and Invasive Breast Tumors

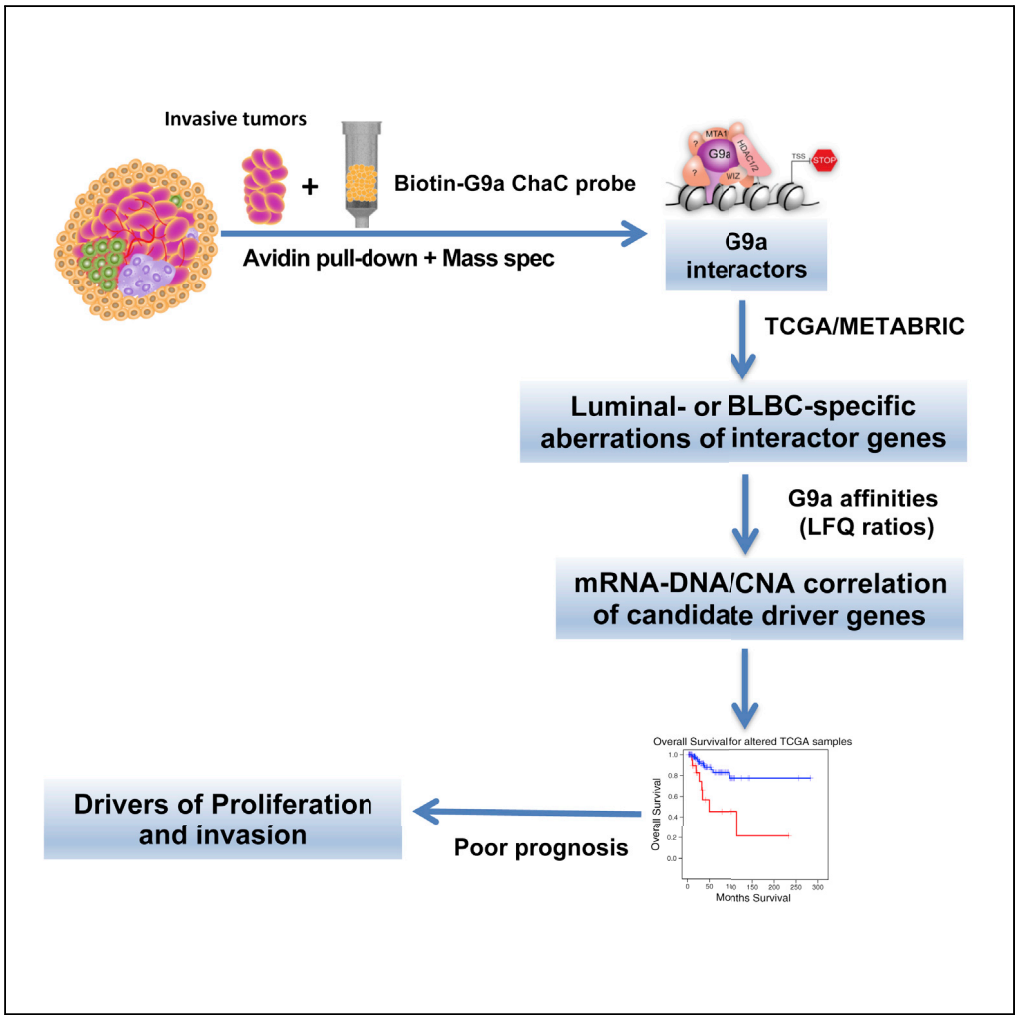

John A. Wrobel, Ling Xie, Li Wang, ..., Jian Jin, Michael L. Gatza, Xian Chen

xianc@email.unc.edu

HIGHLIGHTS

ChaC dissects tumor heterogeneity for identifying oncogenic-active proteins

An oncogenic-active G9a-interactome represents the invasive tumor in a tissue

iC-MAP identifies multi-omics aberrations that drive invasive tumors

Patient-specific iC-MAP of select interactor genes are of prognostic value

Wrobel et al., iScience 17, 359–378
July 26, 2019
https://doi.org/10.1016/j.isci.2019.07.001

iScience

CellPress

Article

Multi-omic Dissection of Oncogenically Active Epiproteomes Identifies Drivers of Proliferative and Invasive Breast Tumors

John A. Wrobel,[1,2,7] Ling Xie,[1,2,7] Li Wang,[1,2,7] Cui Liu,[1] Naim Rashid,[2,3] Kristalyn K. Gallagher,[4] Yan Xiong,[1,2] Kyle D. Konze,[5] Jian Jin,[5] Michael L. Gatza,[6] and Xian Chen[1,2,8,*]

SUMMARY

Proliferative and invasive breast tumors evolve heterogeneously in individual patients, posing significant challenges in identifying new druggable targets for precision, effective therapy. Here we present a functional multi-omics method, interaction-Correlated Multi-omic Aberration Patterning (iC-MAP), which dissects intra-tumor heterogeneity and identifies *in situ* the oncogenic consequences of multi-omics aberrations that drive proliferative and invasive tumors. First, we perform chromatin activity-based chemoproteomics (ChaC) experiments on breast cancer (BC) patient tissues to identify genetic/transcriptomic alterations that manifest as oncogenically active proteins. ChaC employs a biotinylated small molecule probe that specifically binds to the oncogenically active histone methyltransferase G9a, enabling sorting/enrichment of a G9a-interacting protein complex that represents the predominant BC subtype in a tissue. Second, using patient transcriptomic/genomic data, we retrospectively identified some G9a interactor-encoding genes that showed individualized iC-MAP. Our iC-MAP findings represent both new diagnostic/prognostic markers to identify patient subsets with incurable metastatic disease and targets to create individualized therapeutic strategies.

INTRODUCTION

Proliferative and invasive tumors evolve heterogeneously in a tissue microenvironment (Koren and Bentires-Alj, 2015). Such heterogeneity contributes to patient variability in rates of tumor growth, proliferation, metastasis, and susceptibility to anti-cancer therapies (Yates et al., 2015); critically, tumor heterogeneity can mislead diagnosis and treatment. Next-generation sequencing has identified cancer-related genetic alterations (Garnett et al., 2012; Green and Guyer, 2011) that, however, showed low congruence with disease prognosis or diagnosis (Torga and Pienta, 2017). At the transcriptomic level, a 50-gene expression pattern has been created to classify distinct subtypes of breast cancer (BC; PAM50-subtypes), including basal-like/triple-negative (BLBC/TNBC), luminal-A and -B, Her2+, and normal-like BC (Parker et al., 2009). However, these gene-expression signatures are insufficient to discriminate, within single PAM50-subtypes, BC patient subpopulations having different clinical outcomes, particularly subpopulations with highly proliferative and invasive tumors and poor prognosis.

Yates et al. used multi-region genome sequencing to reveal genetic aberrations that define subclonal heterogeneity across different isolates from a single tumor (Yates et al., 2015). To dissect this intra-tumor heterogeneity, substantial efforts, such as xenotransplantation amplification of tumor fractions or genome-wide screening of huge numbers of samples are necessarily employed to identify particular aberrations driving proliferative or invasive subclones (Ng et al., 2016). Gatza et al. introduced an integrated genomics method that identifies drivers of proliferative tumors in luminal BC subtype (Gatza et al., 2014). This approach identifies copy-number aberrations of tumor-essential genes whose subtypic expression patterns correlate with oncogenic pathway activity. A genome-wide RNAi screen further validated these driver genes that are essential for cell viability in an oncogenic pathway-dependent manner. However, these RNAi data that indicated gene-specific effects on BC cell viability were obtained from immortalized cell lines; hence, the data have limited clinicopathological accuracy.

Proteins are the actual disease executors; thus, mass spectrometry (MS)-based quantitative proteomics is widely used to analyze genome-wide, differentially expressed proteins in tumor versus healthy cells. However, the limited sensitivity of MS instruments often yields bulk measurements averaged over different cell

[1]Department of Biochemistry & Biophysics, School of Medicine, University of North Carolina at Chapel Hill, Chapel Hill, NC 27599, USA

[2]Lineberger Comprehensive Cancer Center, School of Medicine, University of North Carolina at Chapel Hill, Chapel Hill, NC 27599, USA

[3]Department of Biostatistics, School of Medicine, University of North Carolina at Chapel Hill, Chapel Hill, NC 27599, USA

[4]Breast Surgical Oncology and Oncoplastics, UNC Surgical Breast Care Program, University of North Carolina at Chapel Hill, Chapel Hill, NC 27599, USA

[5]Mount Sinai Center for Therapeutics Discovery, Departments of Pharmacological Sciences and Oncological Sciences, Tisch Cancer Institute, Icahn School of Medicine at Mount Sinai, New York, NY 10029, USA

[6]Department of Radiation Oncology, Rutgers Cancer Institute of New Jersey, New Brunswick, NJ 08901, USA

[7]These authors contributed equally

[8]Lead Contact

*Correspondence: xianc@email.unc.edu

https://doi.org/10.1016/j.isci.2019.07.001

types in a tissue, obscuring protein changes that precisely define a tumor phenotype. Some researchers employ laser-capture microdissection (LCM) to enrich tumor cells, followed by MS to define the tumor-specific proteome (Liu et al., 2014b). However, the LCM-MS technique is not amenable to routine clinic sampling because processing of small, heterogeneous biospecimens is expensive, low-throughput, and plagued by sample-to-sample variability (Liu et al., 2014b).

Evidently, chromatin state aberrations that stem from complex interactions between gene susceptibility and environmental perturbation drive the heterogeneous evolution of proliferative and invasive tumors (Baker, 2011; Easwaran et al., 2014; Helin and Dhanak, 2013; Wee et al., 2014). During tumorigenesis, the chromatin states associated with particular genes are dynamically regulated in a cell-type-specific manner via interactions with various transcription factors, histone modifiers, chromatin regulators, and chromatin-remodeling enzymes that, together, constitute epigenetic regulatory proteomes (epiproteomes) (Johnson and Dent, 2013). To identify the constituents of these tumor-phenotypic epiproteomes *in situ*, we applied our chromatin activity-based chemoproteomics (ChaC) method (Liu et al., 2014a), a breakthrough functional proteomic technology. ChaC employs UNC0965 (Konze et al., 2014), a biotin-tagged small molecule (Vedadi et al., 2011) that specifically binds the enzymatically active form of the histone lysine methyltransferases G9a and G9a-like protein (GLP). The enzymatic activity of G9a is directly correlated with its oncogenic function in tumor cells (Vedadi et al., 2011; Wozniak et al., 2007), wherein G9a interacts with specific chromatin proteins to drive tumorigenesis (Tu et al., 2018) and metastasis (Dong et al., 2012; Si et al., 2015). Until now, and primarily by clinically incompatible co-transfection and co-immunoprecipitation (IP) approaches, only a few G9a interactors have been characterized, one-gene/protein-at-a-time, for their roles in cancer (Maier et al., 2015; Si et al., 2015). Furthermore, conventional antibody-based immunoprecipitation (IP)-MS approaches (Huttlin et al., 2015; Malovannaya et al., 2011), which capture protein complexes based on epitope abundance, cannot discriminate IP complexes from tumor and non-malignant cells in a tissue. Our G9a ChaC probe UNC0965 is superior to any antibody-dependent, abundance-based IP approaches because it enables a specific, one-step sorting of the protein complexes associated with oncogenically active G9a/GLP separate from less enzymatically active G9a in other cell types in a tissue, especially non-malignant cells. ChaC-MS analysis revealed that the compositions of UNC0965-captured epiproteomes represent the proliferative or invasive potential of a patient tissue. For the first time, with higher sensitivity, specificity, and reproducibility, and directly from clinical specimens, ChaC identified multiple G9a-interacting proteins that function in concert as candidate tumor-phenotypic determinants or drivers.

Despite this advance, current search engines for MS data-dependent protein identification use only one individual's genomic sequence as Ref-seq, so that information about individual patient's (*individualized*) protein aberrations is missing for all ChaC MS-identified G9a/GLP interactors. Conversely, genome-wide studies of two large BC patient cohorts, TCGA (Ciriello et al., 2015) and METABRIC (Molecular Taxonomy of BC International Consortium) (Curtis et al., 2012), have correlated *individualized* transcriptomic/genomic aberrations with clinical/pathological data from >2,600 patients with BC. *To identify which G9a/GLP interactors possess the characteristics of the individual patients with proliferative or invasive tumors,* we retrospectively analyzed (Wang et al., 2018) both TCGA and METABRIC data to identify individualized aberrations of genes that encode luminal- or BLBC-specific G9a/GLP interactors. We then identified particular G9a/GLP interactor genes that showed individualized interaction-Correlated Multi-omic Aberration Patterning, or iC-MAP, in which the G9a/GLP affinities of these UNC0965-captured proteins correlate with genomic or/and transcriptomic aberrations of their encoding genes. Kaplan-Meier (KM) survival analyses further distinguished, from >18,000 genes, patient mRNA overexpression patterns or copy-number aberrations of those interactor genes that are of prognostic value. As a result, particular interactor genes that were amplified uniquely in highly proliferative luminal patients or patients with invasive BLBC/TNBC were identified as determinants or drivers of proliferation or invasion based on their G9a/GLP affinity-correlated alterations in mRNA expression, DNA copy numbers, and/or proliferation score in patient subsets with poor prognosis. This ChaC-based iC-MAP paradigm is generally applicable to dissect *real-time* heterogeneity of any tumor types and identify *in situ* tumor-phenotypic drivers (proteins) that represent individualized diagnostic/prognostic markers and new druggable targets.

RESULTS

iC-MAP Identifies Drivers of Proliferative and Invasive Breast Tumor

As shown in Figure 1A, ChaC with UNC0965 sorts *in situ* and identifies candidate drivers in their oncogenically active states, i.e., within G9a/GLP-interacting epiproteomes, directly from patient tissues without

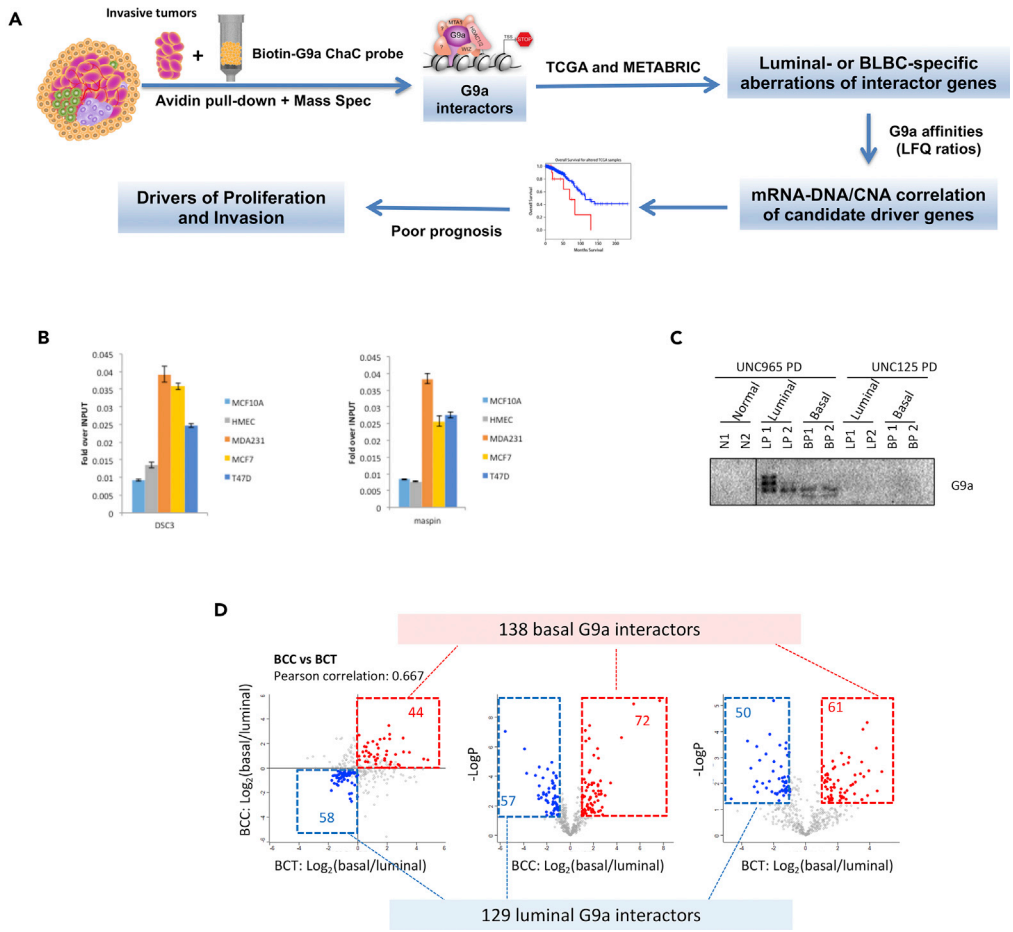

Figure 1. Dissection of the Tumor-phenotypic Heterogeneity by iC-MAP

(A) Schematic iC-MAP design. "CNA" refers to copy-number amplifications.

(B) UNC0965-precipitation-PCR shows that, in different BC subtypes, G9a/GLP is *differentially* enriched or activated in the chromatin associated with tumor suppressor genes *DSC3* (left) and *maspin* (right). UNC0965 pulls down the enzymatically active G9a/GLP with associated DNA. qPCR indicates the differentially active G9a in different BC subtypes and the G9a methylation activity is gene specific.

(C) Immunoblotting analysis of G9a abundance in the protein mixture captured by UNC0965 or the G9a-negative probe UNC125 in the adjacent non-malignant ("N") tissue versus tumor tissues of either luminal (Lum "LP") or basal (BLBC "BP") patients.

(D) Gene-specific G9a/GLP epiproteomes are differently assembled in different BC PAM50 subtypes. BCC, breast cancer cells; BCT, breast cancer tissues. (Left) A plot of basal/luminal LFQ ratios of UNC0965-captured proteins from the BCCs versus BCTs of similar PAM50 subtypes. (Middle and right) The volcano plots of the interactors identified in a series of BCC lines and BCTs showing either BLBC/basal- or luminal-specific UNC0965/G9a affinities correlated with the log2 LFQ ratios (basal-like/luminal) normalized against the ratios from adjacent non-malignant tissues. Proteins that show log2 LFQ ratios >1 or < −1 and -log10 p value >1 are putative BC subtypic interactors of statistical significance.

See also Figures S1 and S2; Tables S1–S4.

diluting information about proliferation lesions or tumor invasiveness. We compared multiple BC cell lines and primary tissues of similar PAM50 subtypes to determine the specificity of UNC0965 (Konze et al., 2014) in dissecting the intra-tumor heterogeneity, i.e., sorting an oncogenically active G9a/GLP-interacting epiproteome from a heterogeneous tissue. Following label-free quantitation (LFQ)-based MS characterization of the composition of UNC0965-captured epiproteomes, we applied the Perseus method (Tyanova et al., 2016) that has built-in multiple testing to determine statistically significant LFQ ratios (FDR <0.05); PAM50-subtypic G9a/GLP interactors are those that show quantitatively correlated LFQ ratios in protein affinities to G9a/GLP regardless of the prevalence of a phenotype in a heterogeneous tissue or in a homogeneous cell line. Next, we used TCGA (Ciriello et al., 2015) and METABRIC patient databases to retrospectively

identify personal proteo-transcriptomic and proteo-genomic links (Wang et al., 2018) for the genes PAM50-subtypic G9a/GLP interactor genes. PAM50-subtypic drivers of proliferative or invasive breast tumors were identified as interactor genes that showed correlated multi-omics aberrations in, e.g., mRNA expression, DNA copy numbers, and/or proliferation score in patient subsets with poor prognosis.

The G9a ChaC Probe Captures BC Subtypic G9a Interactors

We first determined the genomic occupancy of the G9a/GLP-interacting epiproteomes in different BC PAM50 subtypes. We used UNC0965 (Konze et al., 2014) immobilized on NeutrAvidin agarose beads to capture the G9a epiproteomes and their bound DNA elements from non-malignant (HMEC or MCF10A), the PAM50 luminal-subtype (T47D or MCF7), and the basal-like subtype (MDA231) BLBC cell lines. We did not detect any differences for capture using a G9a/GLP-negative probe (UNC125). However, compared with non-malignant mammary cells, PCR amplification of the UNC0965-captured genes revealed that G9a was specifically enriched within the chromatin of tumor suppressor genes, such as DSC3 and maspin, in the malignant/tumor cells, and more so in the basal subtype (Figure 1B). Thus, the methylation/enzymatic activity of G9a/GLP *differs* within the chromatin of genes that show differential expression in either non-malignant versus malignant cells or in different BC subtypes. This result agrees with previous findings. DSC3 is an anti-metastatic tumor suppressor with significantly diminished expression in breast tumor cells (Oshiro et al., 2005), as its associated chromatin had increased CpG DNA methylation and H3K9me2 catalyzed by the heterodimer G9a/GLP complex (Vedadi et al., 2011; Wozniak et al., 2007). Maspin inhibits invasiveness and motility of mammary carcinoma (Wu et al., 2010). The maspin gene also carried pronounced H3K9me2 in MDA231 but not in the non-malignant HuMEC (Wozniak et al., 2007). These results indicated that (1) in malignant or invasive BC subtype, G9a/GLP is more oncogenically active or more enriched in the transcriptionally silenced chromatin of tumor suppressor genes and (2) UNC0965 can pull down the oncogenically active G9a/GLP and associated protein complexes specifically from the chromatin harboring aberrantly silenced genes in distinct tumor phenotypes; ignored are the same genes in other chromatin states in non-malignant cells or in other cell types.

We then compared the composition of the UNC0965-captured epiproteomic complexes from a cell line series containing homogeneous representatives of nonmalignant mammary epithelial cells (HuMEC or MCF10A), PAM50-luminal (BT474, T47D, and MCF7), and PAM50-BLBC (MDA231, HCC1806, and SUM159) subtypes. To ensure that our ChaC scheme is readily applicable to any clinical specimen, we coupled on-beads sampling/processing with LFQ, so that all ChaC experiments were performed on a clinical sample scale of 60–100 μg total protein mass per nLC-MS/MS run. Following repeated washing to remove non-specific proteins, and on-beads tryptic digestion, we performed nLC-MS/MS experiments on each UNC0965 pull-down for two to three biological replicates, each with three technical replicate runs. In each UNC0965 pull-down from a PAM50 subtype, G9a and GLP were unambiguously identified by 30–50 unique MS/MS-sequenced peptides. To distinguish genuine G9a-interacting epiproteomic components, we filtered non-specific associates by comparing the proteins captured by UNC0965 with proteins acquired in UNC125 or mock pull-downs (empty NeutrAvidin beads). The LFQ ratios (peak intensities) of proteins in the UNC0965-captured complexes from any paired cell line correlated with the relative G9a/GLP affinities of these proteins in these cell types. Based on their affinity-correlated LFQ ratios, we identified major clusters of G9a/GLP-associated proteins that had significantly increased affinities to UNC0965 and no binding to empty beads (Figure S1A and Table S1). With respect to their associations with UNC0965 in the non-malignant cells, the majority of UNC0965-captured proteins showed quantitatively correlated G9a/GLP affinities in similar luminal- or BLBC-subtypic cell lines, i.e., the LFQ ratios of these proteins were correlated in MCF7 versus T47D or in MDA-MB-231 versus SUM159 (Pearson correlation coefficient 0.73), indicating that the G9a/GLP-interacting epiproteomes are assembled in a BC-subtypic manner (Figure S1B, Table S2). Among these ChaC-identified proteins, we found many known components of multiple epiproteomic complexes (Ooi and Wood, 2007, Shi et al., 2003, Wilson and Roberts, 2011, Ahringer, 2000). Also, in agreement with a previous report (Si et al., 2015), we found that GATA3 enhanced its interaction with G9a in luminal BC cells, whereas MTA2 was associated with G9a more specifically in BLBC cells. By identifying these chromatin regulatory complexes known to be associated with G9a, we demonstrated the specificity of UNC0965 in capturing endogenous G9a epiproteomes assembled into gene-specific, oncogenically silenced chromatin characteristic of different BC subtypes. Technically, the gene specificity of UNC0965-captured epiproteomic complexes renders ChaC superior to any abundance-based IP-MS approaches (Huttlin et al., 2015; Malovannaya et al., 2011).

ChaC-MS Identifies *In Situ* Oncogenic-active G9a Interactors Critical for Tumor Cell Viability

To confirm the unique ability of ChaC to sort and characterize a pathologically relevant, G9a-associated epiproteome whose composition defines the predominant tumor phenotype in a heterogeneous tissue, we performed similar cross-referencing LFQ experiments (Wang et al., 2018) with ChaC and various PAM50-subtypes from different sample types, i.e., cell lines and tissues. These samples included the aforementioned cell line series plus four frozen clinical specimens including tumor tissues with molecular classifications of similar PAM50 subtypes (and adjacent nonmalignant tissue).

In the UNC0965-captured protein complexes we observed higher G9a abundance in luminal or basal patients, whereas no G9a was detected by immunoblotting against G9a antibody in either adjacent non-malignant tissue or the protein mixtures that were pulled down by the G9a-negative probe UNC125 (Figure 1C). These results confirmed that UNC0965 pulls down specifically G9a/GLP and its activity-based interactors in the proliferative or the invasive tumor cells, avoiding other cell types or non-malignant cells in which G9a is less enzymatically active.

LFQ ratios are proportional to the G9a/GLP affinities of the captured proteins. Thus, the UNC0965-captured proteins that show cross-referenced LFQ ratios among cell lines versus tissues, or among tissues of similar PAM50 subtypes (Wang et al., 2018), should be the G9a/GLP-interacting proteins characteristic of tumor cells that are the predominant population. Accordingly, we used the Perseus method (Tyanova et al., 2016) to analyze the PAM50-subtypic compositions of UNC0965-captured epiproteomes. Among 294 proteins in common in all cell lines (n = 6) (Table S3) and tissues (n = 4) (Table S4, Figure S2A), with three liquid chromatography-tandem mass spectrometry (LC-MS/MS) technical replicates for each of two biological replicates, 154 UNC0965-captured proteins showed similar, statistically significant G9a/GLP affinities in the tissues versus the cell lines of similar PAM50 subtypes, with respect to either non-malignant MCF10A or non-malignant tissues. As indicated by the LFQ ratios that correlated across both cell line and tissue origin (Pearson correlation coefficient at 0.66) (Figure 1D, left), one luminal-specific cluster of eighty-four proteins (Figure 1D, left, lower-left quadrant) showed increased UNC0965 affinity specifically in the luminal subtype but decreased affinity in the BLBC subtype; another BLBC-specific cluster of seventy proteins showed an opposite UNC0965-binding pattern (Figure 1D, left, upper-right quadrant). In a high confidence with false discovery rate of <5%, we identified fifty-eight luminal (Figure 1D, left, blue dots) and forty-four BLBC (Figure 1D, left, red dots) G9a/GLP interactors. Thus, the PAM50-subtypic G9a affinities of many epiproteomic components were consistently preserved, representing the predominant tumor phenotype, with minimum sample-to-sample variability, in both homogeneous cell lines and heterogeneous clinical tissues. Also, by LFQ-assisted LC-MS/MS, the compositions of G9a/GLP interactomes were identified with PAM50-subtypic characteristics, i.e., G9a/GLP interacts with subtype-unique chromatin proteins in different BC subtypes.

Bypassing tedious LCM tumor cell sorting or xenotransplantation, UNC0965 can sort/enrich *in situ* the oncogenically active G9a/GLP interactors that represent a single, predominant tumor phenotype in a heterogeneous tissue. Thus, ChaC exhibits high pathological accuracy in identifying candidate oncogenic drivers. Based on statistically significant LFQ ratios that correlated with increased UNC0965 binding of MS-identified proteins, we identified 138 BLBC/basal and 129 luminal G9a interactors (Figure 1D). Functional category/network analysis revealed that these BC-subtypic G9a interactors over-represented major pathways/sub-networks associated with RNA processing, translation initiation and elongation, ribosome biogenesis, RNA splicing, and RNA metabolism, consistent with the view that these interactors are candidate drivers of tumor growth and proliferation/invasion (Figure 2). Lastly, results of immunoblotting experiments were consistent with MS/MS experiments, i.e., we compared the level of UNC0965-captured G9a/GLP from different BC subtype cell lines versus HuMEC. UNC0965 pull-downs from equal amounts of each cell line had higher amounts of G9a(EHMT2)/GLP(EHMT1) in either the basal (long or short forms of G9a/GLP) or the luminal subtypes compared with HuMEC cells for which no G9a/GLP was detected (Figure S2B). Also, no UNC0965/G9a-interacting proteins were detected in the UNC125-captured protein mixtures.

Identification of Oncogenic-active G9a Interactors with Multi-omics Aberrations

Using TCGA (Ciriello et al., 2015) and METABRIC (Curtis et al., 2012; Pereira et al., 2016) databases, we analyzed the *individualized* frequency of various types of patient-specific aberrations of genes that encode PAM50-subtypic G9a interactors. These datasets contain two large independent cohorts of >2,600 patients with five subtypes classified by PAM50 (Parker et al., 2009) and information about mutations, copy-number

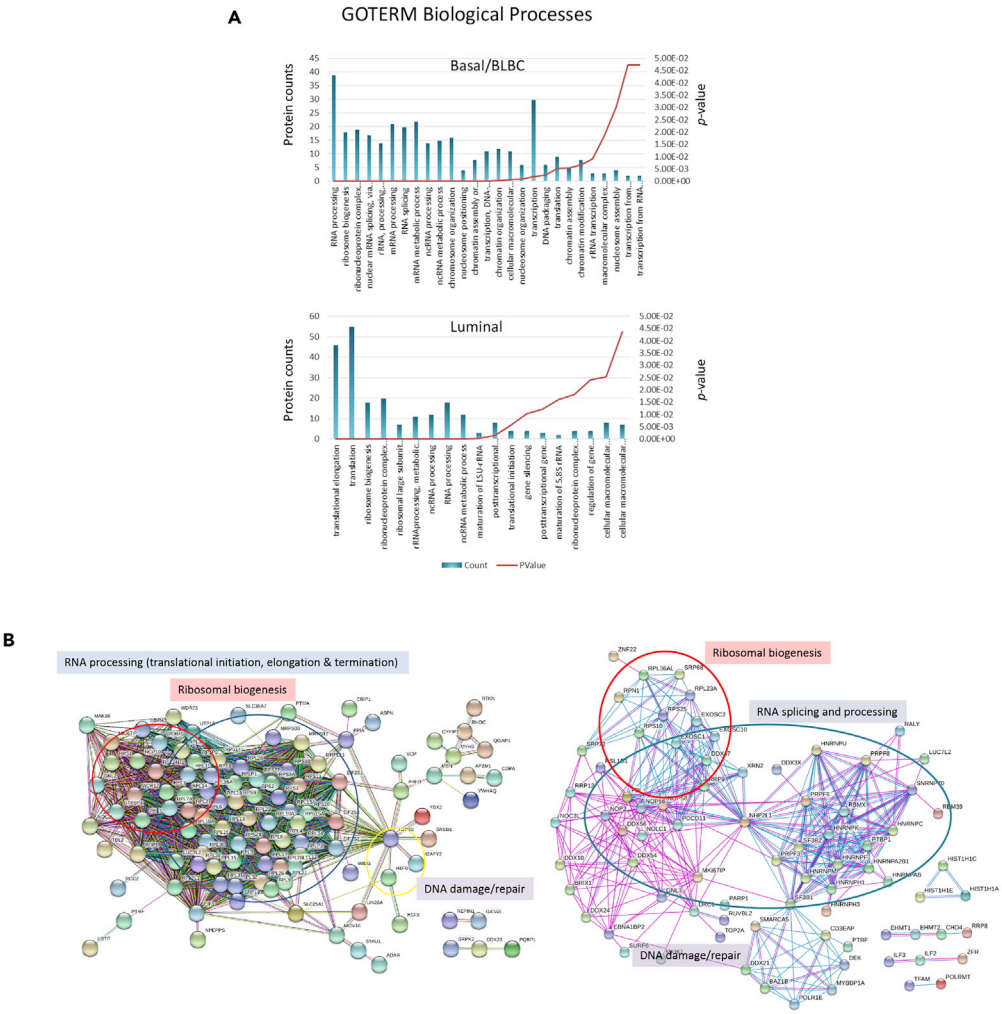

Figure 2. Functional Category/Network Analysis of BC-subtypic G9a Interactors

(A) Functional categorization of luminal- or BLBC-specific G9a interactors.

(B) STRING network involving the proteins showing luminal- (left) or Basal/BLBC (right)-specific enhancements in their affinities to G9a (luminal or BLBC/basal G9a interactors).

aberrations, mRNA expression, and associated clinical/pathological data (stages/grades and relapse status). The TCGA project analyzed 816, mainly American, patients with BC with 590 luminal A/B subtypes and 136 BLBC/TNBC subtypes. The METABRIC database contains 1866 Canadian and European patients with BC with 1,127 luminal A/B subtypes and 198 BLBC/TNBC subtypes.

First, we found that the mutation frequencies for most interactor genes were extremely low in the TCGA patient pool, i.e., less than 5% of patients with BC had somatic mutations in G9a interactor genes, except for *GATA3* (Table S5). Clearly, somatic mutations had little impact on the oncogenic activities of G9a interactors.

Next, we compared the mRNA expression of interactor encoding genes (downloaded as *Z* score values from the cBioPortal for Cancer Genomics: http://www.cbioportal.org/) between BLBC/basal and luminal A/B TCGA patients (Ciriello et al., 2015) by performing a Mann-Whitney-Wilcoxon Test to judge the expression differences between the two PAM50 subtypic populations. This test was performed on all genes in the dataset for comparisons, and we used the Benjamini Hochberg procedure to adjust p values for multiple testing. By this multi-testing scheme, an interactor was classified as BLBC/basal if its expression level was

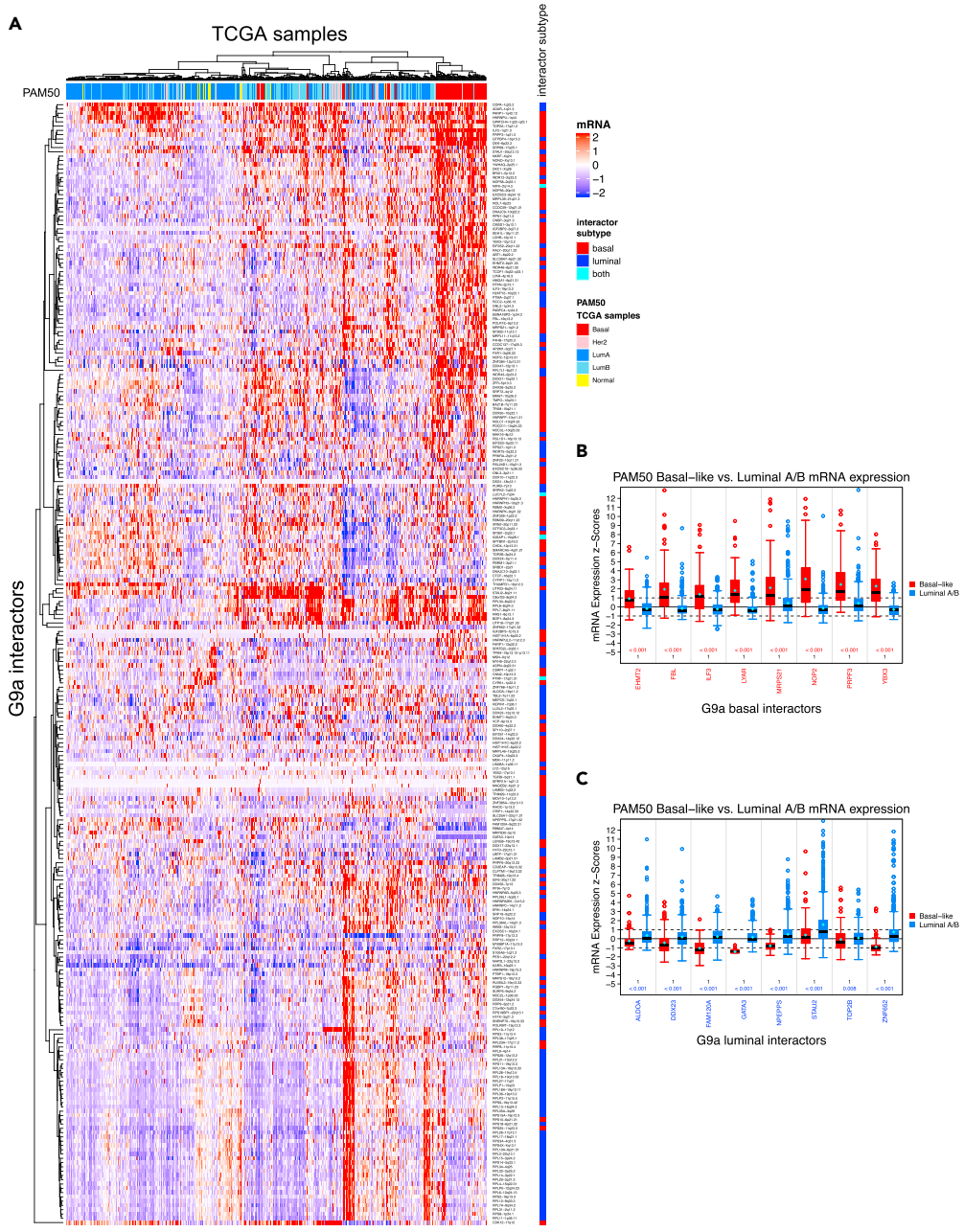

Figure 3. Genes that Encode PAM50-subtypic G9a Interactors Show Statistically Significant Overexpressed mRNA

The expression values for the PAM50-subtypic G9a interactor genes were obtained from the cBioPortal (mRNA expression Z scores compared with diploid tumors) for all TCGA BRCA patients.

(A) Heatmap for G9a interactor genes (rows) with mRNA expression from the TCGA sample set (columns). The TCGA samples and G9a interactor genes were clustered using unsupervised hierarchical clustering ("euclidean" distance and "ward" clustering method). The columns are annotated with PAMA50 subtype of each TCGA patient. The rows are annotated with the proteomic subtype of G9a interactors.

(B and C) Box plots showing the statistically significant altered mRNA expression (x axis) for a sample set of basal G9a interactor genes (B) and a sample set of luminal G9a interactor genes (C). For each interactor gene, the distribution of mRNA expression for PAM50 basal-like TCGA patients (N = 136) is shown on the left in red, and for PAM50 luminal A and B patients (N = 560) it is shown on the right in blue. Outliers are indicated as circles. The median is indicated by the black bar inside each box. The mean is indicated by the cyan diamond. The mRNA expression as a *Z* score is displayed on the y axis. A Mann-Whitney-Wilcoxon Test was performed on each pair to judge differences in expression levels.

Figure 3. *Continued*
This Mann-Whitney-Wilcoxon Test was performed on all genes in the TCGA dataset (n = ~18,000), and the resulting p values were adjusted for multiple comparisons. Adjusted p values are displayed above the x axis for basal-like samples having greater expression (top line) and luminal samples having greater expression (bottom line). Adjusted p values < 0.05 are red if expression is higher for basal-like and blue if expression is higher for luminal samples. Figure S3 shows the iCEP box plots for the complete set of basal G9a interactors. Figure S4 shows the iCEP box plots for the complete set of luminal G9a interactors.
See also Figures S3 and S4; Tables S5 and S6.

significantly greater (adjusted p value < 0.05) for the basal patients. Likewise, an interactor was classified as luminal if its mRNA expression level was statistically greater for the luminal patients (adjusted p value < 0.05).

From a systems view, hierarchical clustering resulted in patient-specific mRNA expression patterns for all PAM50-subtypic G9a interactors in TCGA patients (Figure 3A). We found a similar statistically significant interaction-correlated expression pattern (iCEP) (Wang et al., 2018) wherein the PAM50-subtypic G9a/GLP binding of some UNC0965-captured proteins showed *cis*-mRNA expression of the genes encoding these interactors in patients with the corresponding PAM50 subtypes (Table S6). Briefly, 94 of 138 BLBC/basal G9a interactors showed basal iCEPs in the TCGA patients, including 77 interactors (82%) that displayed basal iCEPs in both TCGA and METABRIC patients (Figures 3B and S3). Conversely, among 129 luminal G9a interactors, only twenty-nine showed iCEPs across various luminal subtypes (Figures 3C and S4), whereas sixty-eight had higher expression in patients with BLBC. Notably, it is not surprising to observe fewer luminal interactor genes with statistically significant iCEPs because, compared with BLBC/basal subtypes, there are more diverse receptor-based luminal subtypes, including luminal-A and luminal-B. Nevertheless, the patient mRNA overexpression pattern of G9a/GLP interactor genes automatically clustered patients with BC (TCGA and METABRIC) based on the PAM50-classified subtypes for which these interactors were identified, confirming the pathological accuracy of UNC0965 in sorting the predominant tumor phenotype in a tissue. Importantly, our iCEP findings demonstrated that ChaC discovers the interactor-encoding genes as new BC-subtypic classifiers, i.e., these genes are fully translated into oncogenically active G9a/GLP interactors in a PAM50-subtypic manner.

We then examined the PAM50 subtype distribution of copy-number alterations in the G9a interactor genes in the TCGA patient sets. Particularly, we performed a correlation analysis comparing increased mRNA expression with copy-number amplification of all G9a interactor genes. The mRNA expression (as *Z* score values) and copy-number (as GISTIC values) data were downloaded from the cBioPortal for Cancer Genomics (http://www.cbioportal.org/) (Cerami et al., 2012; Gao et al., 2013). Based on copy-number status, we separated the TCGA samples into a deletion/diploid group (GISTIC values of 0, -1, or -2) and a gain/amplification group (GISTIC values of 1 or 2). We performed a Mann-Whitney-Wilcoxon Test to judge whether the mRNA expression values were greater for the gain group compared with the deletion/diploid group. This test was performed on over 18,000 genes (with both mRNA expression and GISTIC data), and p values were adjusted for multiple testing using the Benjamini Hochberg procedure. We identified 110 luminal and 117 BLBC/basal interactor genes that showed significant correlations between mRNA overexpression and copy-number gain/amplification in TCGA luminal A/B (n = 590) or basal samples (n = 136) (adjusted p value < 0.05, Table S7).

Identification of Tumor-proliferative G9a Interactors with Multi-omics Aberrations

Because proliferation is a luminal BC characteristic, we next searched for G9a interactors bearing mRNA-expression or DNA copy-number aberrations that are characteristic of proliferative tumors. Using the proliferation scores of individual patients recruited for the TCGA BRCA study (Ciriello et al., 2015) we performed a correlation analysis of PAM50-subtypic interactors, comparing mRNA expression with the tumor proliferation scores for luminal A/B (n = 590) and basal patients (n = 136). We separated the TCGA samples into high-proliferation-score (top 25%) and low-proliferation-score (bottom 75%) groups. A Mann-Whitney-Wilcoxon Test was used to judge whether the mRNA expression values were greater for the high-proliferation-score group compared with the low-proliferation-score group. This test was performed on over 18,000 genes, and p values were adjusted for multiple testing using the Benjamini Hochberg procedure. We identified forty-five luminal and twenty-three basal interactor genes that showed significant correlations between increased mRNA expression and a high proliferation score (adjusted p value < 0.05, Table S8).

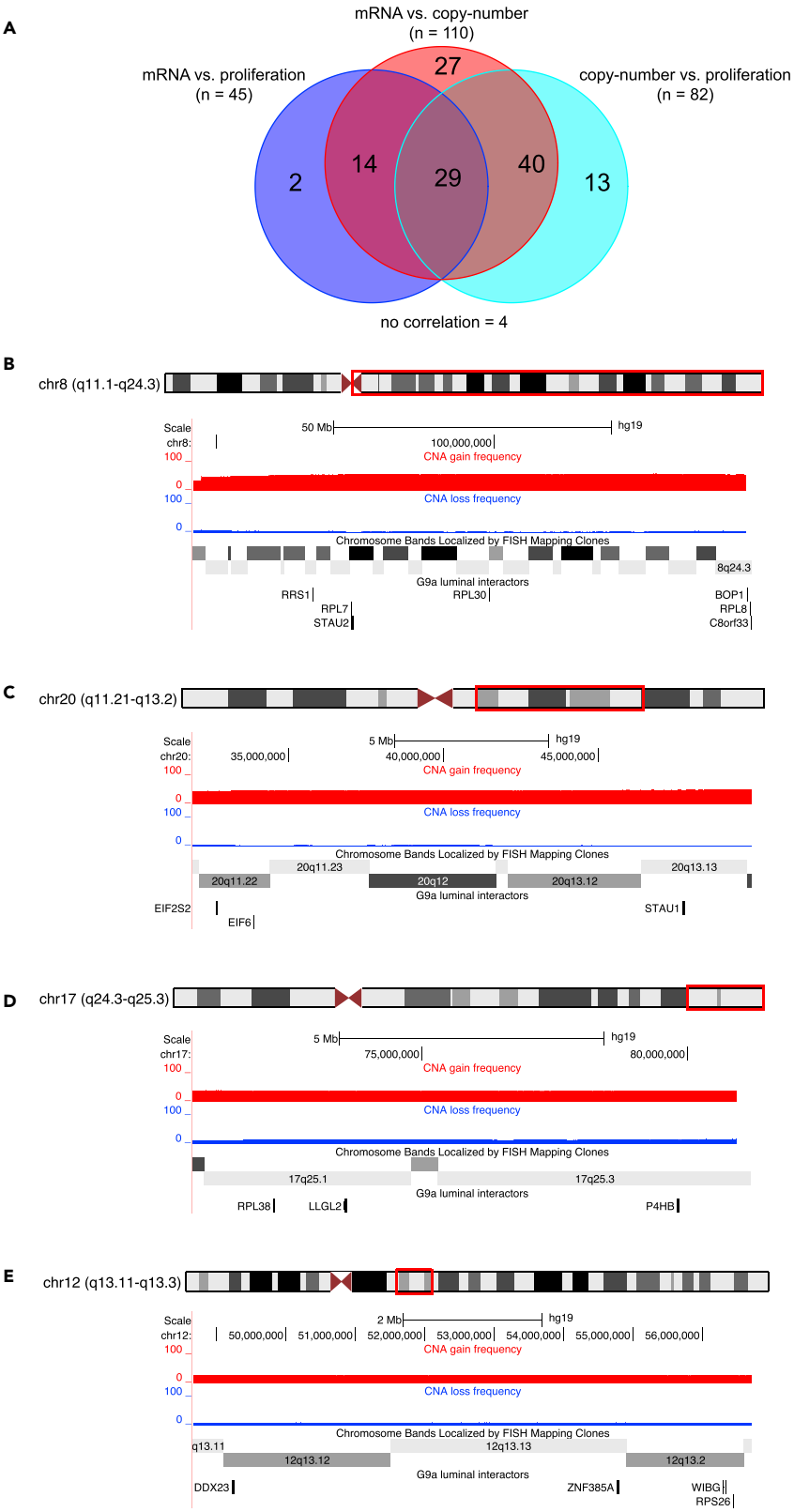
A
mRNA vs. copy-number
(n = 110)
mRNA vs. proliferation
(n = 45)
copy-number vs. proliferation
(n = 82)
27
14
29
40
2
13
no correlation = 4
B
chr8 (q11.1-q24.3)
Scale
chr8:
50 Mb
hg19
100,000,000
CNA gain frequency
CNA loss frequency
Chromosome Bands Localized by FISH Mapping Clones
8q24.3
G9a luminal interactors
RRS1
RPL7
STAU2
RPL30
BOP1
RPL8
C8orf33
C
chr20 (q11.21-q13.2)
Scale
chr20:
5 Mb
hg19
35,000,000
40,000,000
45,000,000
CNA gain frequency
CNA loss frequency
Chromosome Bands Localized by FISH Mapping Clones
20q11.23
20q13.13
20q11.22
20q12
20q13.12
G9a luminal interactors
EIF2S2
EIF6
STAU1
D
chr17 (q24.3-q25.3)
Scale
chr17:
5 Mb
hg19
75,000,000
80,000,000
CNA gain frequency
CNA loss frequency
Chromosome Bands Localized by FISH Mapping Clones
17q25.1
17q25.3
G9a luminal interactors
RPL38
LLGL2
P4HB
E
chr12 (q13.11-q13.3)
Scale
chr12:
2 Mb
hg19
50,000,000
51,000,000
52,000,000
53,000,000
54,000,000
55,000,000
56,000,000
CNA gain frequency
CNA loss frequency
Chromosome Bands Localized by FISH Mapping Clones
q13.11
12q13.13
12q13.12
12q13.2
G9a luminal interactors
DDX23
ZNF385A
WIBG
RPS26

Figure 4. G9a Interactor Genes Found with Highly Frequent Copy-number Amplifications

(A) Venn diagram showing overlap of mRNA versus copy number, mRNA versus proliferation, and copy number versus proliferation correlations for the 129 luminal G9a interactors. UCSC Genome Browser views of four examples of clusters of luminal G9a interactors located in amplified chromosomal regions in TCGA luminal patient samples: (B–E) (B) *RRS1, RPL7, STAU2, RPL30, BOP1, RPL8,* and *C8orf33* on the q arm of chromosome 8; (C) *EIF2S2, EIF6,* and *STAU1* on the q arm of chromosome 20; (D) *RPL38, LLGL2,* and *P4HB* on the q arm of chromosome 17; (E) *DDX23, ZNF385A, WIBG,* and *RPS26* on the q arm of chromosome 12. For each view, the frequency of luminal TCGA samples with copy-number gain (segmentation mean >0.1) (red) and copy-number loss (segmentation mean < −0.1) (blue) is indicated.
See also Figure S5; Tables S7, S8, S9, and S10.

Similarly, by performing a Fisher's Exact Test for Count Data, we identified eighty-two luminal interactors that had a statistically significant correlation between copy-number amplification (CNA) and a high proliferation score (adjusted p value < 0.05, Table S9). We did not find any basal interactors with significant correlation between copy-number amplification and proliferation score. Because a strong basal-specific iCEP was observed for most of basal interactors, we reasoned that mRNA over-expression of basal interactor genes is the primary driver of proliferation/invasion in basal patients.

Drivers of Proliferative Luminal Tumors Have Multi-omics Aberrations in Patients with Poor Prognosis

Because patients with proliferative or invasive tumors often have poor prognosis, we performed the KM survival analysis to determine prognosis for patients whose luminal G9a interactor genes showed both CNA (a GISTIC score of 1 or 2) and mRNA overexpression (a *Z* score of mRNA expression in the top 50%) that correlated with high proliferation scores. The statistically significant overall survival was determined by a p value and hazard ratio. We identified (Figure 4A) twenty-nine luminal interactor genes with proliferation-correlated CNA and mRNA over-expression. Among these genes, *C8orf33, EIF2S2*, and *EIF6* were also found in the RNAi dataset of genes essential for luminal cell line viability. *EIF2S2* and *EIF6* are essential genes of proliferative luminal breast tumors (Gatza et al., 2014). To identify new driver genes that are amplified uniquely in proliferative luminal tumors, we investigated which interactor genes are located in genomic regions with increased amplification frequency and have a coordinate increase in mRNA expression in patients with poor prognosis. For example, seven luminal interactors with multiple correlations (Figures 5A and S6) were found on the q arm of chromosome 8 with copy-number amplification frequencies of 51%–56% (Figure 4B, Table S10). Specifically, *C8orf33, BOP1*, and *RPL8* are located at 8q24.3, *RPL7 and STAU2* at 8q21.11, *RRS1* at 8q13.1, and *RPL30* at 8q22.2. *RPL7* and *STAU2* are near each other, separated by one gene (Figure S5). Patients with copy-number amplifications for all of these individual genes with proliferation-multi-omics correlations (Figures 5A and S6) have poor overall survival in TCGA and/or METABRIC (p values ranging from 0.001 to 0.068) (Figures 6A and S7, Table S11). Patients with *STAU2* mRNA overexpression in both TCGA and METABRIC (Figure 6A) have poor survival. mRNA overexpression of *C8orf33* in TCGA (no data in METABRIC) indicates poor survival. Patients with mRNA overexpression of *RRS1, RPL8,* and *BOP1* have poor survival in METABRIC (Figure S8, Table S12).

EIF2S2 and *EIF6* are located at 20q11.22 with copy-number amplification frequencies of 40% and 43%, whereas *STAU1* is located at 20q13.13 with an amplification frequency of 46% (Figure 4C, Table S10). Of particular interest, both *EIF2S2* and *EIF6* are essential for cell proliferation (Gatza et al., 2014). These individual genes have poor survival for METABRIC patients with correlations between CNA and mRNA overexpression (Figures 5B, 6B, and S9–S11, Tables S11 and S12). mRNA overexpression of *EIF2S2* also showed a statistically significant (p value = 0.046) poor prognosis for TCGA patients.

Also, METABRIC patients with poor prognosis associated with copy-number amplifications (p value ranging from 0.049 to 0.059) possessed three luminal interactor genes (RPL38, LLGL2, P4HB) that had all correlations and were located at 17q25 with CNA frequencies of 35%–36% (Figures 4D, 5C, 6C, and S12–S14, Tables S10, S11, and S12). In addition, poor prognosis was associated with *LLGL2* copy-number amplifications in TCGA patients (p value = 0.068) and mRNA overexpression in METABRIC patients (p value = 0.011). Four luminal interactor genes (*DDX23, ZNF385A, WIBG, RPS26*) located at 12q13, when amplified, showed poor survival in both TCGA and METABRIC patients (p values < 0.001, with the exception of WIBG, which has no data in METABRIC) (Figures 4E, 5D, 6D, and S15–S17, Tables S10, S11, and S12).

Crucially, the functions of some interactor genes have been individually linked to tumor survival and invasion. *BOP1* was implicated in dysregulated ribosome biogenesis that promotes metastatic breast cancer cells to the

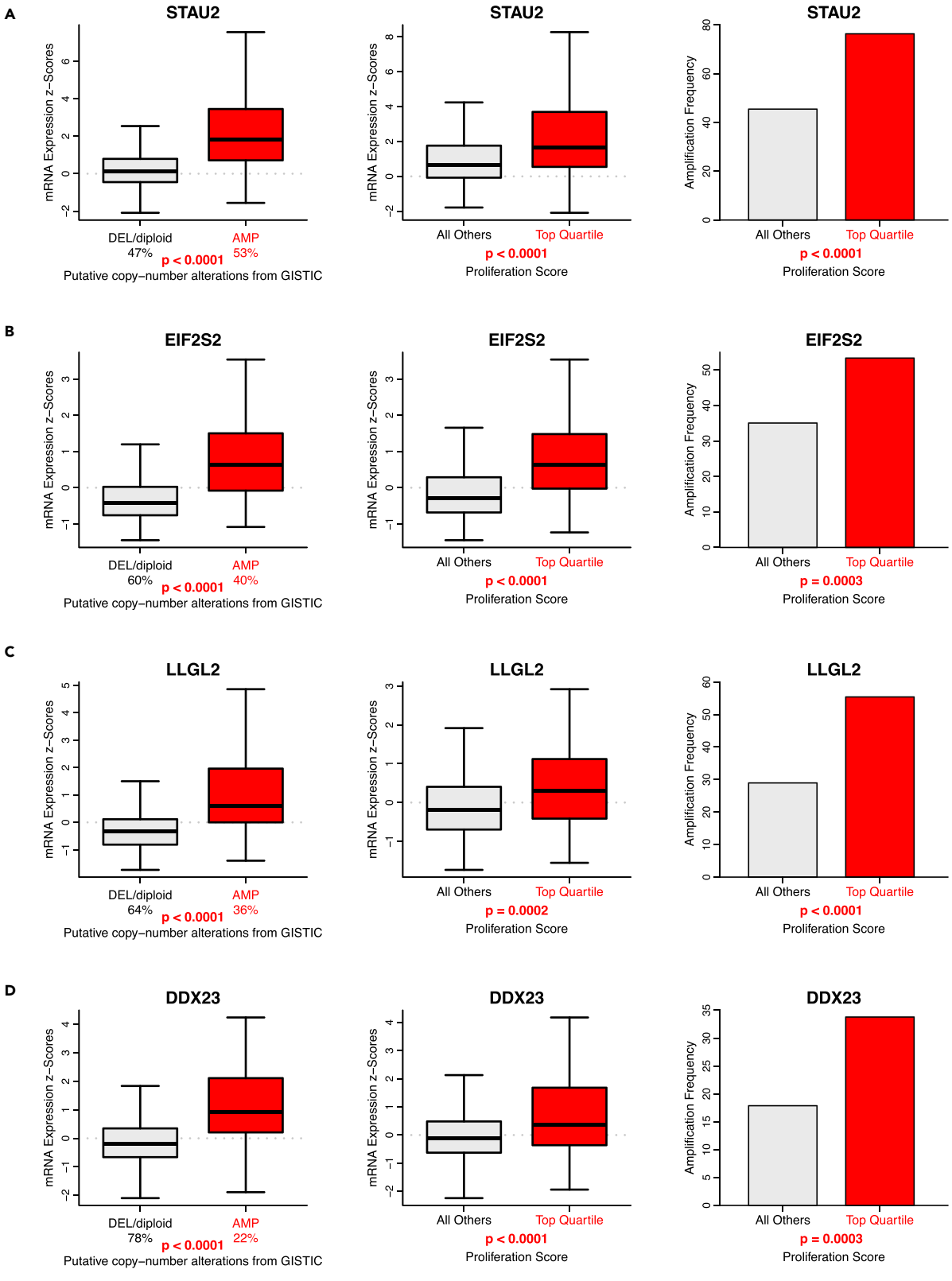
A
STAU2
mRNA Expression z–Scores
DEL/diploid
47%
AMP
53%
p < 0.0001
Putative copy–number alterations from GISTIC
STAU2
mRNA Expression z–Scores
All Others
Top Quartile
p < 0.0001
Proliferation Score
STAU2
Amplification Frequency
All Others
Top Quartile
p < 0.0001
Proliferation Score
B
EIF2S2
mRNA Expression z–Scores
DEL/diploid
60%
AMP
40%
p < 0.0001
Putative copy–number alterations from GISTIC
EIF2S2
mRNA Expression z–Scores
All Others
Top Quartile
p < 0.0001
Proliferation Score
EIF2S2
Amplification Frequency
All Others
Top Quartile
p = 0.0003
Proliferation Score
C
LLGL2
mRNA Expression z–Scores
DEL/diploid
64%
AMP
36%
p < 0.0001
Putative copy–number alterations from GISTIC
LLGL2
mRNA Expression z–Scores
All Others
Top Quartile
p = 0.0002
Proliferation Score
LLGL2
Amplification Frequency
All Others
Top Quartile
p < 0.0001
Proliferation Score
D
DDX23
mRNA Expression z–Scores
DEL/diploid
78%
AMP
22%
p < 0.0001
Putative copy–number alterations from GISTIC
DDX23
mRNA Expression z–Scores
All Others
Top Quartile
p < 0.0001
Proliferation Score
DDX23
Amplification Frequency
All Others
Top Quartile
p = 0.0003
Proliferation Score

Figure 5. Multi-omics Identification of Proliferative Luminal Drivers

Example correlation plots for luminal G9a interactor genes in the following rows: (A) *STAU2*, (B) *EIF2S2*, (C) *LLGL2*, (D) *DDX23*. (Left) Box plots showing the distribution of mRNA expression for luminal samples with a GISTIC values of 1 or 2 (AMP) compared with GISTIC values of 0, -1, or -2 (DEL/diploid). The percent of luminal TCGA samples in each group is indicated. The adjusted p value as determined by a Mann-Whitney-Wilcoxon Test is displayed to indicate the significance of the AMP group having higher mRNA expression. (Middle) Box plots showing the distribution of mRNA expression for luminal samples with a proliferation score in the top quartile compared with all the other samples. The adjusted p value as determined by a Mann-Whitney-Wilcoxon Test is displayed to indicate the significance of the Top Quartile group having higher mRNA expression. (Right) Bar plots showing the frequency of samples with an amplification (GISTIC values of 1 or 2) for the indicated gene for luminal samples with a proliferation score in the top quartile compared with all other samples. The adjusted p value as determined by a Fisher's Exact Test for Count Data is displayed to indicate the significance of the Top Quartile group having a significantly greater amplification frequency.

See also Figures S6, S9, S12, and S15; Tables S7, S8, and S9.

brain (Lee et al., 2008), and genetic aberration in the *BOP1* chromosomal location 8q24 is associated with a risk of colorectal cancer (Gruber et al., 2007). The ribosomal protein *RPL8,* also a known G9a substrate, has an established correlation to chemotherapeutic response (Swoboda et al., 2007). *C8orf33* was found significantly upregulated in breast cancer drug treatment (Ma et al., 2013). Finally, mRNA overexpression of *EHMT2* indicated poor prognosis for luminal patients in the METABRIC dataset (Table S12).

Drivers of Invasive Tumors Show Multi-omics Aberrations in Patients with Poor-prognosis BLBC

Distinct from most of luminal G9a interactors, the majority of BLBC/basal interactor genes showed iCEP, which indicated strong correlations between the oncogenic consequences represented by enhanced G9a binding and their mRNA overexpression in basal patients (Figures 3 and S3). Figure 7A summarizes the distribution of basal interactors with correlations in iCEP; and/or mRNA overexpression, CNA, proliferation score; and/or a high CNA frequency (>= 40%). For example, fifty-one basal G9a interactors were found with high percentage of CNAs (Table S10). The chromosomal location of BLBC/basal G9a interactors with frequent CNAs is shown in Figures 7B and 7C.

Among the interactors that showed at least two correlations, we searched for new invasion driver genes with proliferation-correlated multi-omics aberrations in basal patients with poor prognosis. Unlike luminal G9a luminal interactors, only a few basal G9a interactors individually were associated with poor prognosis (Tables S13 and S14). For example, in the overall survival (OS) analysis of the TCGA (Ciriello et al., 2015) (Figure 8A, p 0.128) and METABRIC (Curtis et al., 2012) (Figure 8B, p 0.288) patient data, overexpression of G9a (*EHMT2*) *alone* was not significantly prognostic. We therefore performed KM survival analysis to identify which *combinations* of multiple basal G9a interactor genes showed co-aberrations in mRNA expression and/or CNAs in basal patients having invasive tumors. We defined the altered group as patients with an mRNA expression *Z* score in the top 50% for all the genes in the combination. For this analysis, we examined basal patient samples from both TCGA (n = 136) and METABRIC (n = 198).

First, co-overexpression of G9a and its interactor genes *PRPF6, XRN2,* and *YBX3* (Figures 8C and 8D) or *DDX50, ILF2,* and *SURF6* (Figures 8E and 8F) was observed in both TCGA and METABRIC basal patient subsets with poor survival. *XRN2* (20p11.22) and *PRPF6* (20q13.33), located on different arms of chromosome 20, showed an mRNA expression versus copy-number correlation (Table S7) with a high CNA frequency (Table S10). Overexpression of *PRPF6* has a role in colorectal cancer tumor growth by promoting alternative splicing of genes involved in cell proliferation (Adler et al., 2014). Copy-number amplifications of *PRPF6* correlated with this overexpression of *PRPF6* in colon tumors. *DDX50, ILF2,* and *SURF6* are basal iCEP genes (Figure S3 and Table S6) showing a correlation between mRNA overexpression and CNA (Table S7).

Also, BLBC/basal patients with the worst prognosis possessed co-overexpression of multiple interactor genes with highly frequent CNA that correlated with mRNA overexpression, including *HNRNPF, ILF3,* and *MRPL39* (Figures S18A and S18B); *EHMT1, EHMT2,* and *ILF3* (Figures S18C and S18D); and *DDX56, FBL,* and *HNRNPF* (Figures S18E and S18F). *HNRNPF* and *MRPL39* also showed an mRNA overexpression versus proliferation correlation. Each of these genes in a prognostically significant combination is located on different chromosomes. *HNRNPF* has a role in cell proliferation (Goh et al., 2010) and is a potential biomarker for colorectal cancer progression (Balasubramani et al., 2006). The transcription factor ILF3 promotes sustained urokinase-type plasminogen activator expression in metastatic breast cancer cells (Hu et al., 2013). Furthermore, we identified ten panels of multiple G9a interactor genes that showed at least two correlations (Figure 7A) and co-overexpression of interactor genes in each panel was found in basal patient subsets with poor prognosis (Figure S19).

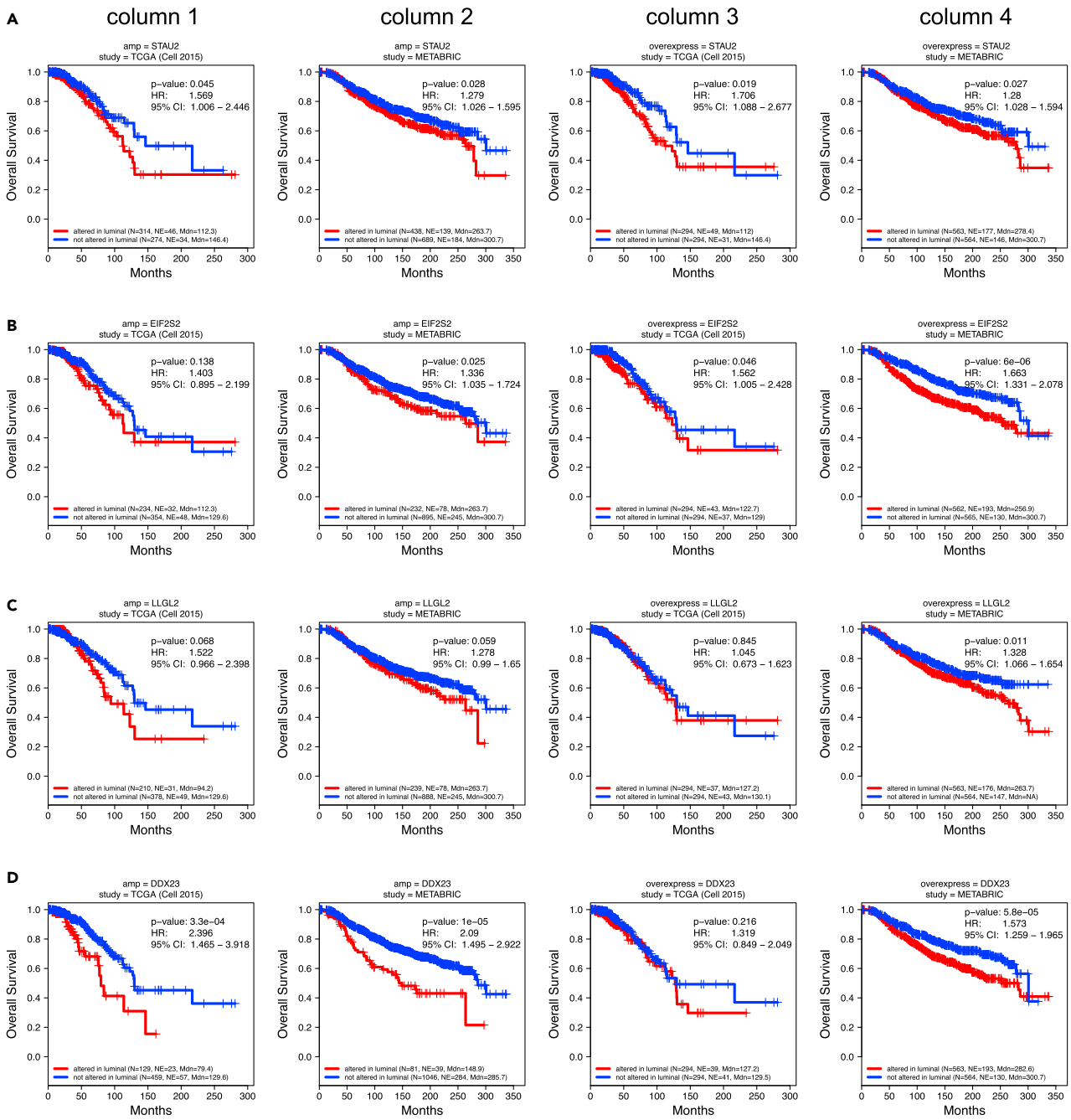

Figure 6. Survival Analysis of Proliferative Luminal Drivers

Example Kaplan-Meier survival analysis plots for luminal G9a interactor genes in the following rows: (A) *STAU2*, (B) *EIF2S2*, (C) *LLGL2*, (D) *DDX23*. Columns 1 and 2 show Kaplan-Meier survival analysis plots for luminal samples with copy-number amplification (GISTIC score of 1 or 2) (red line)versus copy-number deletion or diploid (GISTIC score of 0, -1, or -2) (blue line) in luminal TCGA samples (column 1) and luminal METABRIC samples (column 2). Columns 3 and 4 show Kaplan-Meier survival analysis plots for luminal samples with mRNA overexpression (*Z* score > median *Z* score) (red line) compared with samples not showing mRNA overexpression (*Z* score < median *Z* score) (blue line) in luminal TCGA samples (column 3) and luminal METABRIC samples (column 4). For the Kaplan-Meier plots, "N" refers to "Number of samples" and "NE" refers to "Number of Events." The number of events is for OS status = "DECEASED." "Mdn" indicates the median months survival. The log rank p value and Hazard Ratio (HR) with 95% Confidence Interval (CI) between the two groups are indicated in each plot.

See also Figures S7, S8, S10, S11, S13, S14, S16, and S17; Tables S11 and S12.

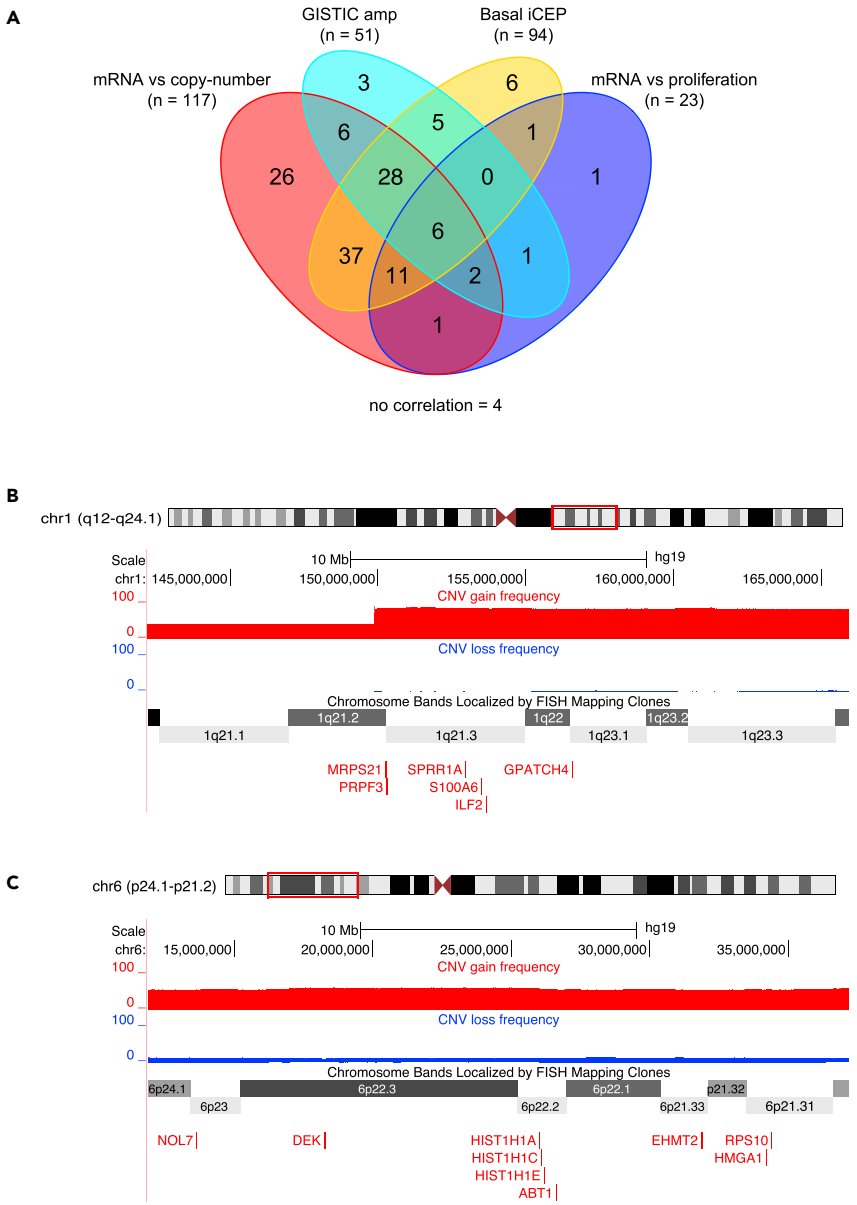

Figure 7. Multi-omics Correlated Identification of Drivers of Invasive Basal Tumor

(A) Venn diagram showing overlap of basal G9a interactors with mRNA versus copy number, mRNA versus proliferation, and basal iCEP correlations, and an amplification (GISTIC values of 1 or 2) frequency greater or equal to 40%.

(B) UCSC Genome Browser view showing location of basal G9a interactors (*MRPS21, PRPF3, SPRR1A, S100A6, ILF2, GPATCH4*) located in the 1q21-23 region of chromosome 1.

(C) UCSC Genome Browser view showing location of basal G9a interactors (*NOL7, DEK, HIST1H1A, HIST1H1C, HIST1H1E, ABT1, EHMT2, HMGA1, RPS10*) located in an amplified region on the p arm of chromosome 6. For each view, the frequency of basal TCGA samples with copy-number gain (segmentation mean >0.1) (red) and copy-number loss (segmentation mean < −0.1) (blue) is indicated.

See also Figures S20 and S21; Tables S7, S8, S9, and S10.

Many basal interactor genes with iCEP are located in chromosomal regions that show high CNA frequencies in TCGA patients with BLBC (Figures 7B and 7C). Of special interest, certain pairs of G9a interactors are directly adjacent to one another in the genome (Figure S20). Particularly interesting is the clustering of iCEP interactors located at genomic loci 1q21 (*MRPS21, PRPF3, S100A6, ILF2, SPRR1A*) and 1q23

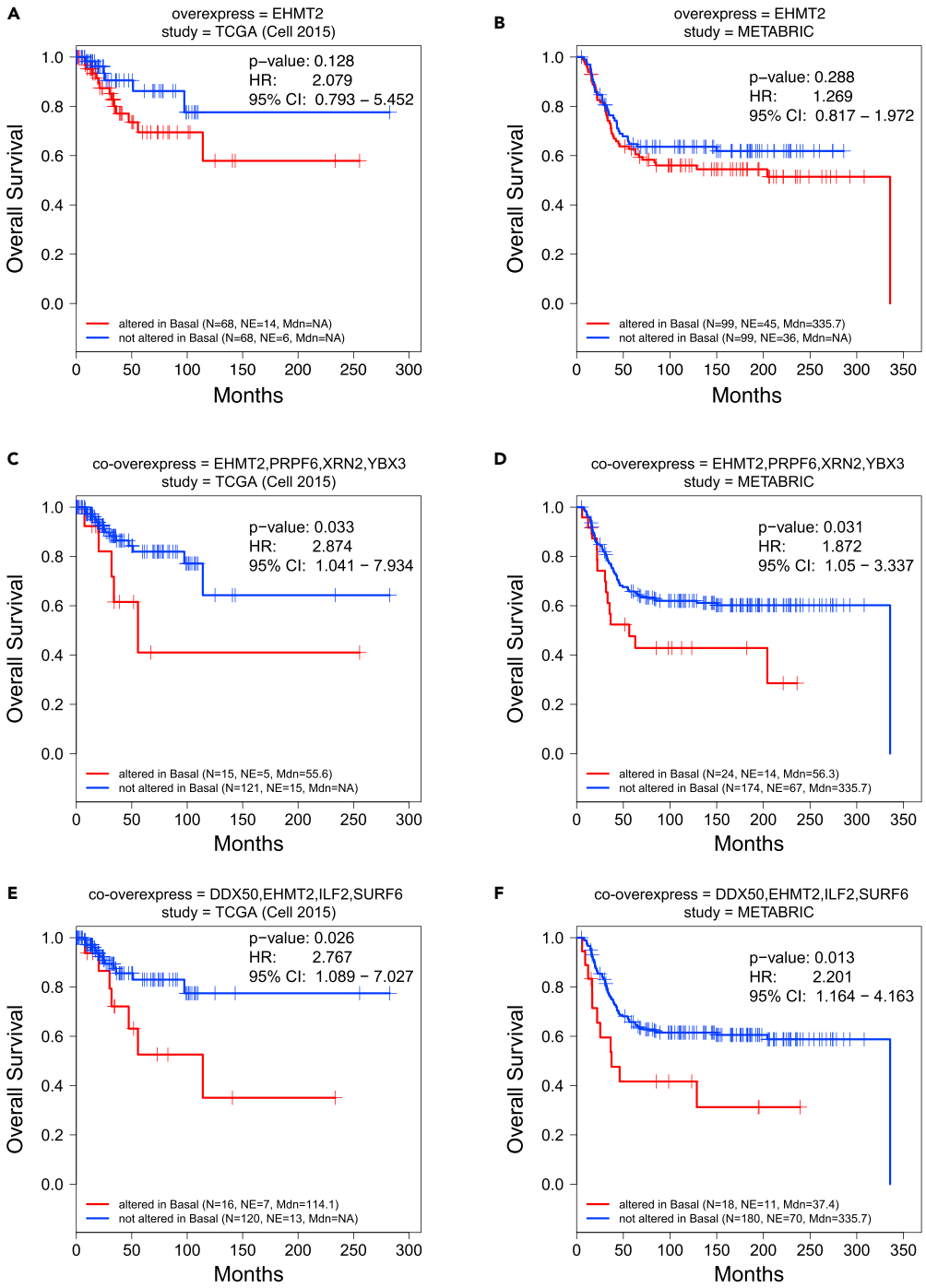

Figure 8. Identification of Driver Genes Showing Co-overexpression/Co-amplification in Patients with Poor Prognosis

Kaplan-Meier survival analysis indicates that altered mRNA expression of G9a interactor genes is prognostically significant in marking distinct patient subpopulations within single PAM50 subtypes.

(A, C, and E) Overall survival (OS) plots of TCGA patients with the BLBC subtype (n = 136).

(B, D, and F) Overall survival (OS) plots of METABRIC patients with the BLBC subtype (n = 198).

For (A and B) the altered group (red line) is samples with mRNA overexpression (*Z* score > median *Z* score) for EHMT2. The non-altered group (blue line) is samples not showing mRNA overexpression (*Z* score < median *Z* score) for EHMT2. For the other panels, the altered group (red line) is samples with mRNA co-overexpression (*Z* score > median *Z* score for all genes

Figure 8. *Continued*
in the combination) for EHMT2, PRPF6, XRN2, and YBX3 (C and D) and DDX50, EHMT2, ILF2, and SURF6 (E and F). The non-altered group (blue line) is the remaining samples not showing mRNA co-overexpression for the same genes. "N" refers to "Number of samples" and "NE" refers to "Number of Events." The number of events is for OS status = "DECEASED." "Mdn" indicates the median months survival. The log rank p value and Hazard Ratio (HR) with 95% Confidence Interval (CI) between the two groups are indicated in each plot.
See also Figures S18 and S19; Tables S13 and S14.

(*GPATCH4*) where *MRPS21* and *PRPF3* (1q21.2) are immediate neighbors with 89% CNA frequency (Figures 7B and S20A). These interactors have a consistently high CNA level in the TCGA patients compared with most other interactors (Figure S21). The 1q21-23 region is amplified uniquely in human BLBC, and it contains breast cancer driver genes (Silva et al., 2015). Also, in amplified regions of chromosome 6, a pair of interactor genes, *HMGA1* and *RPS10* (6p21.31), showed about a 50% CNA frequency and are separated by only two genes (Figure S20E).

Similar to luminal tumor proliferation drivers, the functions of some interactor panel genes have been individually characterized as drivers of proliferative or invasive tumor. The secreted protein CYR61 promotes BLBC/TNBC metastasis (Huang et al., 2017; Sanchez-Bailon et al., 2015). LYAR, a ribosome-associated protein, is a key regulator of the migration and invasion of human CRC cells (Wu et al., 2015) and a regulator of translation associated with cell proliferation (Yonezawa et al., 2014). *Recently, using CRISPR/Cas9-mediated knockdown of LYAR in the invasive BLBC MDA-MB-231 cells, we characterized LYAR as a driver of invasive breast tumor* (Wang et al., 2018). DEK promotes tumor growth, cellular motility, and invasion in breast cancer (Privette Vinnedge et al., 2011). NIFK has a role in lung cancer progression, and increased NIFK expression was associated with poor prognosis in patients with lung cancer (Lin et al., 2016). DDX21 is involved in breast cancer proliferation by promoting AP-1 activity and rRNA processing (Zhang et al., 2014). DDX3X promotes breast cell proliferation by inhibiting the expression of KLF4, a cell cycle repressor (Cannizzaro et al., 2018). Overexpression of rRNA methyl-transferase FBL causes altered rRNA methylation patterns leading to decreased translation fidelity and translation of cancer-related genes from internal ribosome initiation sites (Marcel et al., 2013). Uniquely, ChaC identified these proteins as G9a interactors in the networked pathways that drive invasive BLBC (Figure 2A). *HMGA1* drives metastatic progression in TNBC cells (Shah et al., 2013).

DISCUSSION

Genome-wide studies of patients with breast cancer have generated enormous amounts of genomic and transcriptomic data. Still, sizable additional efforts, such as xenotransplantation amplification of tumor fractions and predictive score modeling (Ng et al., 2016) are required to determine which genomic/transcriptomic aberrations are of oncogenic significance. Also, invasive tumors often evolve heterogeneously, producing subclones different from the earlier specimen from which a treatment decision was made. Either because of low phenotypic accuracy of genomics and transcriptomics or low MS proteomic phenotypic coverage of individual patient's alterations, single-omics approaches usually fail to dissect this intra-tumor heterogeneity. Thus, for optimized therapeutic decisions, we require new multi-omics methods that enable real-time diagnostic identification of drivers or druggable targets in evolving tumor tissue.

We demonstrate that ChaC is a simple, robust method enabling *in situ,* efficient dissection of intra-tumor heterogeneity to *identify the genetic and transcriptomic alterations that manifest as oncogenically active proteins*. Because it specifically binds with antibody-like affinity (IC_{50} < 2.5 nM) to the enzymatically (oncogenically) active form of G9a, the G9a ChaC probe UNC0965 can capture and enrich endogenous, oncogenically active G9a/GLP-interacting epiproteomes for subsequent, focused MS/MS characterization. This front-end epiproteomic enrichment avoids interfering signals from non-tumor-related proteins in other cell types, especially neighboring non-malignant cells in which G9a/GLP is less enzymatically active. Accordingly, our cross-referencing LFQ data confirmed that the G9a/GLP affinities of UNC0965-captured proteins were quantitatively correlated or conserved in similar tumor phenotypes across different sample types, from homogeneous cell lines to heterogeneous tumor tissues (Figure 1D). This quantitative consistency confirms that UNC0965 can directly sort the G9a/GLP-interacting proteins that represent the predominant tumor phenotype in the tissue microenvironment.

ChaC is a generic technique for the rapid *in situ* characterization of endogenous, tumor-phenotypic epigenetic regulatory protein complexes. The small molecule chemoprobe substitution for an antibody

facilitates the integration of a simple, on-bead sample processing with LFQ LC-MS/MS characterization. Unlike antibodies, a ChaC probe does not disrupt protein complexes, and ChaC probes eliminate concerns about antibody cross-reactivity. Also, the tight association between biotin and NeutrAvidin minimizes sample loss and enables extensive washing to remove MS-incompatible contaminants, e.g., detergents, salts, and nonspecific proteins, so retained proteins can be immediately subjected to reduction, alkylation, and on-bead tryptic digestion. Because tryptic digests of large antibodies (>150 kDa) may suppress the peptide signals from low-abundance proteins, the smaller NeutrAvidin (60 kDa) is particularly suitable for on-bead digestion. Concurrently, the specificity and sensitivity of MS is fully utilized for focused analysis of the low-abundance, tumor-phenotypic G9a epiproteomes that are thereby "teased out" from thousands of other proteins in a cancer proteome, making ChaC applicable to clinical isolates of a few million "sorted" cells. Thus, ChaC eliminates tedious, clinically incompatible steps and yields rapid and precise identification of oncogenically active proteins in clinical isolates without diluting information about tumor invasiveness.

ChaC-identified G9a/GLP interactors over-represented the regulatory pathways/networks associated with tumor cell viability such as RNA processing, translation, ribosomal biogenesis, and protein synthesis, the major hallmarks of tumor growth, survival, and invasion. These findings are consistent with the fact that G9a/GLP small molecule inhibitors suppressed BC cell growth and survival *in vitro* (Casciello et al., 2017) and inhibited epithelial-mesenchymal transition-mediated invasion of aggressive BLBC cells (Liu et al., 2018). Thus, ChaC can measure *in vivo* oncogenic pathway activity by identifying *in situ* particular chromatin proteins with tumor-phenotypic G9a/GLP interactions, as opposed to extrapolations of pathway activity based on gene-expression analyses (Gatza et al., 2014).

Because of low MS sensitivity, only small portions of a proteome can be sequenced. Thus, quantitative profiling of global protein expression differences in TCGA samples has produced MS/MS-sequenced peptides that match less than 5% of the BC-related, genomic/transcriptomic variants (Mertins et al., 2016; Ruggles et al., 2016). This low coverage considerably limits information about individualized tumor-phenotypic alterations. Our iC-MAP method has overcome this problem by linking tumor-phenotypic data (epiproteomes) to tumor-genotypic data with comprehensive coverage of individualized alterations. In this regard, without cost- and labor-intensive sampling and genome-wide fishing exploration, akin to "finding a needle in a haystack," ChaC pinpoints particular tumor-phenotypic driver genes with prognostically significant multi-omics alterations; these driver genes would otherwise be indistinguishable from non-tumor-related genes in transcriptomic or genetic profiles. Specifically, the retrospective population-based analyses of TCGA and METABRIC patient data revealed iC-MAP wherein select ChaC-identified G9a interactors had proliferation scores that aligned with highly frequent copy-number amplifications and/or mRNA overexpression. This connection indicates that these interactor genes are fully translated into the oncogenically active proteins in patients with proliferative or invasive tumor. Furthermore, iC-MAP enables a multi-omics dissection of the intra-tumor or interpatient heterogeneity within single PAM50 subtypes that is far more complicated than might be predicted from genetic or transcriptomic aberrations alone. iC-MAP also identified the mRNA-overexpression or CNA profiles of interactor genes that are prognostically meaningful in distinguishing the subsets of luminal or BLBC patients with distinct clinical outcomes in multiple patient databases.

Notably, the goal of the current study was not to build a "perfect" prediction model for personal prognosis but rather to identify candidate genes that serve as interacting partners to G9a that function as drivers of proliferation or invasion and which may represent therapeutically actionable targets. Thus, the prognostic capacity of these genes, while noted, serves as a filtering step and these analyses have not been subjected to multiple comparison correction. Multivariate analysis has been previously reported for EIF2S2 and EIF6 (Gatza et al., 2014) in combination with standard clinical parameters including proliferation. Given that the identified genes correlate with proliferation (Figure 4), which is probably one of the strongest known prognostic feature for breast cancers, we would not expect that these genes, or combination of genes, would appreciably add to the overall prognostic model when proliferation was included within the multivariate analysis model; this observation was true for both EIF2S2 and EIF6 in the previously cited study. However, as we have noted, many of the identified genes are co-amplified or co-expressed. As illustrated in Figure S19, accounting for co-overexpression does in fact improve the prognostic capacity of some sets of genes.

Ultimately, not all identified genes will be able to function as prognosis predictive biomarkers at both the mRNA and/or DNA copy-number level. As would be expected, differences in prognostic capacity

between mRNA and DNA copy-number status for a given gene may reflect different mechanisms by which each gene is activated/regulated in addition to DNA copy-number status. We will note, however, that the DNA copy-number status and mRNA levels of the vast majority of the identified genes were prognostic in the METABRIC study, whereas less robust results were observed in the TCGA cohort. These differences likely reflect differences in the completeness of the clinical data in each dataset—the TCGA clinical follow-up time is ~2 years (24.3 months), whereas the METABRIC dataset has a more clinically relevant 7.2-year follow-up.

In the clinic, quantitative PCR assays on our identified interactor genes could stratify patient treatment regimes, i.e., how will individual patients respond, will they develop resistance, and what are the most appropriate, optimized drug or dose? Thus, clinicians will use these prognostically meaningful biomarkers to select, within the early window of opportunity for cure, personalized therapeutic strategies with the highest likelihood of success for each luminal or BLBC subpopulation, to assess therapeutic effectiveness and the risk of disease recurrence during treatment.

In sum, conceptually innovative, our iC-MAP results also revealed that the tumor heterogeneity resulting from complex interactions between genetic susceptibility and environmental perturbation is not driven by genomic aberrations alone but, instead, by dynamic, coordinated, multi-omics alterations. Guided by our ChaC breakthrough technology that enables *in situ* identification of driver proteins of subclonal heterogeneity in real time, iC-MAP further characterizes drivers of evolving proliferative or invasive subclones by continual acquisition of new genetic aberrations or punctuated clonal expansion. Because patients with proliferative luminal and invasive basal tumors are the clinical subsets for which most available therapeutic options are ineffective, our iC-MAP findings represent new diagnostic/prognostic markers to identify patient subsets with metastatic disease. Our findings also form the basis for precision therapeutic strategies that are matched to the proliferative or invasive potential of individual tumors.

Limitations of the Study

To obtain statistically significant correlations for driver determination, iC-MAP requires both mRNA expression and copy-number aberration data from large patient cohorts. In addition, ChaC analysis is limited to freshly collected or frozen tissues and peripheral blood cells.

METHODS

All methods can be found in the accompanying Transparent Methods supplemental file.

SUPPLEMENTAL INFORMATION

Supplemental Information can be found online at https://doi.org/10.1016/j.isci.2019.07.001.

ACKNOWLEDGMENTS

This work was supported in part by grants NC Tracs TTSA Phase I TTSA021P1, NIH 1U19AI109965, 1U24CA160035-01 from the National Cancer Institute Clinical Proteomic Tumor Analysis Consortium (CPTAC) (to X.C.) and R01GM122749 (to J.J.). We thank Dr. Howard Fried for editorial assistance. This invention of iC-MAP is protected by United States Provisional Patent Application Serial No. 62/608,992 that was filed by the University of North Carolina-Chapel Hill.

AUTHOR CONTRIBUTIONS

J.A.W. developed the software, performed proteogenomic analysis of clinical data, and wrote the report. L.X. and L.W. performed sample preparation and processing of some cell lines and clinical tissues for MS/MS experimental analysis, analyzed data, and conducted functional characterization. C.L. performed chem-precipitation with UNC0965 for PCR. N.R., M.L.G., and K.K.G. assisted clinicopathological data analysis. Y.X., K.D.K., and J.J. provided UNC0965 and UNC125. X.C. conceived and designed the project and experiments, analyzed and interpreted data, and wrote the manuscript.

DECLARATION OF INTERESTS

The invention of ChaC is protected by US Patent Application Serial No. 15/118,061 that was filed by the University of North Carolina-Chapel Hill.

Received: January 22, 2019
Revised: May 16, 2019
Accepted: July 1, 2019
Published: July 26, 2019

REFERENCES

Adler, A.S., McCleland, M.L., Yee, S., Yaylaoglu, M., Hussain, S., Cosino, E., Quinones, G., Modrusan, Z., Seshagiri, S., Torres, E., et al. (2014). An integrative analysis of colon cancer identifies an essential function for PRPF6 in tumor growth. Genes Dev. *28*, 1068–1084.

Ahringer, J. (2000). NuRD and SIN3 histone deacetylase complexes in development. Trends Genet. *16*, 351–356.

Baker, M. (2011). Making sense of chromatin states. Nat. Methods *8*, 717–722.

Balasubramani, M., Day, B.W., Schoen, R.E., and Getzenberg, R.H. (2006). Altered expression and localization of creatine kinase B, heterogeneous nuclear ribonucleoprotein F, and high mobility group box 1 protein in the nuclear matrix associated with colon cancer. Cancer Res. *66*, 763–769.

Cannizzaro, E., Bannister, A.J., Han, N., Alendar, A., and Kouzarides, T. (2018). DDX3X RNA helicase affects breast cancer cell cycle progression by regulating expression of KLF4. FEBS Lett. *592*, 2308–2322.

Casciello, F., Al-Ejeh, F., Kelly, G., Brennan, D.J., Ngiow, S.F., Young, A., Stoll, T., Windloch, K., Hill, M.M., Smyth, M.J., et al. (2017). G9a drives hypoxia-mediated gene repression for breast cancer cell survival and tumorigenesis. Proc. Natl. Acad. Sci. U S A *114*, 7077–7082.

Cerami, E., Gao, J., Dogrusoz, U., Gross, B.E., Sumer, S.O., Aksoy, B.A., Jacobsen, A., Byrne, C.J., Heuer, M.L., Larsson, E., et al. (2012). The cBio cancer genomics portal: an open platform for exploring multidimensional cancer genomics data. Cancer Discov. *2*, 401–404.

Ciriello, G., Gatza, M.L., Beck, A.H., Wilkerson, M.D., Rhie, S.K., Pastore, A., Zhang, H., McLellan, M., Yau, C., Kandoth, C., et al. (2015). Comprehensive molecular portraits of invasive lobular breast cancer. Cell *163*, 506–519.

Curtis, C., Shah, S.P., Chin, S.F., Turashvili, G., Rueda, O.M., Dunning, M.J., Speed, D., Lynch, A.G., Samarajiwa, S., Yuan, Y., et al. (2012). The genomic and transcriptomic architecture of 2,000 breast tumours reveals novel subgroups. Nature *486*, 346–352.

Dong, C., Wu, Y., Yao, J., Wang, Y., Yu, Y., Rychahou, P.G., Evers, B.M., and Zhou, B.P. (2012). G9a interacts with Snail and is critical for Snail-mediated E-cadherin repression in human breast cancer. J. Clin. Invest. *122*, 1469–1486.

Easwaran, H., Tsai, H.C., and Baylin, S.B. (2014). Cancer epigenetics: tumor heterogeneity, plasticity of stem-like states, and drug resistance. Mol. Cell *54*, 716–727.

Gao, J., Aksoy, B.A., Dogrusoz, U., Dresdner, G., Gross, B., Sumer, S.O., Sun, Y., Jacobsen, A., Sinha, R., Larsson, E., et al. (2013). Integrative analysis of complex cancer genomics and clinical profiles using the cBioPortal. Sci. Signal. *6*, pl1.

Garnett, M.J., Edelman, E.J., Heidorn, S.J., Greenman, C.D., Dastur, A., Lau, K.W., Greninger, P., Thompson, I.R., Luo, X., Soares, J., et al. (2012). Systematic identification of genomic markers of drug sensitivity in cancer cells. Nature *483*, 570–575.

Gatza, M.L., Silva, G.O., Parker, J.S., Fan, C., and Perou, C.M. (2014). An integrated genomics approach identifies drivers of proliferation in luminal-subtype human breast cancer. Nat. Genet. *46*, 1051–1059.

Goh, E.T., Pardo, O.E., Michael, N., Niewiarowski, A., Totty, N., Volkova, D., Tsaneva, I.R., Seckl, M.J., and Gout, I. (2010). Involvement of heterogeneous ribonucleoprotein F in the regulation of cell proliferation via the mammalian target of rapamycin/S6 kinase 2 pathway. J. Biol. Chem. *285*, 17065–17076.

Green, E.D., and Guyer, M.S. (2011). Charting a course for genomic medicine from base pairs to bedside. Nature *470*, 204–213.

Gruber, S.B., Moreno, V., Rozek, L.S., Rennerts, H.S., Lejbkowicz, F., Bonner, J.D., Greenson, J.K., Giordano, T.J., Fearson, E.R., and Rennert, G. (2007). Genetic variation in 8q24 associated with risk of colorectal cancer. Cancer Biol. Ther. *6*, 1143–1147.

Helin, K., and Dhanak, D. (2013). Chromatin proteins and modifications as drug targets. Nature *502*, 480–488.

Hu, Q., Lu, Y.Y., Noh, H., Hong, S., Dong, Z., Ding, H.F., Su, S.B., and Huang, S. (2013). Interleukin enhancer-binding factor 3 promotes breast tumor progression by regulating sustained urokinase-type plasminogen activator expression. Oncogene *32*, 3933–3943.

Huang, Y.T., Lan, Q., Lorusso, G., Duffey, N., and Ruegg, C. (2017). The matricellular protein CYR61 promotes breast cancer lung metastasis by facilitating tumor cell extravasation and suppressing anoikis. Oncotarget *8*, 9200–9215.

Huttlin, E.L., Ting, L., Bruckner, R.J., Gebreab, F., Gygi, M.P., Szpyt, J., Tam, S., Zarraga, G., Colby, G., Baltier, K., et al. (2015). The BioPlex network: a systematic exploration of the human interactome. Cell *162*, 425–440.

Johnson, D.G., and Dent, S.Y. (2013). Chromatin: receiver and quarterback for cellular signals. Cell *152*, 685–689.

Konze, K.D., Pattenden, S.G., Liu, F., Barsyte-Lovejoy, D., Li, F., Simon, J.M., Davis, I.J., Vedadi, M., and Jin, J. (2014). A chemical tool for in vitro and in vivo precipitation of lysine methyltransferase G9a. ChemMedChem *9*, 549–553.

Koren, S., and Bentires-Alj, M. (2015). Breast tumor heterogeneity: source of fitness, hurdle for therapy. Mol. Cell *60*, 537–546.

Lee, J.H., Horak, C.E., Khanna, C., Meng, Z., Yu, L.R., Veenstra, T.D., and Steeg, P.S. (2008). Alterations in Gemin5 expression contribute to alternative mRNA splicing patterns and tumor cell motility. Cancer Res. *68*, 639–644.

Lin, T.C., Su, C.Y., Wu, P.Y., Lai, T.C., Pan, W.A., Jan, Y.H., Chang, Y.C., Yeh, C.T., Chen, C.L., Ger, L.P., et al. (2016). The nucleolar protein NIFK promotes cancer progression via CK1alpha/beta-catenin in metastasis and Ki-67-dependent cell proliferation. Elife *5*, e11288.

Liu, C., Yu, Y., Liu, F., Wei, X., Wrobel, J.A., Gunawardena, H.P., Zhou, L., Jin, J., and Chen, X. (2014a). A chromatin activity-based chemoproteomic approach reveals a transcriptional repressome for gene-specific silencing. Nat. Commun. *5*, 5733.

Liu, N.Q., Stingl, C., Look, M.P., Smid, M., Braakman, R.B., De Marchi, T., Sieuwerts, A.M., Span, P.N., Sweep, F.C., Linderholm, B.K., et al. (2014b). Comparative proteome analysis revealing an 11-protein signature for aggressive triple-negative breast cancer. J. Natl. Cancer Inst. *106*, djt376.

Liu, X.R., Zhou, L.H., Hu, J.X., Liu, L.M., Wan, H.P., and Zhang, X.Q. (2018). UNC0638, a G9a inhibitor, suppresses epithelial mesenchymal transition mediated cellular migration and invasion in triple negative breast cancer. Mol. Med. Rep. *17*, 2239–2244.

Ma, C., Chen, H.I., Flores, M., Huang, Y., and Chen, Y. (2013). BRCA-Monet: a breast cancer specific drug treatment mode-of-action network for treatment effective prediction using large scale microarray database. BMC Syst. Biol. *7* (*Suppl 5*), S5.

Maier, V.K., Feeney, C.M., Taylor, J.E., Creech, A.L., Qiao, J.W., Szanto, A., Das, P.P., Chevrier, N., Cifuentes-Rojas, C., Orkin, S.H., et al. (2015). Functional proteomic analysis of repressive histone methyltransferase complexes reveals ZNF518B as a G9A regulator. Mol. Cell. Proteomics *14*, 1435–1446.

Malovannaya, A., Lanz, R.B., Jung, S.Y., Bulynko, Y., Le, N.T., Chan, D.W., Ding, C., Shi, Y., Yucer, N., Krenciute, G., et al. (2011). Analysis of the human endogenous coregulator complexome. Cell *145*, 787–799.

Marcel, V., Ghayad, S.E., Belin, S., Therizols, G., Morel, A.P., Solano-Gonzalez, E., Vendrell, J.A., Hacot, S., Mertani, H.C., Albaret, M.A., et al. (2013). p53 acts as a safeguard of translational control by regulating fibrillarin and rRNA methylation in cancer. Cancer Cell *24*, 318–330.

Mertins, P., Mani, D.R., Ruggles, K.V., Gillette, M.A., Clauser, K.R., Wang, P., Wang, X., Qiao,

J.W., Cao, S., Petralia, F., et al. (2016). Proteogenomics connects somatic mutations to signalling in breast cancer. Nature *534*, 55–62.

Ng, S.W., Mitchell, A., Kennedy, J.A., Chen, W.C., McLeod, J., Ibrahimova, N., Arruda, A., Popescu, A., Gupta, V., Schimmer, A.D., et al. (2016). A 17-gene stemness score for rapid determination of risk in acute leukaemia. Nature *540*, 433–437.

Ooi, L., and Wood, I.C. (2007). Chromatin crosstalk in development and disease: lessons from REST. Nat. Rev. Genet. *8*, 544–554.

Oshiro, M.M., Kim, C.J., Wozniak, R.J., Junk, D.J., Munoz-Rodriguez, J.L., Burr, J.A., Fitzgerald, M., Pawar, S.C., Cress, A.E., Domann, F.E., et al. (2005). Epigenetic silencing of DSC3 is a common event in human breast cancer. Breast Cancer Res. *7*, R669–R680.

Parker, J.S., Mullins, M., Cheang, M.C., Leung, S., Voduc, D., Vickery, T., Davies, S., Fauron, C., He, X., Hu, Z., et al. (2009). Supervised risk predictor of breast cancer based on intrinsic subtypes. J. Clin. Oncol. *27*, 1160–1167.

Pereira, B., Chin, S.F., Rueda, O.M., Vollan, H.K., Provenzano, E., Bardwell, H.A., Pugh, M., Jones, L., Russell, R., Sammut, S.J., et al. (2016). The somatic mutation profiles of 2,433 breast cancers refines their genomic and transcriptomic landscapes. Nat. Commun. *7*, 11479.

Privette Vinnedge, L.M., McClaine, R., Wagh, P.K., Wikenheiser-Brokamp, K.A., Waltz, S.E., and Wells, S.I. (2011). The human DEK oncogene stimulates beta-catenin signaling, invasion and mammosphere formation in breast cancer. Oncogene *30*, 2741–2752.

Ruggles, K.V., Tang, Z., Wang, X., Grover, H., Askenazi, M., Teubl, J., Cao, S., McLellan, M.D., Clauser, K.R., Tabb, D.L., et al. (2016). An analysis of the sensitivity of proteogenomic mapping of somatic mutations and novel splicing events in cancer. Mol. Cell Proteomics *15*, 1060–1071.

Sanchez-Bailon, M.P., Calcabrini, A., Mayoral-Varo, V., Molinari, A., Wagner, K.U., Losada, J.P., Ciordia, S., Albar, J.P., and Martin-Perez, J. (2015). Cyr61 as mediator of Src signaling in triple negative breast cancer cells. Oncotarget *6*, 13520–13538.

Shah, S.N., Cope, L., Poh, W., Belton, A., Roy, S., Talbot, C.C., Jr., Sukumar, S., Huso, D.L., and Resar, L.M. (2013). HMGA1: a master regulator of tumor progression in triple-negative breast cancer cells. PLoS One *8*, e63419.

Shi, Y., Sawada, J., Sui, G., Affar el, B., Whetstine, J.R., Lan, F., Ogawa, H., Luke, M.P., Nakatani, Y., and Shi, Y. (2003). Coordinated histone modifications mediated by a CtBP co-repressor complex. Nature *422*, 735–738.

Si, W., Huang, W., Zheng, Y., Yang, Y., Liu, X., Shan, L., Zhou, X., Wang, Y., Su, D., Gao, J., et al. (2015). Dysfunction of the reciprocal feedback loop between GATA3- and ZEB2-nucleated repression programs contributes to breast cancer metastasis. Cancer Cell *27*, 822–836.

Silva, G.O., He, X., Parker, J.S., Gatza, M.L., Carey, L.A., Hou, J.P., Moulder, S.L., Marcom, P.K., Ma, J., Rosen, J.M., et al. (2015). Cross-species DNA copy number analyses identifies multiple 1q21-q23 subtype-specific driver genes for breast cancer. Breast Cancer Res. Treat. *152*, 347–356.

Swoboda, R.K., Somasundaram, R., Caputo, L., Ochoa, E.M., Gimotty, P.A., Marincola, F.M., Van Belle, P., Barth, S., Elder, D., Guerry, D., et al. (2007). Shared MHC class II-dependent melanoma ribosomal protein L8 identified by phage display. Cancer Res. *67*, 3555–3559.

Torga, G., and Pienta, K.J. (2017). Patient-paired sample congruence between 2 commercial liquid biopsy tests. JAMA Oncol. *4*, 868–870.

Tu, W.B., Shiah, Y.J., Lourenco, C., Mullen, P.J., Dingar, D., Redel, C., Tamachi, A., Ba-Alawi, W., Aman, A., Al-Awar, R., et al. (2018). MYC interacts with the G9a histone methyltransferase to drive transcriptional repression and tumorigenesis. Cancer Cell *34*, 579–595.e8.

Tyanova, S., Temu, T., Sinitcyn, P., Carlson, A., Hein, M.Y., Geiger, T., Mann, M., and Cox, J. (2016). The Perseus computational platform for comprehensive analysis of (prote)omics data. Nat. Methods *13*, 731–740.

Vedadi, M., Barsyte-Lovejoy, D., Liu, F., Rival-Gervier, S., Allali-Hassani, A., Labrie, V., Wigle, T.J., Dimaggio, P.A., Wasney, G.A., Siarheyeva, A., et al. (2011). A chemical probe selectively inhibits G9a and GLP methyltransferase activity in cells. Nat. Chem. Biol. *7*, 566–574.

Wang, L., Wrobel, J.A., Xie, L., Li, D., Zurlo, G., Shen, H., Yang, P., Wang, Z., Peng, Y., Gunawardena, H.P., et al. (2018). Novel RNA-affinity proteogenomics dissects tumor heterogeneity for revealing personalized markers in precision prognosis of cancer. Cell Chem. Biol. *25*, 619–633.e5.

Wee, S., Dhanak, D., Li, H., Armstrong, S.A., Copeland, R.A., Sims, R., Baylin, S.B., Liu, X.S., and Schweizer, L. (2014). Targeting epigenetic regulators for cancer therapy. Ann. N. Y. Acad. Sci. *1309*, 30–36.

Wilson, B.G., and Roberts, C.W. (2011). SWI/SNF nucleosome remodellers and cancer. Nat. Rev. Cancer *11*, 481–492.

Wozniak, R.J., Klimecki, W.T., Lau, S.S., Feinstein, Y., and Futscher, B.W. (2007). 5-Aza-2′-deoxycytidine-mediated reductions in G9A histone methyltransferase and histone H3 K9 di-methylation levels are linked to tumor suppressor gene reactivation. Oncogene *26*, 77–90.

Wu, Y., Alvarez, M., Slamon, D.J., Koeffler, P., and Vadgama, J.V. (2010). Caspase 8 and maspin are downregulated in breast cancer cells due to CpG site promoter methylation. BMC Cancer *10*, 32.

Wu, Y., Liu, M., Li, Z., Wu, X.B., Wang, Y., Wang, Y., Nie, M., Huang, F., Ju, J., Ma, C., et al. (2015). LYAR promotes colorectal cancer cell mobility by activating galectin-1 expression. Oncotarget *6*, 32890–32901.

Yates, L.R., Gerstung, M., Knappskog, S., Desmedt, C., Gundem, G., Van Loo, P., Aas, T., Alexandrov, L.B., Larsimont, D., Davies, H., et al. (2015). Subclonal diversification of primary breast cancer revealed by multiregion sequencing. Nat. Med. *21*, 751–759.

Yonezawa, K., Sugihara, Y., Oshima, K., Matsuda, T., and Nadano, D. (2014). Lyar, a cell growth-regulating zinc finger protein, was identified to be associated with cytoplasmic ribosomes in male germ and cancer cells. Mol. Cell. Biochem. *395*, 221–229.

Zhang, Y., Baysac, K.C., Yee, L.F., Saporita, A.J., and Weber, J.D. (2014). Elevated DDX21 regulates c-Jun activity and rRNA processing in human breast cancers. Breast Cancer Res. *16*, 449.

ISCI, Volume *17*

Supplemental Information

Multi-omic Dissection of Oncogenically Active Epiproteomes Identifies Drivers of Proliferative and Invasive Breast Tumors

John A. Wrobel, Ling Xie, Li Wang, Cui Liu, Naim Rashid, Kristalyn K. Gallagher, Yan Xiong, Kyle D. Konze, Jian Jin, Michael L. Gatza, and Xian Chen

Figure S1

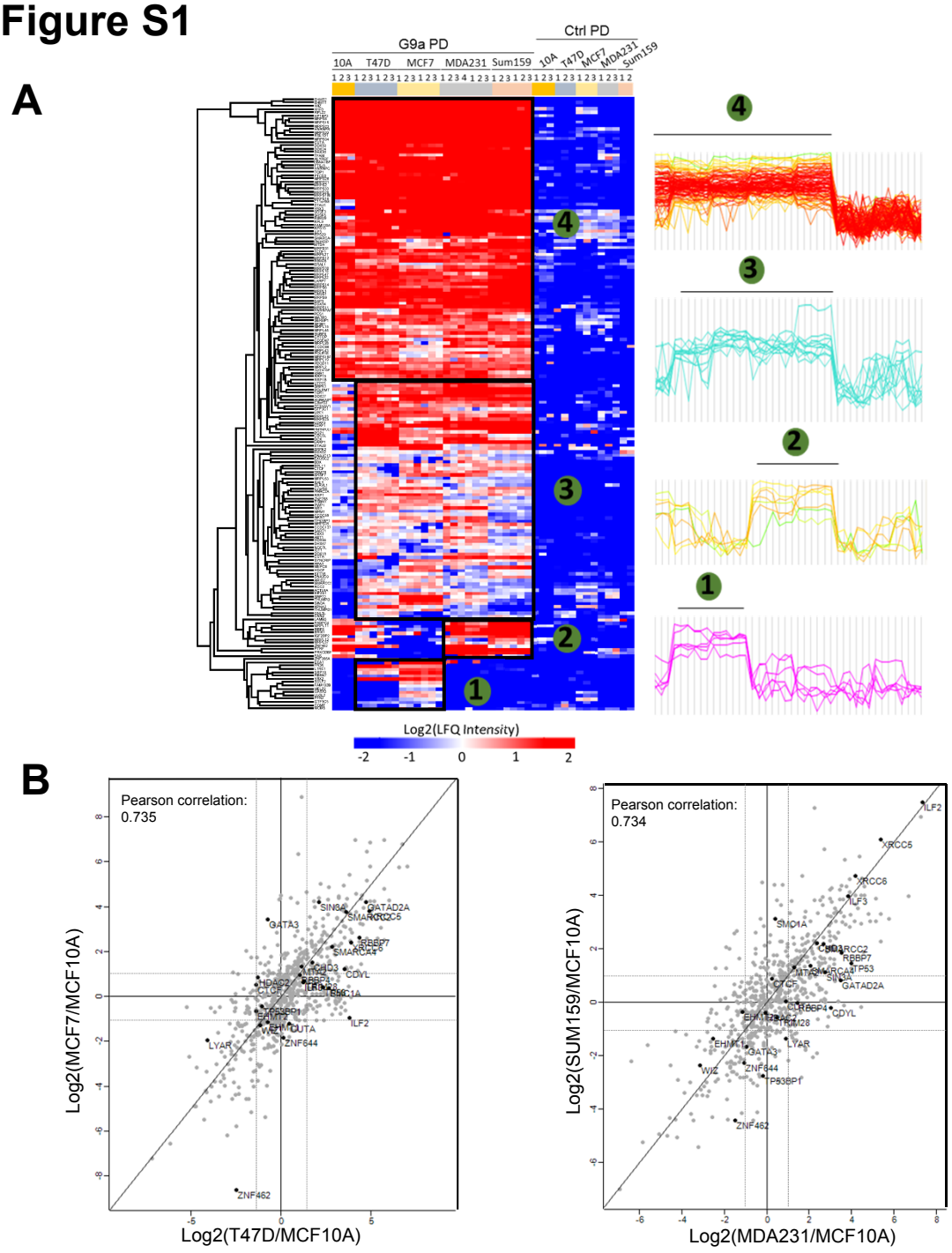

Figure S1. **Quantitative assessment of basal and luminal subtype specific G9a interactors, Related to Figure 1.**

(A) Heat map displays the LFQ ratios of UNC0965-captured proteins in different BC cell lines versus in the normal cell line (MCF10A). 'G9a PD' refers to 'UNC0965 pull-down', and 'Ctrl PD' is the pull-downs from empty beads. Based on the changes of LFQ ratios, the G9a interactors were in four clusters, including luminal- or BLBC/basal- or BC-specific as well as the core components of G9a-interacting epiproteomes. **(B)** LFQ ratios show that the G9a bindings of UNC0965-capurtued proteins are correlated between two luminal-subtype cell lines (MCF7, T47D) versus MCF10A (left), or between two basal subtype cell lines (MDA231, SUM159) versus MCF10A (right). The proteins showing log2 LFQ ratios > 1 or < -1 and -log10 p value > 1 are putative BC subtypic interactors of statistical significance.

Figure S2

A

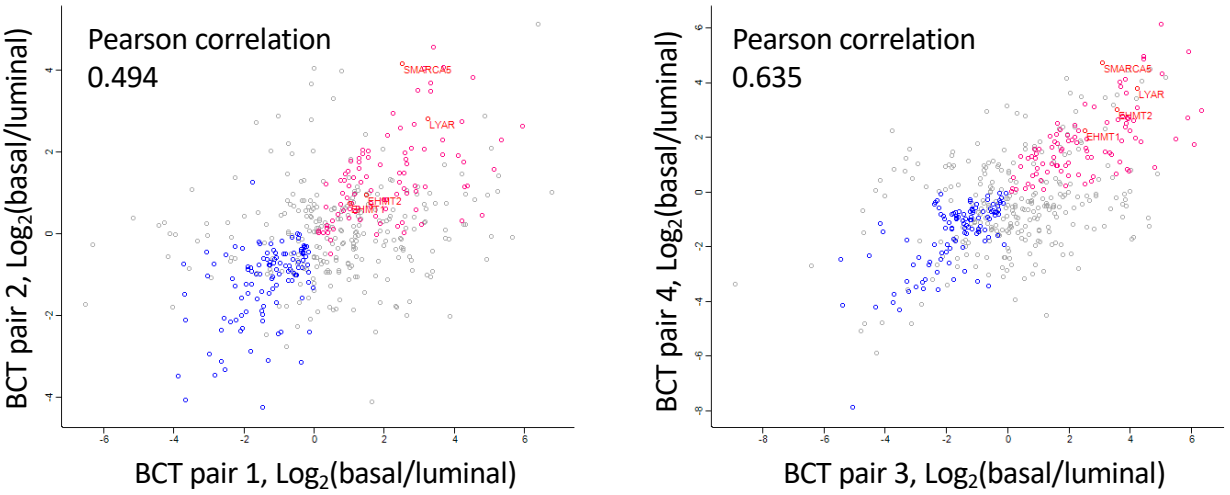
Pearson correlation
0.494
SMARCA5
LYAR
EHMT2
EHMT1
BCT pair 2, Log2(basal/luminal)
BCT pair 1, Log2(basal/luminal)
Pearson correlation
0.635
SMARCA5
LYAR
EHMT2
EHMT1
BCT pair 4, Log2(basal/luminal)
BCT pair 3, Log2(basal/luminal)

B

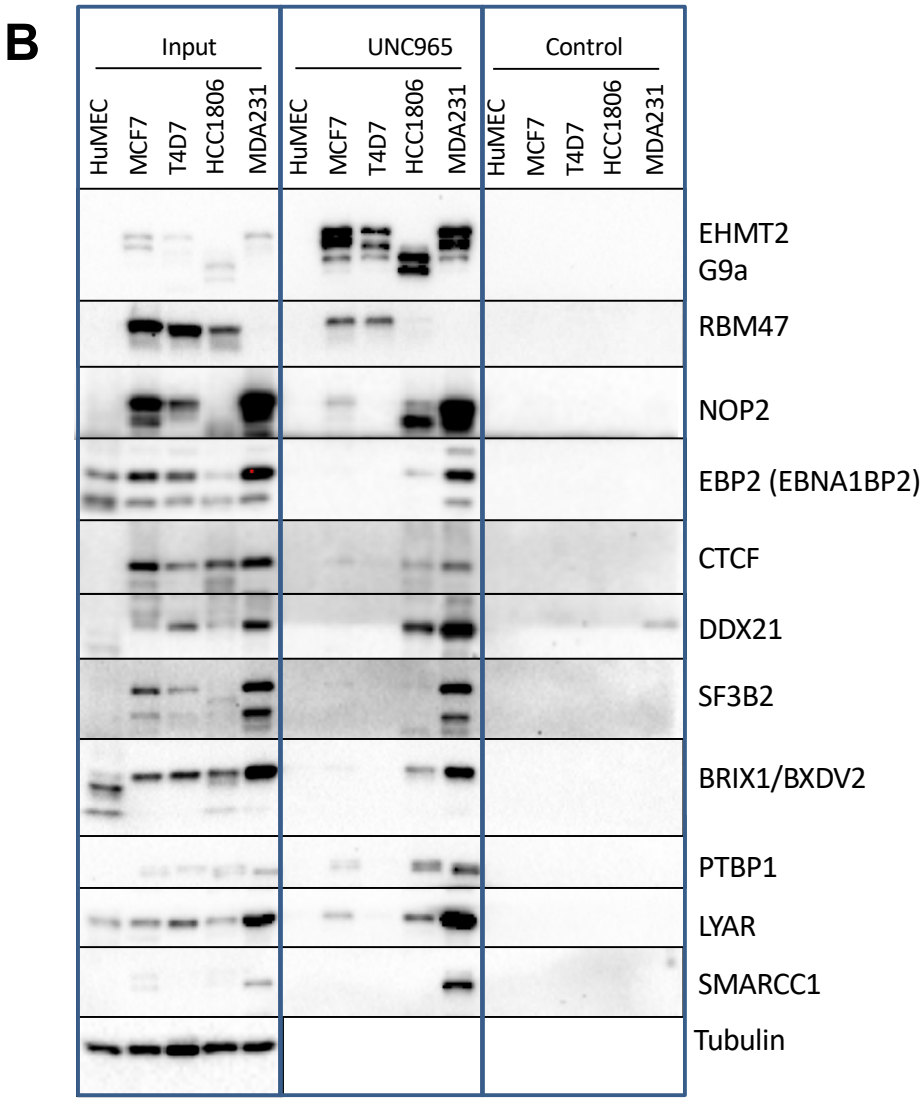
Input
UNC965
Control
HuMEC
MCF7
T4D7
HCC1806
MDA231
EHMT2
G9a
RBM47
NOP2
EBP2 (EBNA1BP2)
CTCF
DDX21
SF3B2
BRIX1/BXDV2
PTBP1
LYAR
SMARCC1
Tubulin

Figure S2. ChaC sorted and characterized the G9a-interacting epiproteome representing single predominate tumor phenotype in heterogenous tissues, Related to Figure 1.

(**A**) Plots of basal/luminal LFQ ratios of UNC0965-captured proteins from human breast cancer tissues (BCT). The proteins showing log2 LFQ ratios > 1 or < -1 and -log10 p value > 1 are putative BC subtypic interactors of statistical significance, including 'purple' for the proteins showing increased binding to G9a in the BLBC patients and 'blue' for the G9a interactors identified in the luminal patients. (**B**) Immunoblotting analysis of the indicated proteins that were captured by UNC0965 or UNC125 (G9a-negative probe) respectively in indicated cell lines. Expect for RBM47 that was identified as a luminal G9a interactor all others are the BLBC-specific G9a interactors.

Figure S3

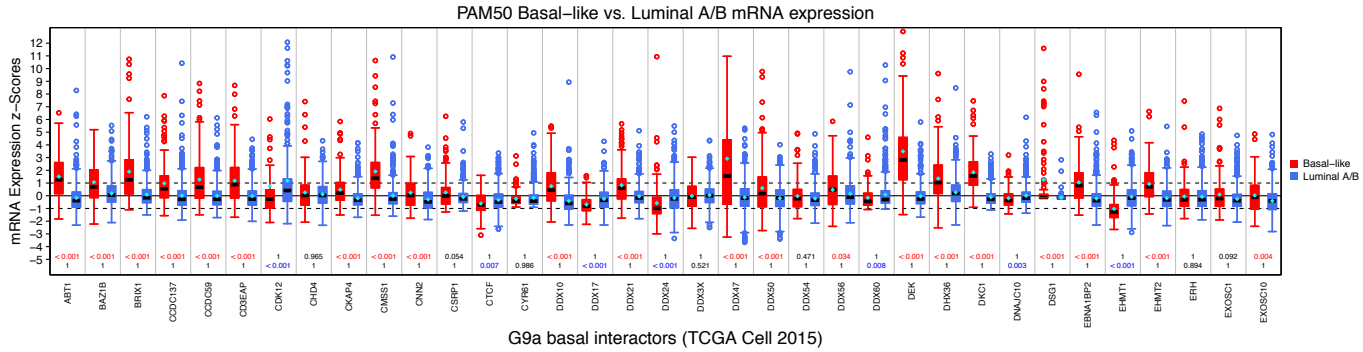
PAM50 Basal–like vs. Luminal A/B mRNA expression
mRNA Expression z–Scores
Basal–like
Luminal A/B
ABT1 BAZ1B BRIX1 CCDC137 CCDC59 CD3EAP CDK12 CHD4 CKAP4 CMSS1 CNN2 CSRP1 CTCF CYR61 DDX10 DDX17 DDX21 DDX24 DDX3X DDX47 DDX50 DDX54 DDX56 DDX60 DEK DHX36 DXC1 DNAJC10 DSG1 EBNA1BP2 EHMT1 EHMT2 ERH EXOSC1 EXOSC10
G9a basal interactors (TCGA Cell 2015)

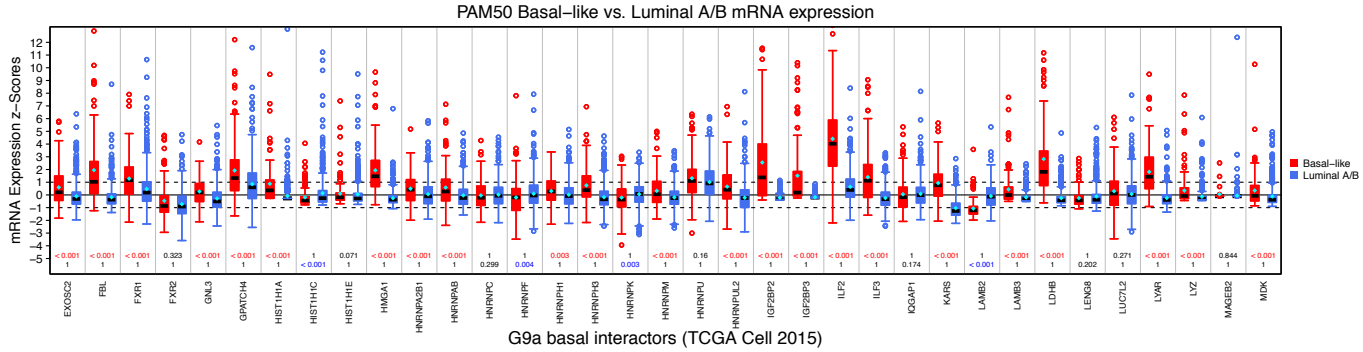
PAM50 Basal–like vs. Luminal A/B mRNA expression
mRNA Expression z–Scores
Basal–like
Luminal A/B
EXOSC2 FBL FXR1 FXR2 GNL3 GPATCH4 HIST1H1A HIST1H1C HIST1H1E HMGA1 HNRNPA2B1 HNRNPAB HNRNPC HNRNPF HNRNPH1 HNRNPH3 HNRNPK HNRNPM HNRNPU HNRNPUL2 IGF2BP2 IGF2BP3 ILF2 ILF3 IQGAP1 KARS LAMB2 LAMB3 LDHB LENG8 LUC7L2 LYAR LYZ MAGEB2 MDK
G9a basal interactors (TCGA Cell 2015)

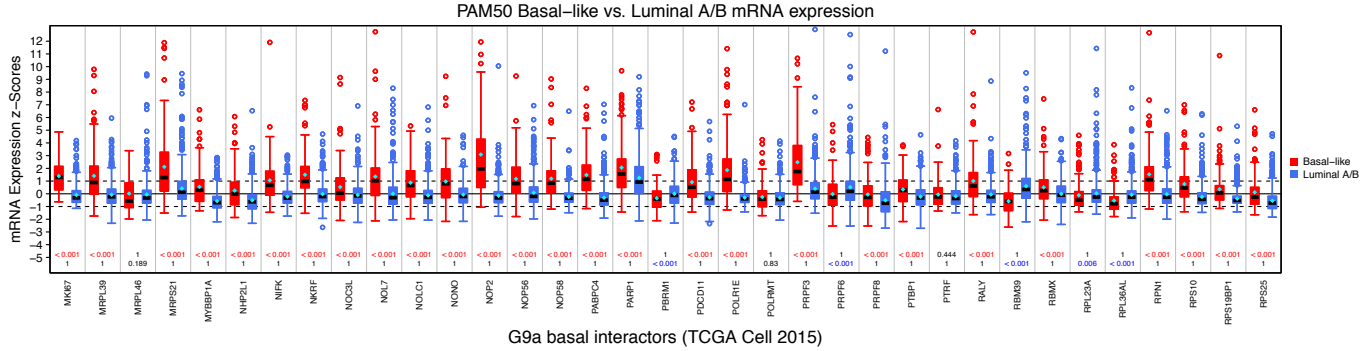
PAM50 Basal–like vs. Luminal A/B mRNA expression
mRNA Expression z–Scores
Basal–like
Luminal A/B
MKI67 MRPL39 MRPL46 MRPS21 MYBBP1A NHP2L1 NIFK NKRF NOC3L NOL7 NOLC1 NONO NOP2 NOP56 NOP58 PABPC4 PARP1 PBRM1 PDCD11 POLR1E POLRMT PRPF3 PRPF6 PRPF8 PTBP1 PTRF RALY RBM39 RBMX RPL23A RPL36AL RPN1 RPS10 RPS19BP1 RPS25
G9a basal interactors (TCGA Cell 2015)

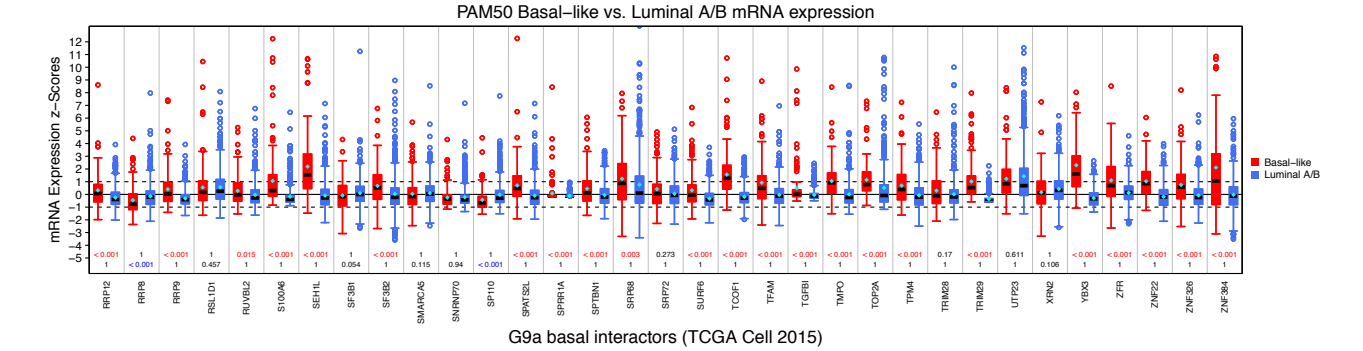
PAM50 Basal–like vs. Luminal A/B mRNA expression
mRNA Expression z–Scores
Basal–like
Luminal A/B
PRPF12 RRP8 RRP9 RSL1D1 RUVBL2 S100A6 SEH1L SF3B1 SF3B2 SMARCA5 SNRNP70 SP110 SPATS2L SPRR1A SPTBN1 SRRM2 SRP72 SUPV3L1 TCOF1 TFAM TGFB1I1 TMPO TOP2A TPM4 TRIM28 TRIM29 UTP23 XRN2 YBX3 ZFR ZNF22 ZNF326 ZNF384
G9a basal interactors (TCGA Cell 2015)

Figure S3. iCEP box plots for complete set of G9a basal interactors, Related to Figure 3.

Box plots showing the statistically significant altered mRNA expression (x-axis) for the complete set of basal G9a interactor genes. For each interactor gene, the distribution of mRNA expression for PAM50 basal-like TCGA patients (N = 136) is shown on the left in red, and for PAM50 luminal TCGA patients (N = 590) is shown on the right colored in blue. Outliers are indicated as circles. The median is indicated by the black bar inside each box. The mean is indicated by the cyan diamond. The mRNA expression as a Z-score is displayed on the y-axis. A Mann-Whitney-Wilcoxon Test was performed on each pair to judge differences in expression levels. This Mann-Whitney Wilcoxon Test was performed on all genes in the TCGA data set (n = ~18,000) and the resulting p-values were adjusted for multiple comparisons. Adjusted p-values are displayed above the x-axis for basal-like samples having greater expression (top line) and luminal samples having greater expression (bottom line). Adjusted p-values < 0.05 are colored red if expression is higher for basal-like and blue if expression is higher for luminal samples.

Figure S4

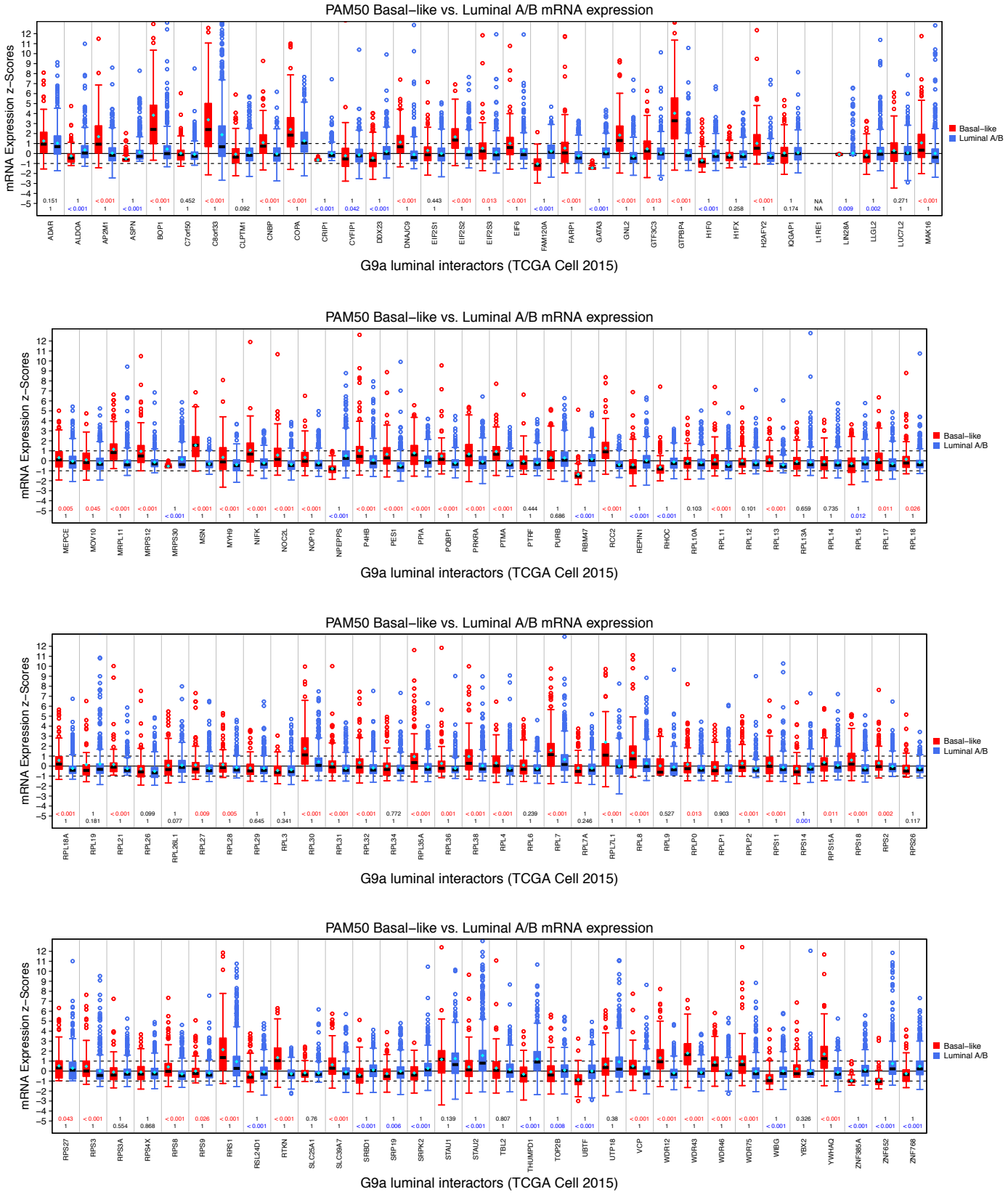
PAM50 Basal–like vs. Luminal A/B mRNA expression
mRNA Expression z–Scores
Basal–like
Luminal A/B
ADAR ALDOA AP2M1 ASPN BOP1 C7orf50 C8orf33 CLPTM1 CNBP COPA CRIP1 CYFIP1 DDX23 DNAJC9 EIF2S1 EIF2S2 EIF2S3 EIF6 FAM120A FARP1 GATA3 GNL2 GTF3C3 GTPBP4 H1F0 H1FX H2AFY2 IQGAP1 L1RE1 LIN28A LLGL2 LUC7L2 MAK-16
G9a luminal interactors (TCGA Cell 2015)
PAM50 Basal–like vs. Luminal A/B mRNA expression
mRNA Expression z–Scores
Basal–like
Luminal A/B
MEPCE MOV10 MRPL11 MRPS12 MRPS30 MSN MYH9 NIFK NOC2L NOP10 NPEPPS P4HB PES1 PPIA PQBP1 PRKRA PTMA PTRF PURB RBM47 RCC2 REPIN1 RHOC RPL10A RPL11 RPL12 RPL13 RPL13A RPL14 RPL15 RPL17 RPL18
G9a luminal interactors (TCGA Cell 2015)
PAM50 Basal–like vs. Luminal A/B mRNA expression
mRNA Expression z–Scores
Basal–like
Luminal A/B
RPL18A RPL19 RPL21 RPL26 RPL26L1 RPL27 RPL28 RPL29 RPL3 RPL30 RPL31 RPL32 RPL34 RPL35A RPL36 RPL38 RPL4 RPL6 RPL7 RPL7A RPL7L1 RPL8 RPL9 RPLP0 RPLP1 RPLP2 RPS11 RPS14 RPS15A RPS18 RPS2 RPS26
G9a luminal interactors (TCGA Cell 2015)
PAM50 Basal–like vs. Luminal A/B mRNA expression
mRNA Expression z–Scores
Basal–like
Luminal A/B
RPS27 RPS3 RPS3A RPS4X RPS8 RPS9 RRS1 RSL24D1 RTKN SLC25A1 SLC39A7 SRBD1 SRP19 SRPK2 STAU1 STAU2 TBL2 THUMPD1 TOP2B UBTF UTP18 VCP WDR12 WDR43 WDR46 WDR75 WIBG YBX2 YWHAQ ZNF385A ZNF652 ZNF768
G9a luminal interactors (TCGA Cell 2015)

Figure S4. iCEP box plots for complete set of G9a luminal interactors, Related to Figure 3.

Box plots showing the statistically significant altered mRNA expression (x-axis) for the complete set of luminal G9a interactor genes. For each interactor gene, the distribution of mRNA expression for PAM50 basal-like TCGA patients (N = 136) is shown on the left in red, and for PAM50 luminal TCGA patients (N = 590) is shown on the right colored in blue. Outliers are indicated as circles. The median is indicated by the black bar inside each box. The mean is indicated by the cyan diamond. The mRNA expression as a Z-score is displayed on the y-axis. A Mann-Whitney-Wilcoxon Test was performed on each pair to judge differences in expression levels. This Mann-Whitney Wilcoxon Test was performed on all genes in the TCGA data set (n = ~18,000) and the resulting p-values were adjusted for multiple comparisons. Adjusted p-values are displayed above the x-axis for basal-like samples having greater expression (top line) and luminal samples having greater expression (bottom line). Adjusted p-values < 0.05 are colored red if expression is higher for basal-like and blue if expression is higher for luminal samples.

Figure S5

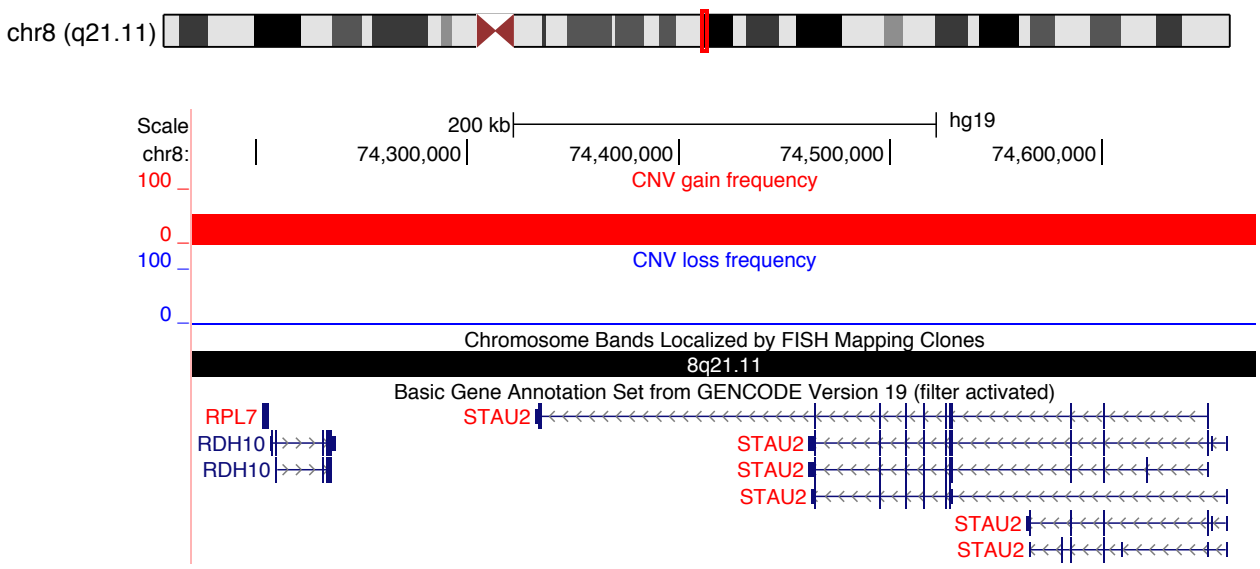
chr8 (q21.11)
Scale
200 kb
hg19
chr8:
74,300,000
74,400,000
74,500,000
74,600,000
100
CNV gain frequency
0
100
CNV loss frequency
0
Chromosome Bands Localized by FISH Mapping Clones
8q21.11
Basic Gene Annotation Set from GENCODE Version 19 (filter activated)
RPL7
RDH10
RDH10
STAU2
STAU2
STAU2
STAU2
STAU2
STAU2

Figure S5. UCSC Genome Browser view of luminal G9a interactors RPL7 and STAU2 whose encoding genes are located near one another, Related to Figure 4.

The names of the G9a interactor genes are displayed in red. The gene annotation track is shown for the “Basic Gene Annotation Set from GENCODE Version 19” filtered to show protein coding transcripts with transcription support level 1 (tsl1). For each view the frequency of luminal TCGA samples with copy number gain (segmentation mean > 0.1) (red) and copy number loss (segmentation mean < -0.1) (blue) is indicated.

Figure S6

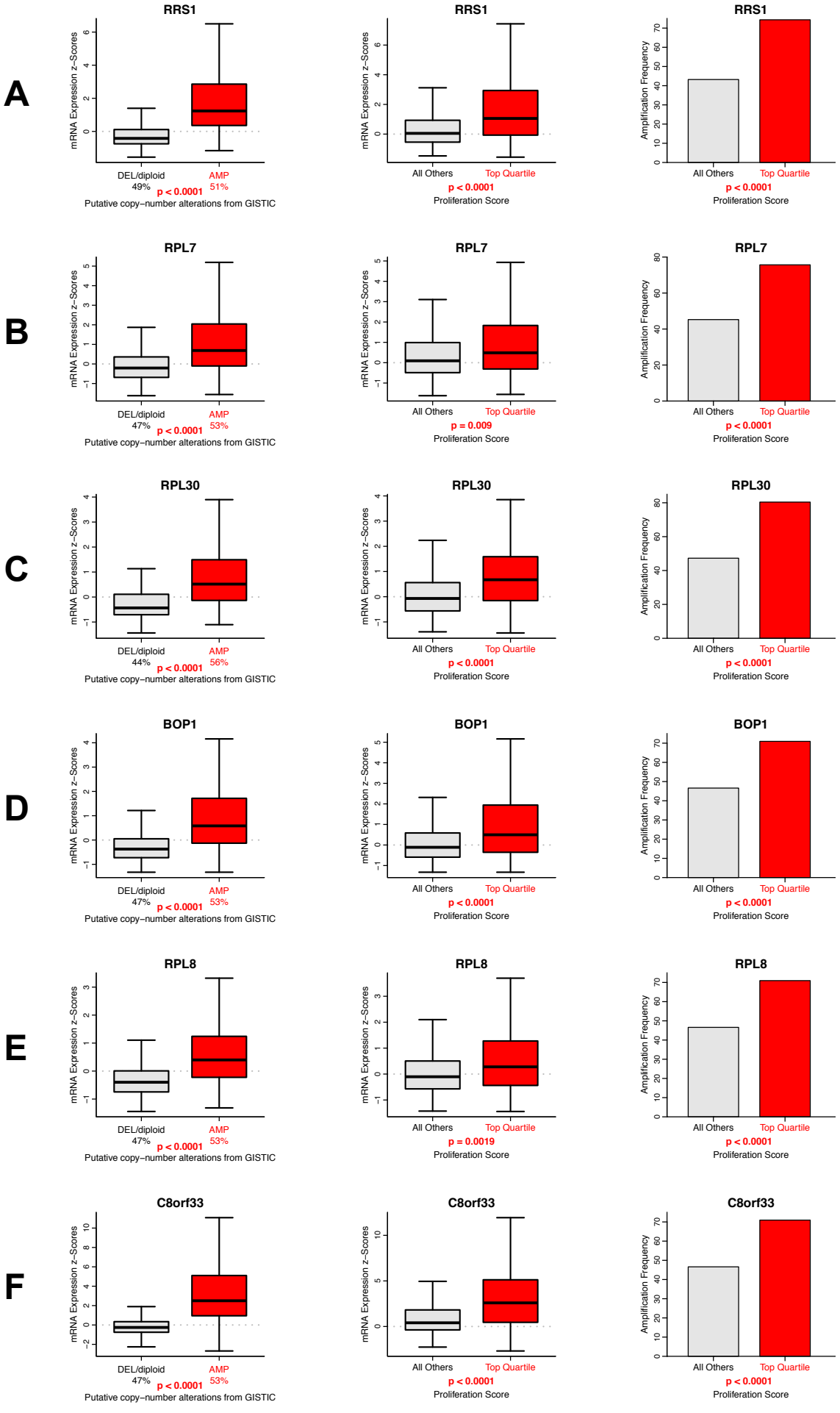
A
RRS1
mRNA Expression z-Scores
DEL/diploid
49%
AMP
51%
p < 0.0001
Putative copy-number alterations from GISTIC
RRS1
mRNA Expression z-Scores
All Others
Top Quartile
p < 0.0001
Proliferation Score
RRS1
Amplification Frequency
All Others
Top Quartile
p < 0.0001
Proliferation Score
B
RPL7
mRNA Expression z-Scores
DEL/diploid
47%
AMP
53%
p < 0.0001
Putative copy-number alterations from GISTIC
RPL7
mRNA Expression z-Scores
All Others
Top Quartile
p = 0.009
Proliferation Score
RPL7
Amplification Frequency
All Others
Top Quartile
p < 0.0001
Proliferation Score
C
RPL30
mRNA Expression z-Scores
DEL/diploid
44%
AMP
56%
p < 0.0001
Putative copy-number alterations from GISTIC
RPL30
mRNA Expression z-Scores
All Others
Top Quartile
p < 0.0001
Proliferation Score
RPL30
Amplification Frequency
All Others
Top Quartile
p < 0.0001
Proliferation Score
D
BOP1
mRNA Expression z-Scores
DEL/diploid
47%
AMP
53%
p < 0.0001
Putative copy-number alterations from GISTIC
BOP1
mRNA Expression z-Scores
All Others
Top Quartile
p < 0.0001
Proliferation Score
BOP1
Amplification Frequency
All Others
Top Quartile
p < 0.0001
Proliferation Score
E
RPL8
mRNA Expression z-Scores
DEL/diploid
47%
AMP
53%
p < 0.0001
Putative copy-number alterations from GISTIC
RPL8
mRNA Expression z-Scores
All Others
Top Quartile
p = 0.0019
Proliferation Score
RPL8
Amplification Frequency
All Others
Top Quartile
p < 0.0001
Proliferation Score
F
C8orf33
mRNA Expression z-Scores
DEL/diploid
47%
AMP
53%
p < 0.0001
Putative copy-number alterations from GISTIC
C8orf33
mRNA Expression z-Scores
All Others
Top Quartile
p < 0.0001
Proliferation Score
C8orf33
Amplification Frequency
All Others
Top Quartile
p < 0.0001
Proliferation Score

Figure S6. Correlation plots for luminal G9a interactor genes located in a region of high amplification frequency on the q arm of chromosome 8 in luminal TCGA samples, Related to Figure 5.

Luminal G9a interactor genes: (**A**) RRS1, (**B**) RPL7, (**C**) RPL30, (**D**) BOP1, (**E**) RPL8, and (**F**) C8orf33 on the q arm of chromosome 8. Each row includes the correlation plots for a specific gene. (left) box plots showing the distribution of mRNA expression for luminal samples with GISTIC values of 1 or 2 (AMP) compared to GISTIC values of 0, -1, or -2 (DEL/diploid). The percent of luminal TCGA samples in each group is indicated. The adjusted p-value as determined by a Mann-Whitney-Wilcoxon Test is displayed to indicate the significance of the AMP group having higher mRNA expression. (middle) box plots showing the distribution of mRNA expression for luminal samples with a proliferation score in the top quartile compared to all the other samples. The adjusted p-value as determined by a Mann-Whitney-Wilcoxon Test is displayed to indicate the significance of the Top Quartile group having higher mRNA expression. (right) bar plots showing the frequency of samples with an amplification (GISTIC values of 1 or 2) for the indicated gene for luminal samples with a proliferation score in the top quartile compared to all the other samples. The adjusted p-value as determined by a Fisher's Exact Test for Count Data is displayed to indicate the significance of the Top Quartile group having a greater amplification frequency. See Figure 5 for the plots for STAU2.

Figure S7

A

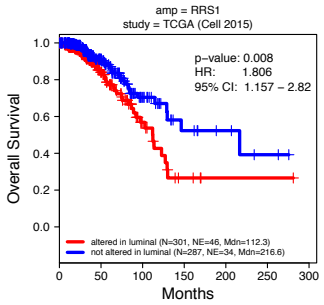

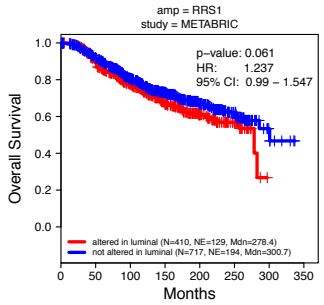

B

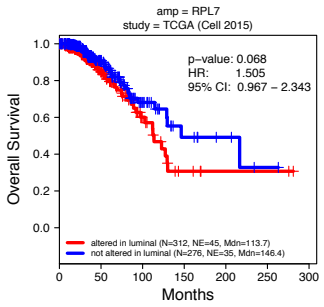

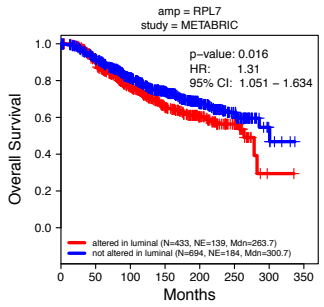

C

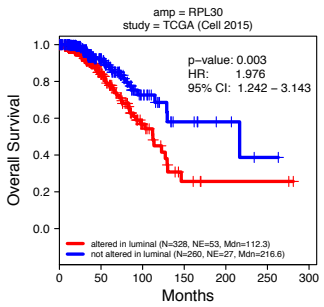

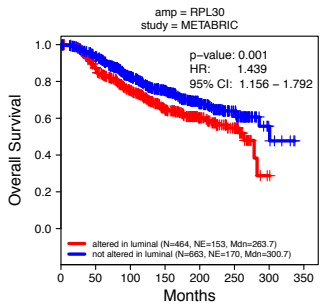

D

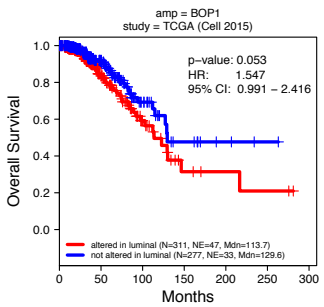

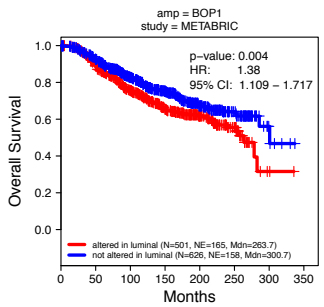

E

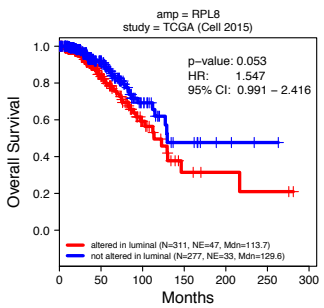

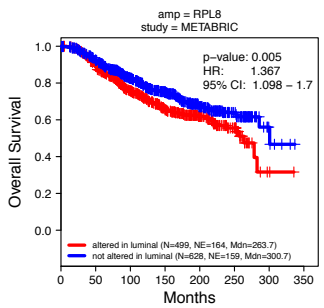

F

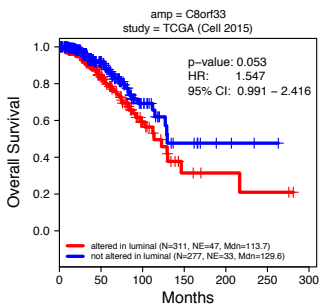

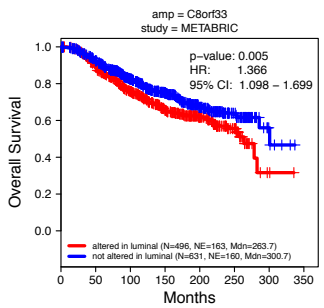

Figure S7. Kaplan-Meier survival analysis plots for luminal samples with copy-number amplification for luminal G9a interactor genes located in a region of high amplification frequency on the q arm of chromosome 8 in luminal TCGA samples, Related to Figure 6.

Luminal G9a interactor genes: (**A**) RRS1, (**B**) RPL7, (**C**) RPL30, (**D**) BOP1, (**E**) RPL8, and (**F**) C8orf33 on the q arm of chromosome 8. Each row includes the Kaplan-Meier survival plots for a specific gene for luminal samples with copy-number amplification (GISTIC score of 1 or 2) (red line) vs. copy-number deletion or diploid (GISTIC score of 0, -1, or -2) (blue line) in luminal TCGA samples (left) and luminal METABRIC samples (right). For the Kaplan-Meier plots, "N" refers to "Number of samples" and "NE" refers to "Number of Events". The number of events is for OS status = "DECEASED". "Mdn" indicates the median months survival. The log-rank p-value and Hazard Ratio (HR) with 95% Confidence Interval (CI) between the two groups are indicated in each plot. See Figure 6 for the plots for STAU2.

Figure S8

A

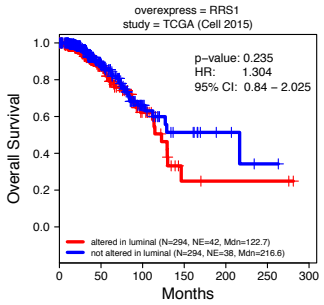

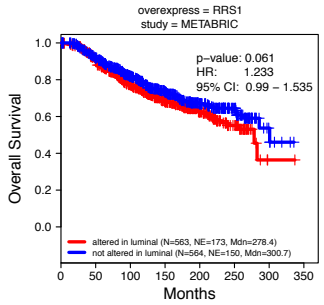

B

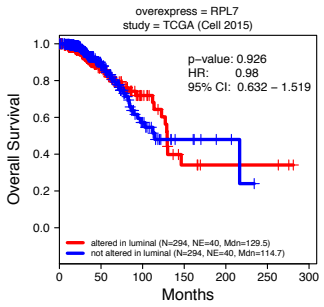

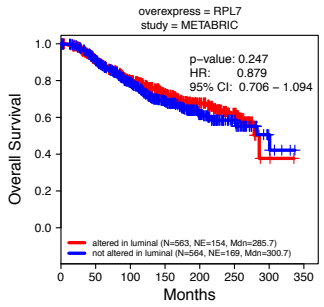

C

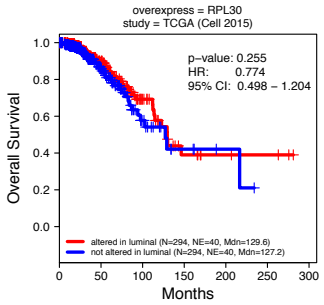

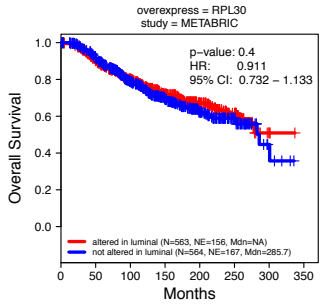

D

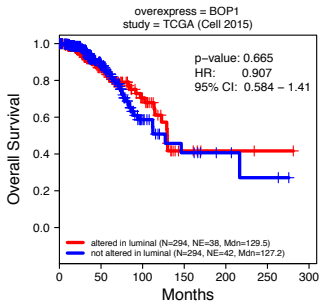

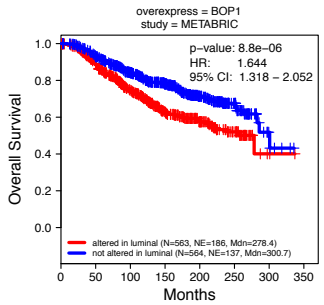

E

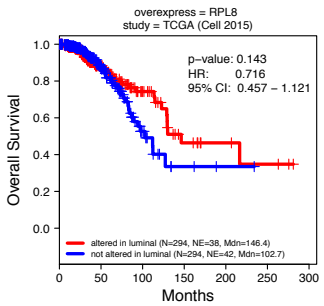

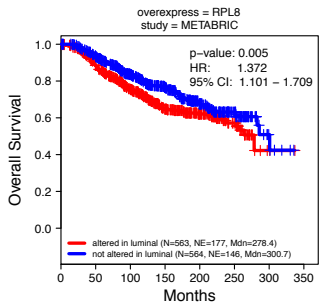

F

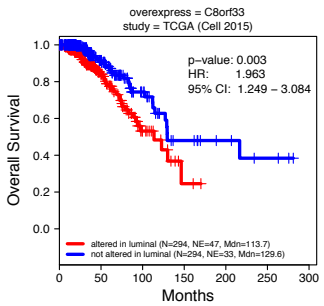

Figure S8. Kaplan-Meier survival analysis plots for luminal samples with mRNA overexpression for luminal G9a interactor genes located in a region of high amplification frequency on the q arm of chromosome 8 in luminal TCGA samples, Related to Figure 6.

Luminal G9a interactor genes: (**A**) RRS1, (**B**) RPL7, (**C**) RPL30, (**D**) BOP1, (**E**) RPL8, and (**F**) C8orf33 (no data in METABRIC) on the q arm of chromosome 8. Each row includes the Kaplan-Meier survival plots for a specific gene for luminal samples with mRNA overexpression (z-score > median z-score) (red line) compared to samples not showing mRNA overexpression (z-score < median z-score) (blue line) in luminal TCGA samples (left) and luminal METABRIC samples (right). For the Kaplan-Meier plots, "N" refers to "Number of samples" and "NE" refers to "Number of Events". The number of events is for OS status = "DECEASED". "Mdn" indicates the median months survival. The log-rank p-value and Hazard Ratio (HR) with 95% Confidence Interval (CI) between the two groups are indicated in each plot. See Figure 6 for the plots for STAU2.

Figure S9

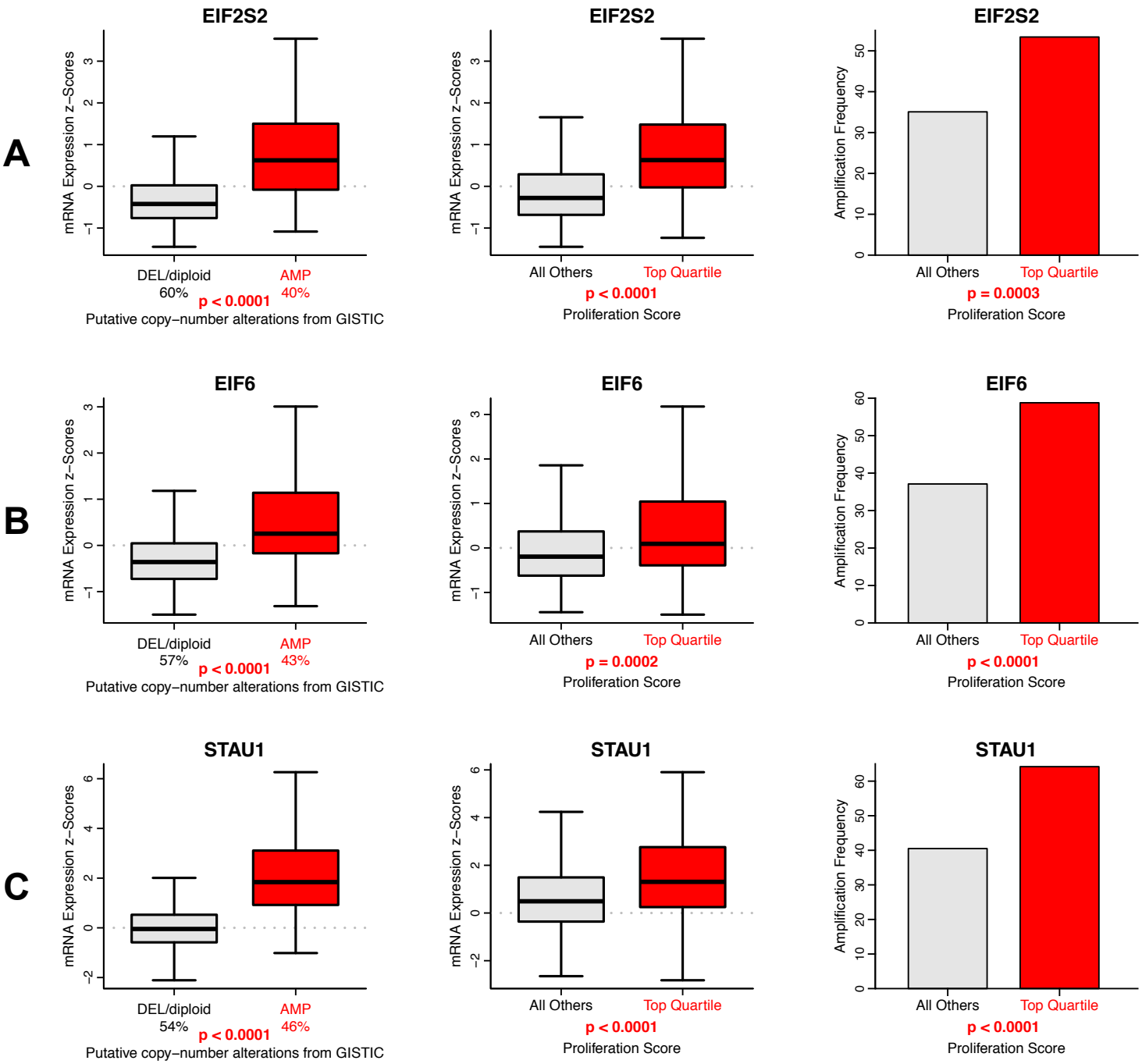
A
EIF2S2
mRNA Expression z−Scores
DEL/diploid
60%
AMP
40%
p < 0.0001
Putative copy−number alterations from GISTIC
EIF2S2
mRNA Expression z−Scores
All Others
Top Quartile
p < 0.0001
Proliferation Score
EIF2S2
Amplification Frequency
All Others
Top Quartile
p = 0.0003
Proliferation Score
B
EIF6
mRNA Expression z−Scores
DEL/diploid
57%
AMP
43%
p < 0.0001
Putative copy−number alterations from GISTIC
EIF6
mRNA Expression z−Scores
All Others
Top Quartile
p = 0.0002
Proliferation Score
EIF6
Amplification Frequency
All Others
Top Quartile
p < 0.0001
Proliferation Score
C
STAU1
mRNA Expression z−Scores
DEL/diploid
54%
AMP
46%
p < 0.0001
Putative copy−number alterations from GISTIC
STAU1
mRNA Expression z−Scores
All Others
Top Quartile
p < 0.0001
Proliferation Score
STAU1
Amplification Frequency
All Others
Top Quartile
p < 0.0001
Proliferation Score

Figure S9. Correlation plots for luminal G9a interactor genes located in a region of high amplification frequency on the q arm of chromosome 20 in luminal TCGA samples, Related to Figure 5.

Luminal G9a interactor genes: (**A**) EIF2S2, (**B**) EIF6, and (**C**) STAU1 on the q arm of chromosome 20. Each row includes the correlation plots for a specific gene. (left) box plots showing the distribution of mRNA expression for luminal samples with GISTIC values of 1 or 2 (AMP) compared to GISTIC values of 0, -1, or -2 (DEL/diploid). The percent of luminal TCGA samples in each group is indicated. The adjusted p-value as determined by a Mann-Whitney-Wilcoxon Test is displayed to indicate the significance of the AMP group having higher mRNA expression. (middle) box plots showing the distribution of mRNA expression for luminal samples with a proliferation score in the top quartile compared to all the other samples. The adjusted p-value as determined by a Mann-Whitney-Wilcoxon Test is displayed to indicate the significance of the Top Quartile group having higher mRNA expression. (right) bar plots showing the frequency of samples with an amplification (GISTIC values of 1 or 2) for the indicated gene for luminal samples with a proliferation score in the top quartile compared to all the other samples. The adjusted p-value as determined by a Fisher's Exact Test for Count Data is displayed to indicate the significance of the Top Quartile group having a greater amplification frequency.

Figure S10

A

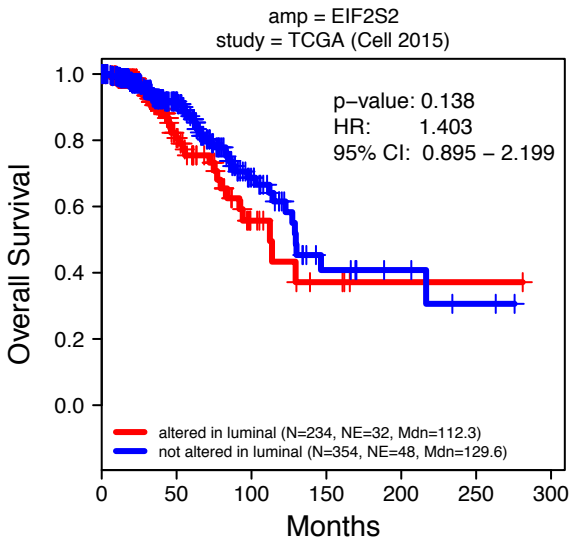

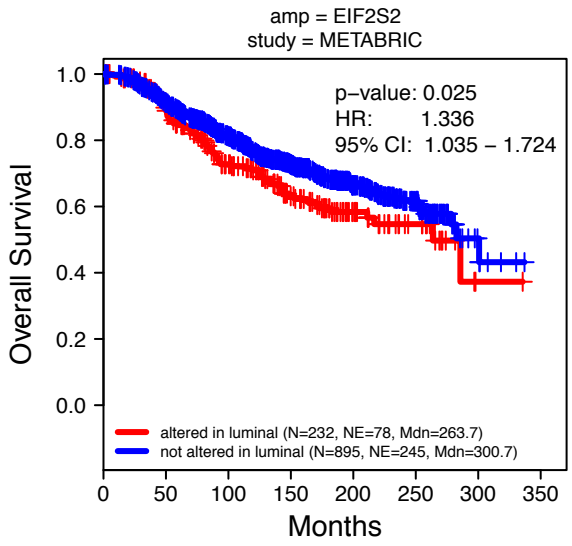

B

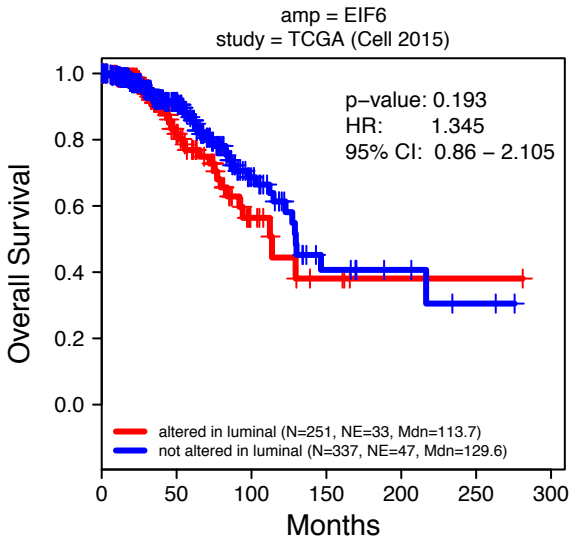

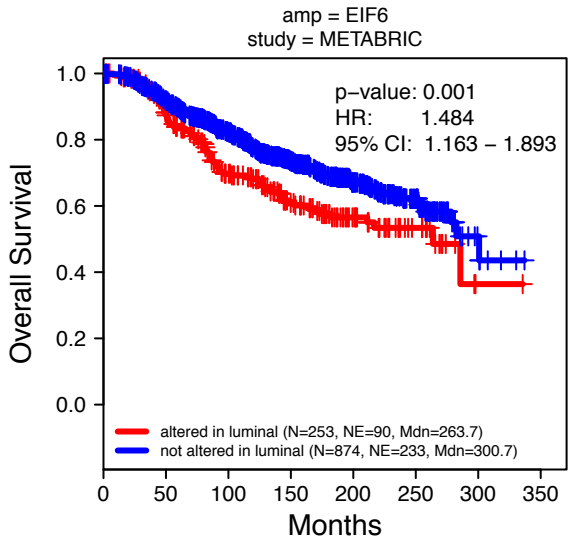

C

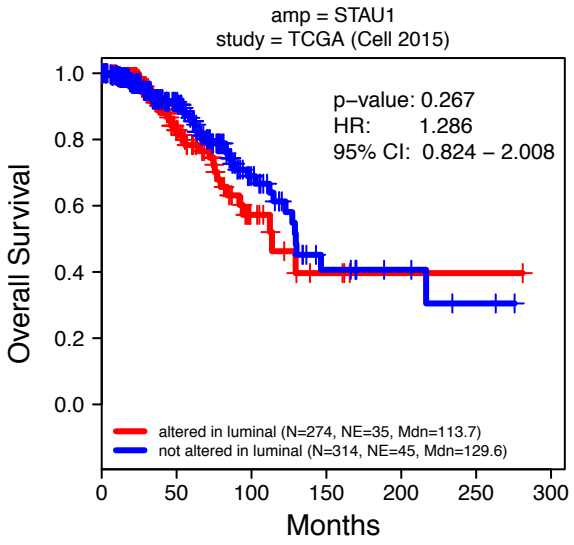

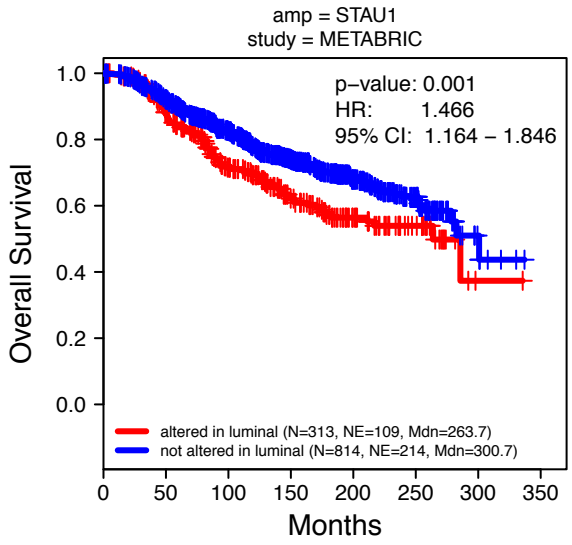

Figure S10. Kaplan-Meier survival analysis plots for luminal samples with copy-number amplification for luminal G9a interactor genes located in a region of high amplification frequency on the q arm of chromosome 20 in luminal TCGA samples, Related to Figure 6.

Luminal G9a interactor genes: (**A**) EIF2S2, (**B**) EIF6, and (**C**) STAU1 on the q arm of chromosome 20. Each row includes the Kaplan-Meier survival plots for a specific gene for luminal samples with copy-number amplification (GISTIC score of 1 or 2) (red line) vs. copy-number deletion or diploid (GISTIC score of 0, -1, or -2) (blue line) in luminal TCGA samples (left) and luminal METABRIC samples (right). For the Kaplan-Meier plots, "N" refers to "Number of samples" and "NE" refers to "Number of Events". The number of events is for OS status = "DECEASED". "Mdn" indicates the median months survival. The log-rank p-value and Hazard Ratio (HR) with 95% Confidence Interval (CI) between the two groups are indicated in each plot.

Figure S11

A

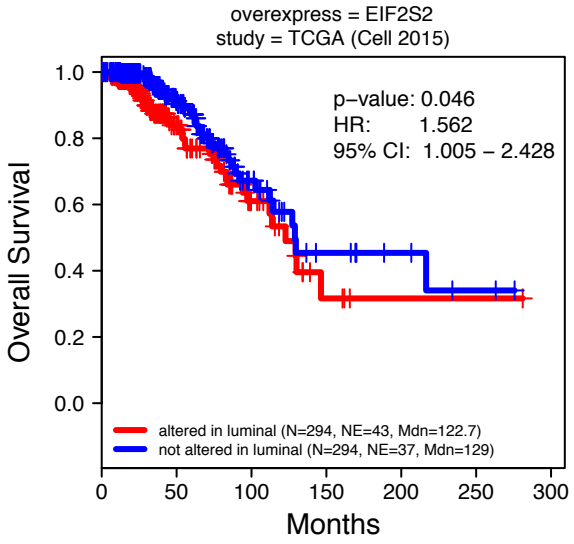

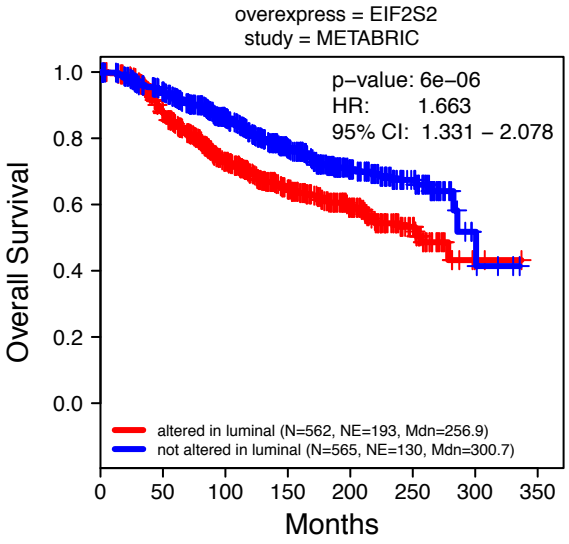

B

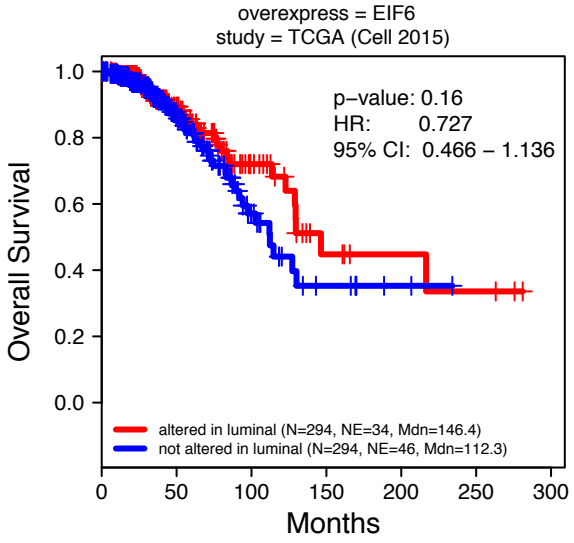

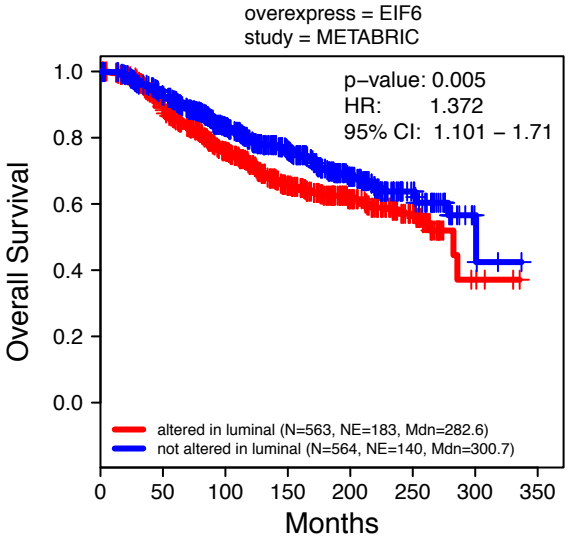

C

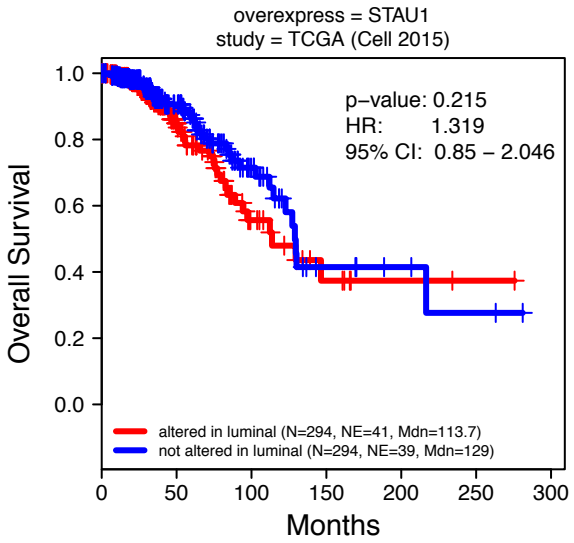

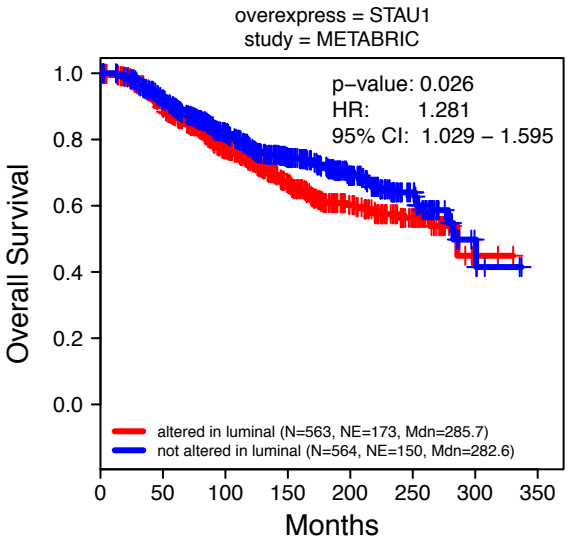

Figure S11. Kaplan-Meier survival analysis plots for luminal samples with mRNA overexpression for luminal G9a interactor genes located in a region of high amplification frequency on the q arm of chromosome 20 in luminal TCGA samples, Related to Figure 6.

Luminal G9a interactor genes: (**A**) EIF2S2, (**B**) EIF6, and (**C**) STAU1 on the q arm of chromosome 20. Each row includes the Kaplan-Meier survival plots for a specific gene for luminal samples with mRNA overexpression (z-score > median z-score) (red line) compared to samples not showing mRNA overexpression (z-score < median z-score) (blue line) in luminal TCGA samples (left) and luminal METABRIC samples (right). For the Kaplan-Meier plots, "N" refers to "Number of samples" and "NE" refers to "Number of Events". The number of events is for OS status = "DECEASED". "Mdn" indicates the median months survival. The log-rank p-value and Hazard Ratio (HR) with 95% Confidence Interval (CI) between the two groups are indicated in each plot.

Figure S12

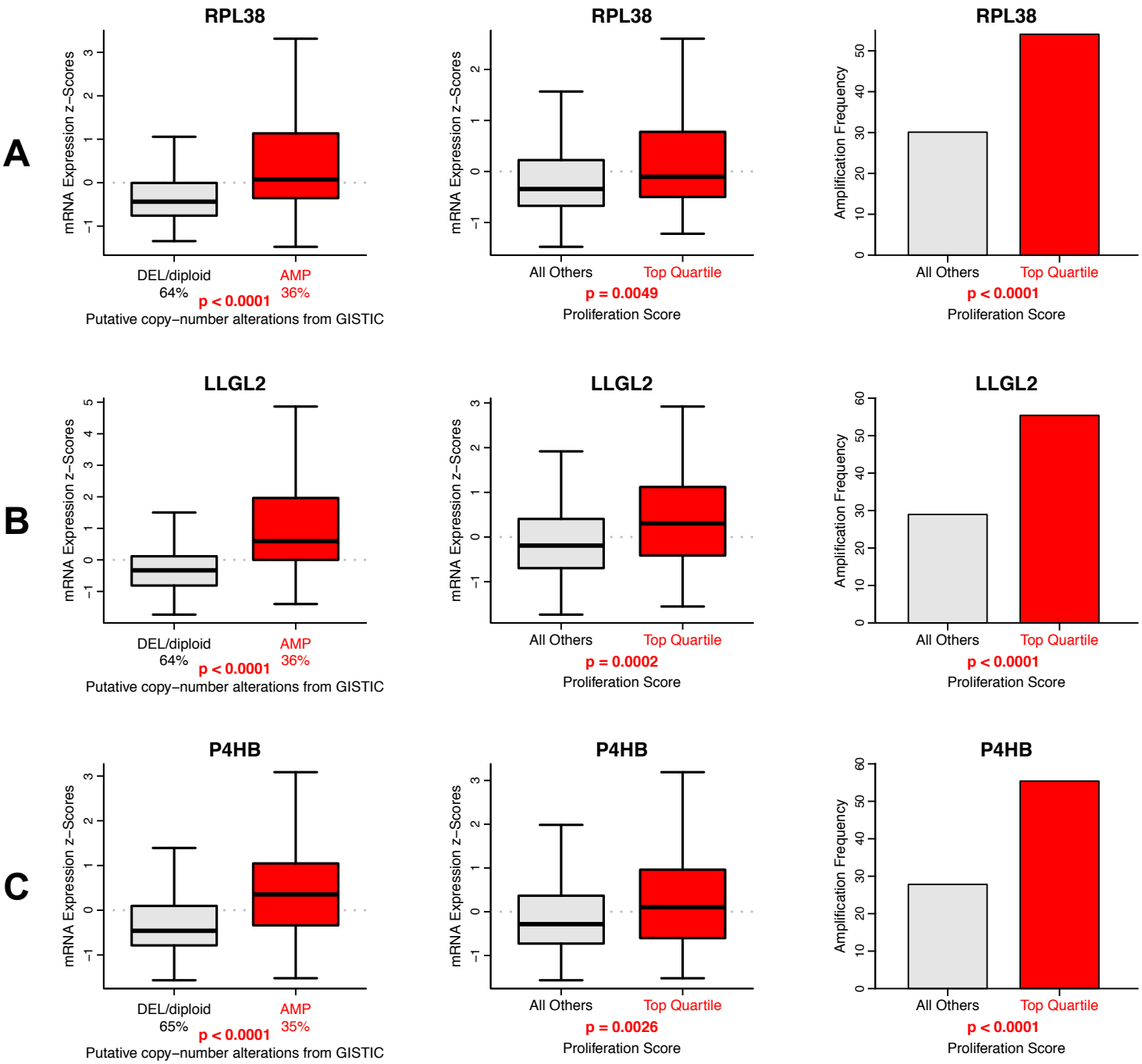
A
RPL38
mRNA Expression z−Scores
DEL/diploid
64%
AMP
36%
p < 0.0001
Putative copy−number alterations from GISTIC
RPL38
mRNA Expression z−Scores
All Others
Top Quartile
p = 0.0049
Proliferation Score
RPL38
Amplification Frequency
All Others
Top Quartile
p < 0.0001
Proliferation Score
B
LLGL2
mRNA Expression z−Scores
DEL/diploid
64%
AMP
36%
p < 0.0001
Putative copy−number alterations from GISTIC
LLGL2
mRNA Expression z−Scores
All Others
Top Quartile
p = 0.0002
Proliferation Score
LLGL2
Amplification Frequency
All Others
Top Quartile
p < 0.0001
Proliferation Score
C
P4HB
mRNA Expression z−Scores
DEL/diploid
65%
AMP
35%
p < 0.0001
Putative copy−number alterations from GISTIC
P4HB
mRNA Expression z−Scores
All Others
Top Quartile
p = 0.0026
Proliferation Score
P4HB
Amplification Frequency
All Others
Top Quartile
p < 0.0001
Proliferation Score

Figure S12. Correlation plots for luminal G9a interactor genes located in regions of high amplification frequency on the q arm of chromosome 17 in luminal TCGA samples, Related to Figure 5.

Luminal G9a interactor genes: (**A**) RPL38, (**B**) LLGL2, and (**C**) P4HB on the q arm of chromosome 17. Each row includes the correlation plots for a specific gene. (left) box plots showing the distribution of mRNA expression for luminal samples with GISTIC values of 1 or 2 (AMP) compared to GISTIC values of 0, -1, or -2 (DEL/diploid). The percent of luminal TCGA samples in each group is indicated. The adjusted p-value as determined by a Mann-Whitney-Wilcoxon Test is displayed to indicate the significance of the AMP group having higher mRNA expression. (middle) box plots showing the distribution of mRNA expression for luminal samples with a proliferation score in the top quartile compared to all the other samples. The adjusted p-value as determined by a Mann-Whitney-Wilcoxon Test is displayed to indicate the significance of the Top Quartile group having higher mRNA expression. (right) bar plots showing the frequency of samples with an amplification (GISTIC values of 1 or 2) for the indicated gene for luminal samples with a proliferation score in the top quartile compared to all the other samples. The adjusted p-value as determined by a Fisher's Exact Test for Count Data is displayed to indicate the significance of the Top Quartile group having a greater amplification frequency.

Figure S13

A

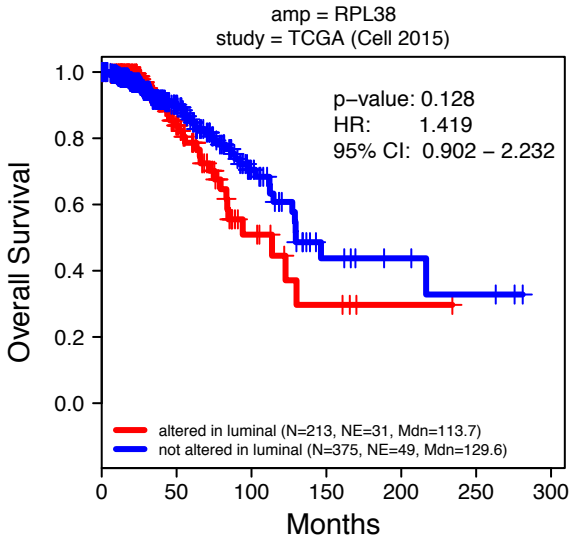

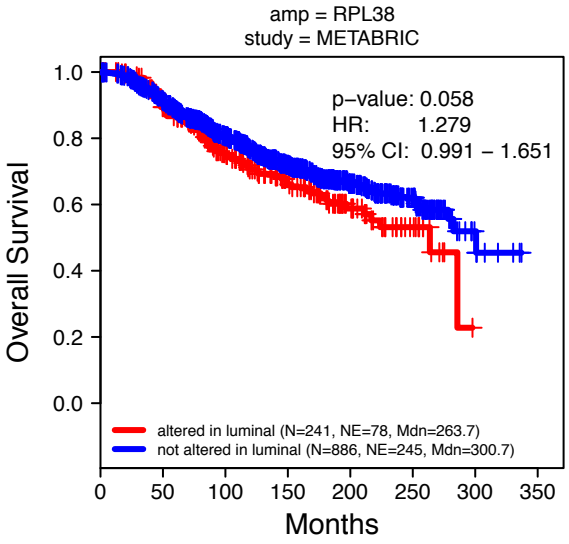

B

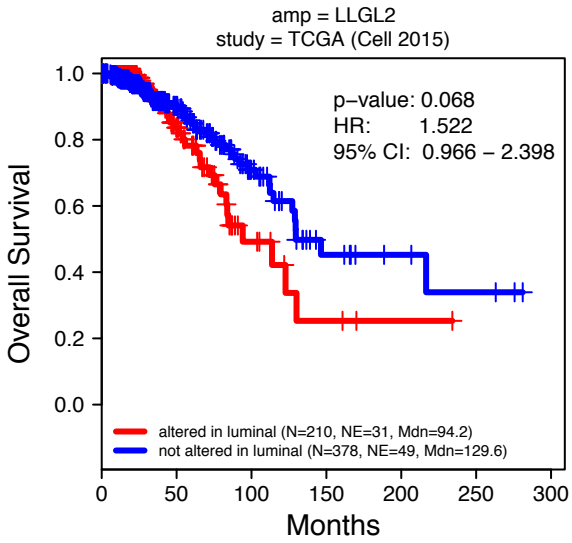

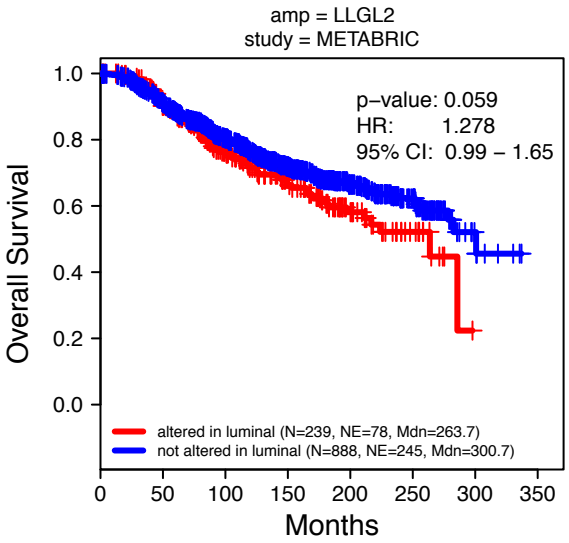

C

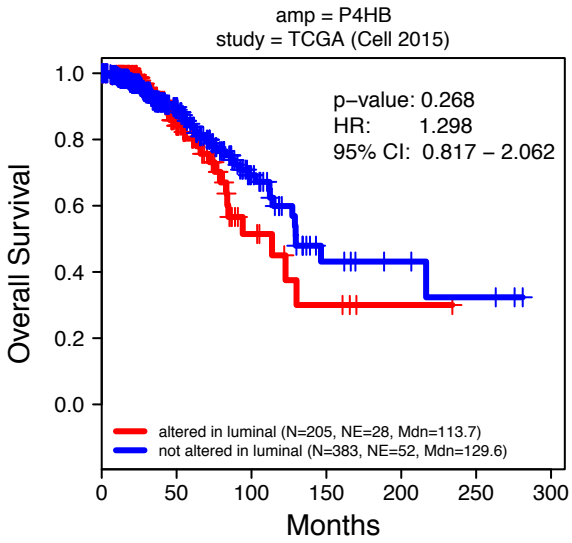

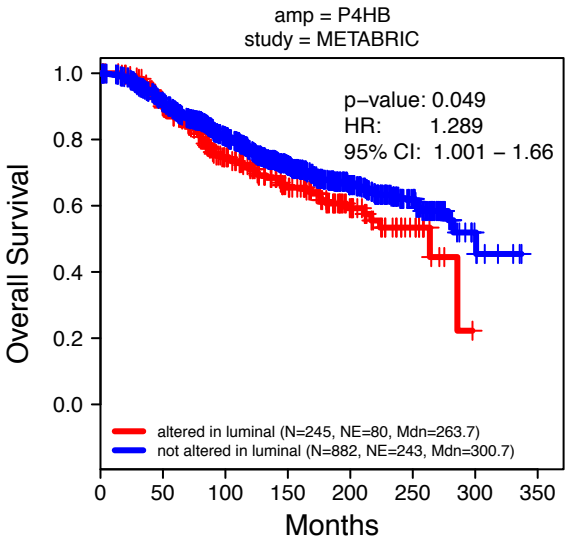

Figure S13. Kaplan-Meier survival analysis plots for luminal samples with copy-number amplification for luminal G9a interactor genes located in a region of high amplification frequency on the q arm of chromosome 17 in luminal TCGA samples, Related to Figure 6.

Luminal G9a interactor genes: (**A**) RPL38, (**B**) LLGL2, and (**C**) P4HB on the q arm of chromosome 17. Each row includes the Kaplan-Meier survival plots for a specific gene for luminal samples with copy-number amplification (GISTIC score of 1 or 2) (red line) vs. copy-number deletion or diploid (GISTIC score of 0, -1, or -2) (blue line) in luminal TCGA samples (left) and luminal METABRIC samples (right). For the Kaplan-Meier plots, "N" refers to "Number of samples" and "NE" refers to "Number of Events". The number of events is for OS status = "DECEASED". "Mdn" indicates the median months survival. The log-rank p-value and Hazard Ratio (HR) with 95% Confidence Interval (CI) between the two groups are indicated in each plot.

Figure S14

A

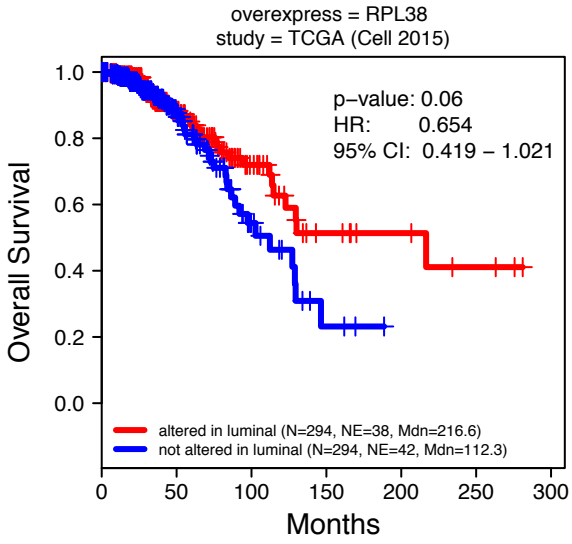

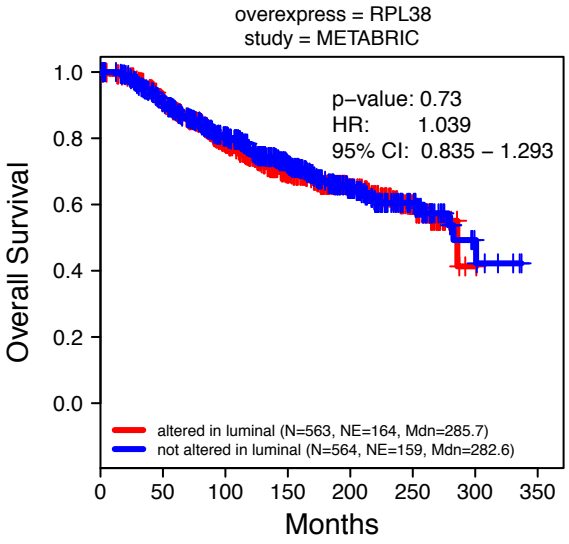

B

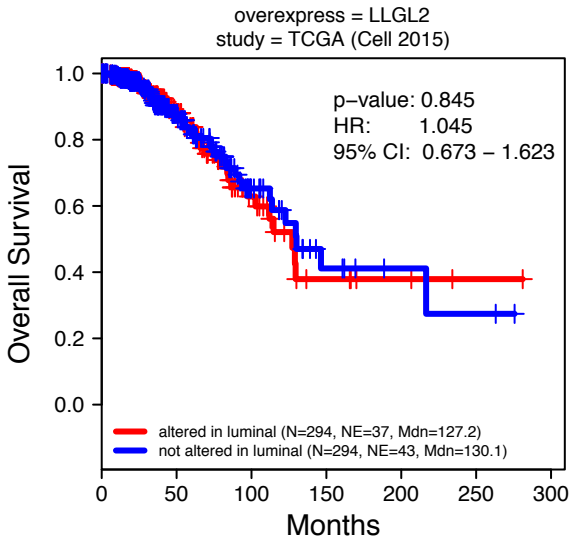

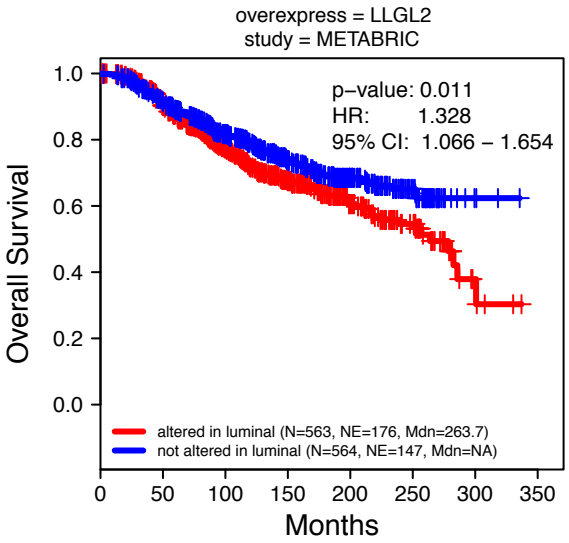

C

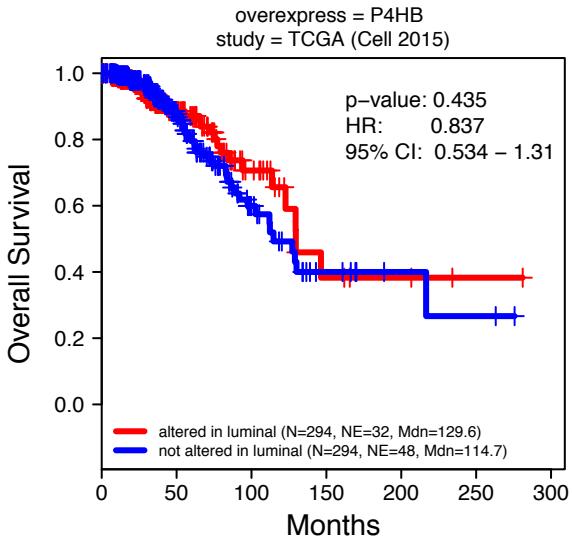

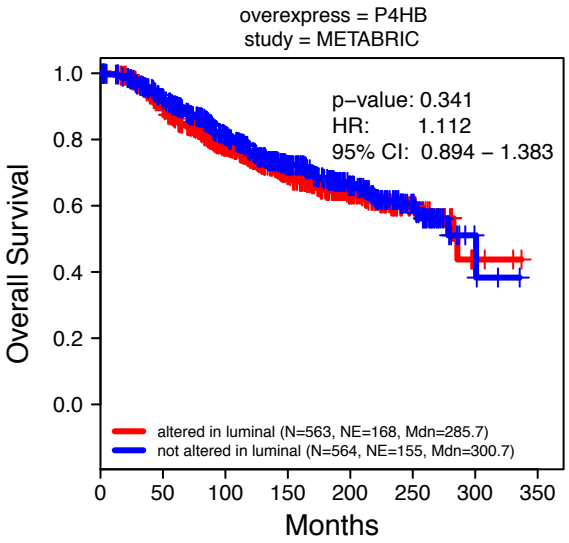

Figure S14. Kaplan-Meier survival analysis plots for luminal samples with mRNA overexpression for luminal G9a interactor genes located in a region of high amplification frequency on the q arm of chromosome 17 in luminal TCGA samples, Related to Figure 6.

Luminal G9a interactor genes: (**A**) RPL38, (**B**) LLGL2, and (**C**) P4HB on the q arm of chromosome 17. Each row includes the Kaplan-Meier survival plots for a specific gene for luminal samples with mRNA overexpression (z-score > median z-score) (red line) compared to samples not showing mRNA overexpression (z-score < median z-score) (blue line) in luminal TCGA samples (left) and luminal METABRIC samples (right). For the Kaplan-Meier plots, "N" refers to "Number of samples" and "NE" refers to "Number of Events". The number of events is for OS status = "DECEASED". "Mdn" indicates the median months survival. The log-rank p-value and Hazard Ratio (HR) with 95% Confidence Interval (CI) between the two groups are indicated in each plot.

Figure S15

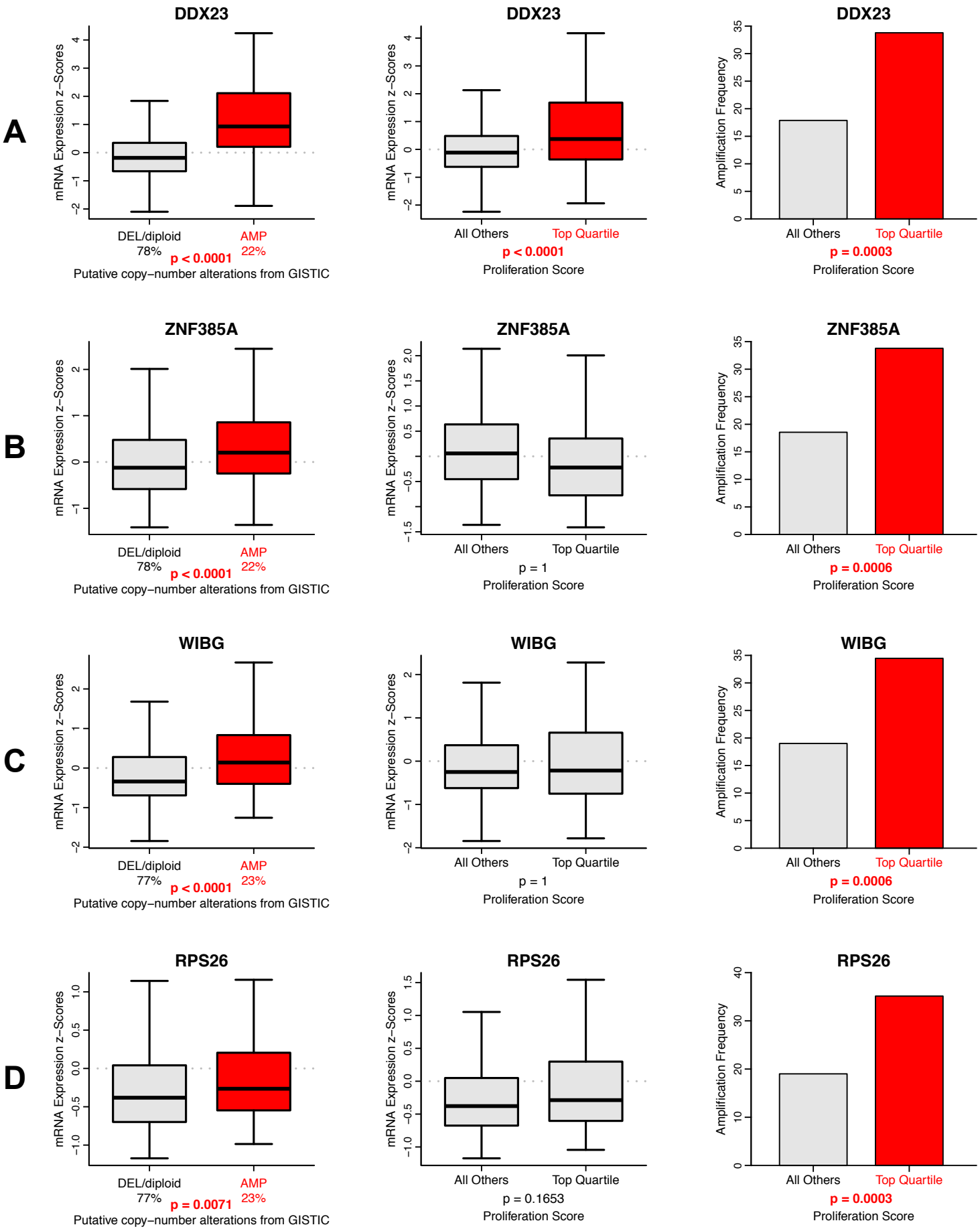
A
DDX23
mRNA Expression z−Scores
DEL/diploid
78%
AMP
22%
p < 0.0001
Putative copy−number alterations from GISTIC
DDX23
mRNA Expression z−Scores
All Others
Top Quartile
p < 0.0001
Proliferation Score
DDX23
Amplification Frequency
All Others
Top Quartile
p = 0.0003
Proliferation Score
B
ZNF385A
mRNA Expression z−Scores
DEL/diploid
78%
AMP
22%
p < 0.0001
Putative copy−number alterations from GISTIC
ZNF385A
mRNA Expression z−Scores
All Others
Top Quartile
p = 1
Proliferation Score
ZNF385A
Amplification Frequency
All Others
Top Quartile
p = 0.0006
Proliferation Score
C
WIBG
mRNA Expression z−Scores
DEL/diploid
77%
AMP
23%
p < 0.0001
Putative copy−number alterations from GISTIC
WIBG
mRNA Expression z−Scores
All Others
Top Quartile
p = 1
Proliferation Score
WIBG
Amplification Frequency
All Others
Top Quartile
p = 0.0006
Proliferation Score
D
RPS26
mRNA Expression z−Scores
DEL/diploid
77%
AMP
23%
p = 0.0071
Putative copy−number alterations from GISTIC
RPS26
mRNA Expression z−Scores
All Others
Top Quartile
p = 0.1653
Proliferation Score
RPS26
Amplification Frequency
All Others
Top Quartile
p = 0.0003
Proliferation Score

Figure S15. Correlation plots for luminal G9a interactor genes located in a region on the q arm of chromosome 12 in luminal TCGA samples, Related to Figure 5.

Luminal G9a interactor genes: (**A**) DDX23, (**B**) ZNF385A, (**C**) WIBG, and (**D**) RPS26 on the q arm of chromosome 12. Each row includes the correlation plots for a specific gene. (left) box plots showing the distribution of mRNA expression for luminal samples with GISTIC values of 1 or 2 (AMP) compared to GISTIC values of 0, -1, or -2 (DEL/diploid). The percent of luminal TCGA samples in each group is indicated. The adjusted p-value as determined by a Mann-Whitney-Wilcoxon Test is displayed to indicate the significance of the AMP group having higher mRNA expression. (middle) box plots showing the distribution of mRNA expression for luminal samples with a proliferation score in the top quartile compared to all the other samples. The adjusted p-value as determined by a Mann-Whitney-Wilcoxon Test is displayed to indicate the significance of the Top Quartile group having higher mRNA expression. (right) bar plots showing the frequency of samples with an amplification (GISTIC values of 1 or 2) for the indicated gene for luminal samples with a proliferation score in the top quartile compared to all the other samples. The adjusted p-value as determined by a Fisher's Exact Test for Count Data is displayed to indicate the significance of the Top Quartile group having a greater amplification frequency.

Figure S16

A

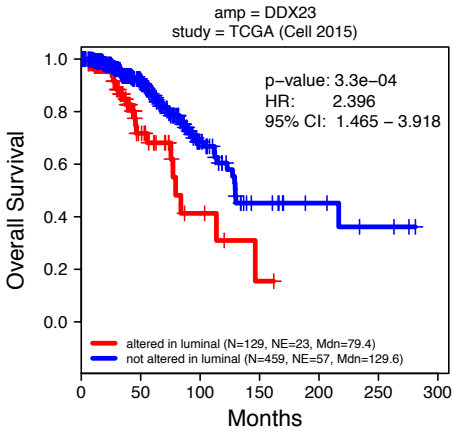

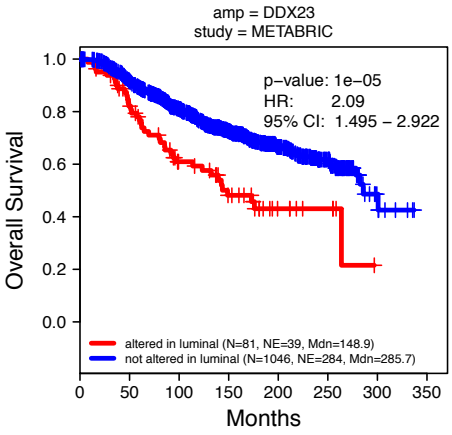

B

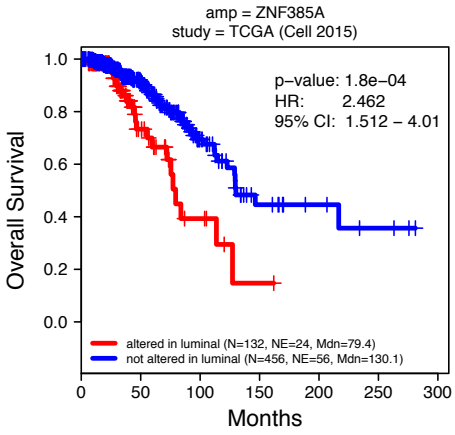

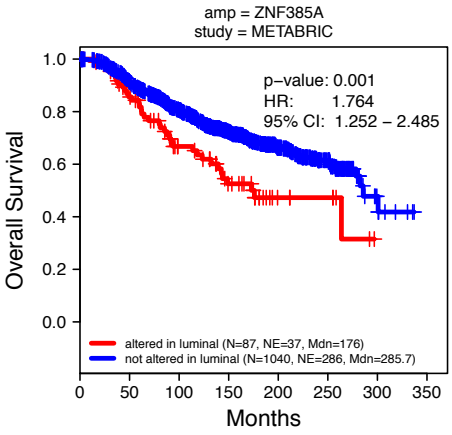

C

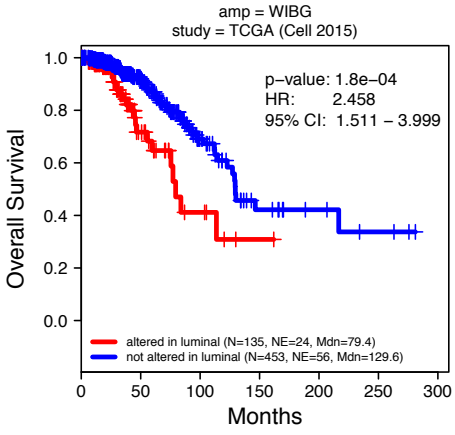

D

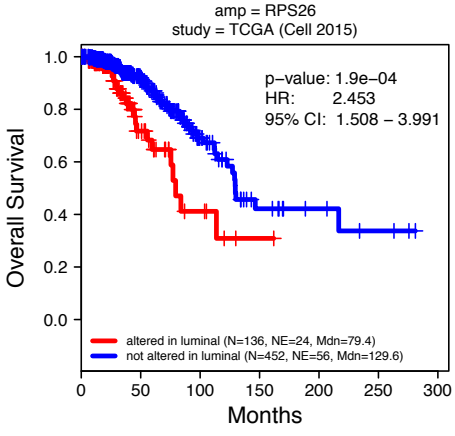

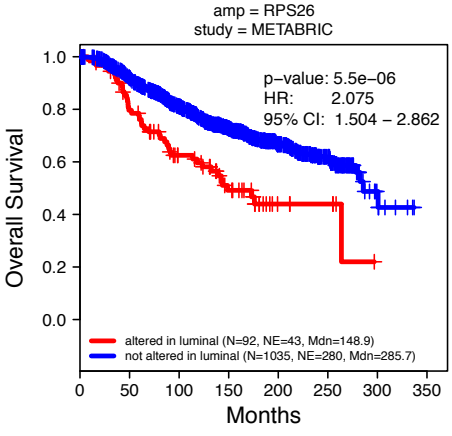

Figure S16. Kaplan-Meier survival analysis plots for luminal samples with copy-number amplification for luminal G9a interactor genes located in a region on the q arm of chromosome 12 in luminal TCGA samples, Related to Figure 6.

Luminal G9a interactor genes: (**A**) DDX23, (**B**) ZNF385A, (**C**) WIBG (no data in METABRIC), and (**D**) RPS26 on the q arm of chromosome 12. Each row includes the Kaplan-Meier survival plots for a specific gene for luminal samples with copy-number amplification (GISTIC score of 1 or 2) (red line) vs. copy-number deletion or diploid (GISTIC score of 0, -1, or -2) (blue line) in luminal TCGA samples (left) and luminal METABRIC samples (right). For the Kaplan-Meier plots, "N" refers to "Number of samples" and "NE" refers to "Number of Events". The number of events is for OS status = "DECEASED". "Mdn" indicates the median months survival. The log-rank p-value and Hazard Ratio (HR) with 95% Confidence Interval (CI) between the two groups are indicated in each plot.

Figure S17

A

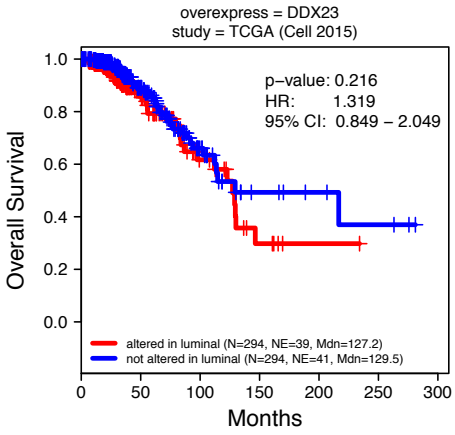

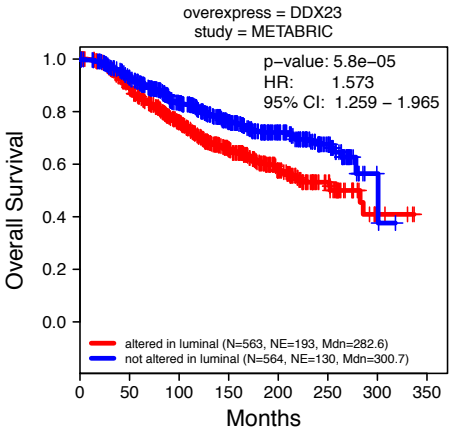

B

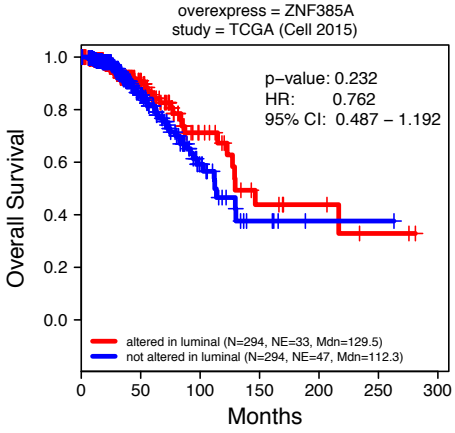

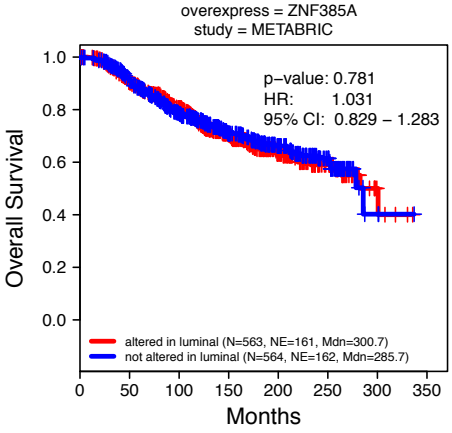

C

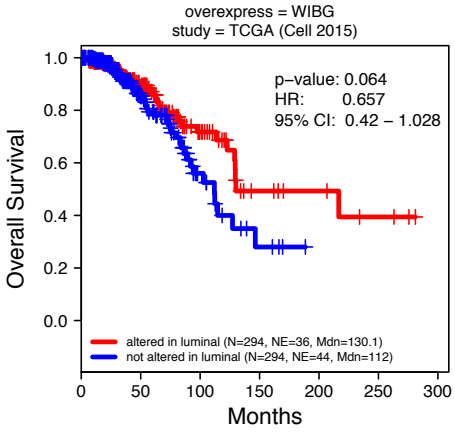

D

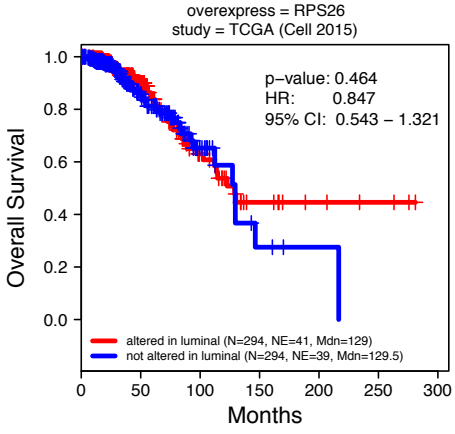

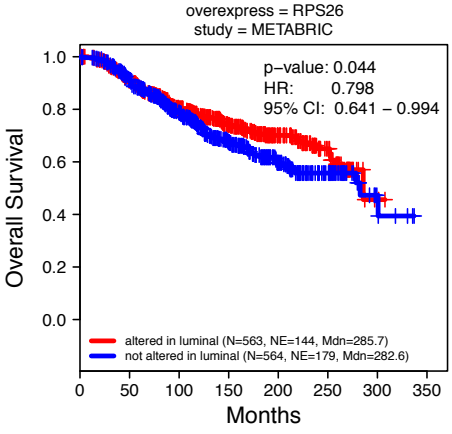

Figure S17. Kaplan-Meier survival analysis plots for luminal samples with mRNA overexpression for luminal G9a interactor genes located in a region on the q arm of chromosome 12 in luminal TCGA samples, Related to Figure 6.

Luminal G9a interactor genes: (**A**) DDX23, (**B**) ZNF385A, (**C**) WIBG (no data in METABRIC), and (**D**) RPS26 on the q arm of chromosome 12. Each row includes the Kaplan-Meier survival plots for a specific gene for luminal samples with mRNA overexpression (z-score > median z-score) (red line) compared to samples not showing mRNA overexpression (z-score < median z-score) (blue line) in luminal TCGA samples (left) and luminal METABRIC samples (right). For the Kaplan-Meier plots, "N" refers to "Number of samples" and "NE" refers to "Number of Events". The number of events is for OS status = "DECEASED". "Mdn" indicates the median months survival. The log-rank p-value and Hazard Ratio (HR) with 95% Confidence Interval (CI) between the two groups are indicated in each plot.

Figure S18

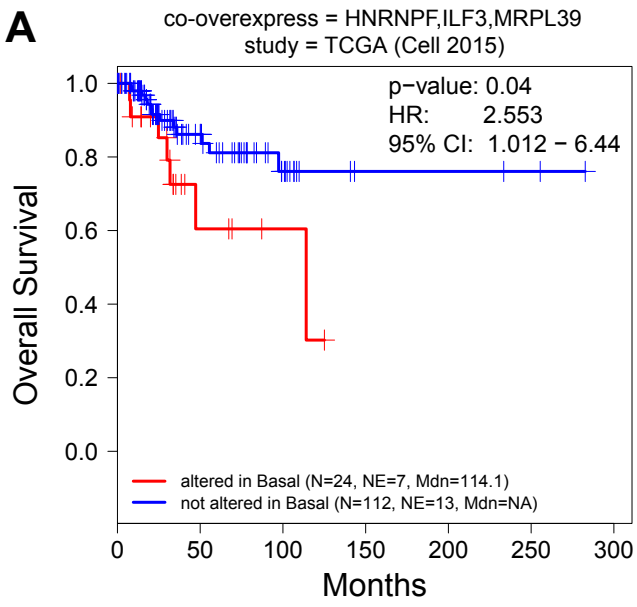
A
co-overexpress = HNRNPF,ILF3,MRPL39
study = TCGA (Cell 2015)
p−value: 0.04
HR: 2.553
95% CI: 1.012 − 6.44
Overall Survival
Months
altered in Basal (N=24, NE=7, Mdn=114.1)
not altered in Basal (N=112, NE=13, Mdn=NA)

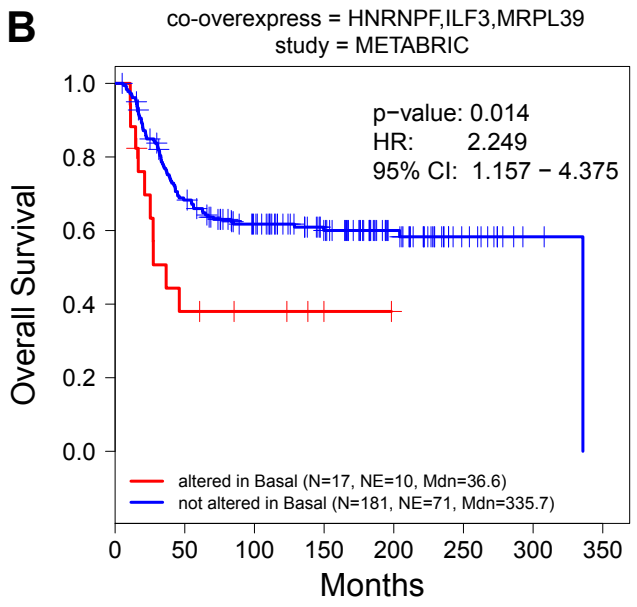
B
co-overexpress = HNRNPF,ILF3,MRPL39
study = METABRIC
p−value: 0.014
HR: 2.249
95% CI: 1.157 − 4.375
Overall Survival
Months
altered in Basal (N=17, NE=10, Mdn=36.6)
not altered in Basal (N=181, NE=71, Mdn=335.7)

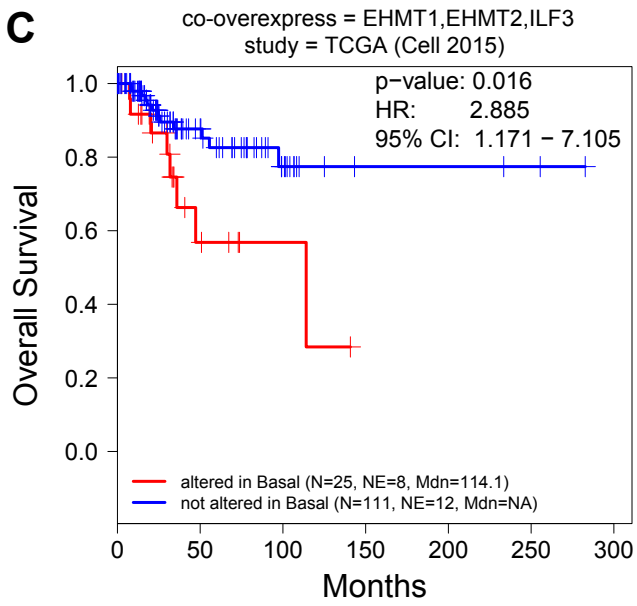
C
co-overexpress = EHMT1,EHMT2,ILF3
study = TCGA (Cell 2015)
p−value: 0.016
HR: 2.885
95% CI: 1.171 − 7.105
Overall Survival
Months
altered in Basal (N=25, NE=8, Mdn=114.1)
not altered in Basal (N=111, NE=12, Mdn=NA)

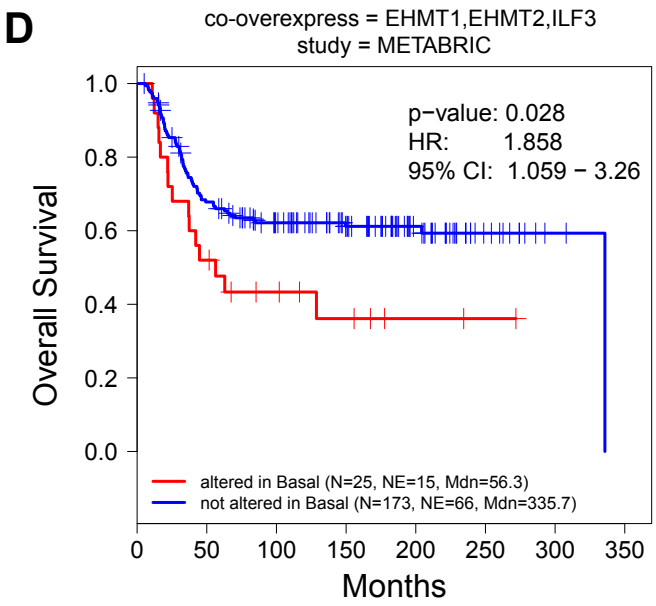
D
co-overexpress = EHMT1,EHMT2,ILF3
study = METABRIC
p−value: 0.028
HR: 1.858
95% CI: 1.059 − 3.26
Overall Survival
Months
altered in Basal (N=25, NE=15, Mdn=56.3)
not altered in Basal (N=173, NE=66, Mdn=335.7)

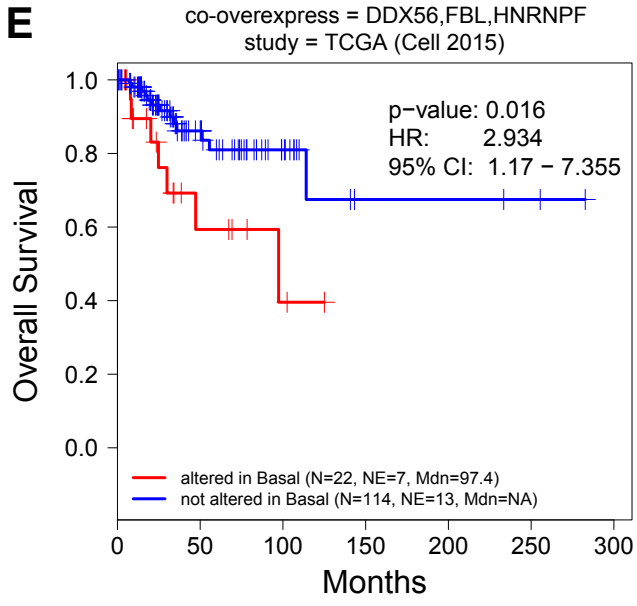
E
co-overexpress = DDX56,FBL,HNRNPF
study = TCGA (Cell 2015)
p−value: 0.016
HR: 2.934
95% CI: 1.17 − 7.355
Overall Survival
Months
altered in Basal (N=22, NE=7, Mdn=97.4)
not altered in Basal (N=114, NE=13, Mdn=NA)

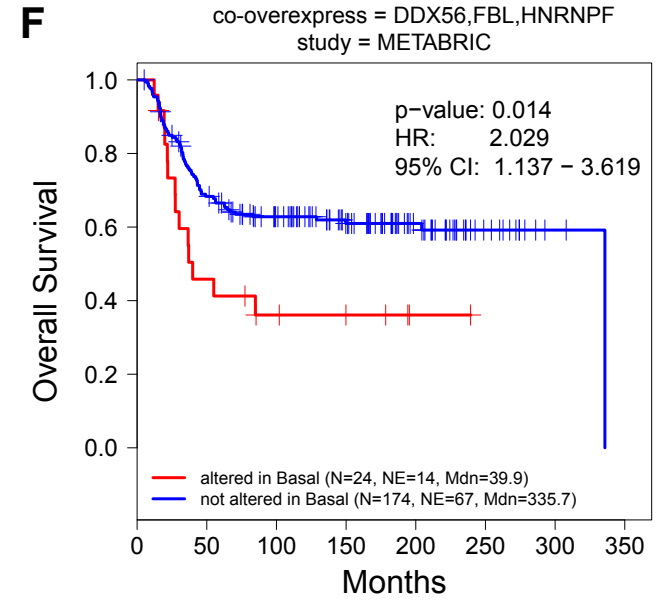
F
co-overexpress = DDX56,FBL,HNRNPF
study = METABRIC
p−value: 0.014
HR: 2.029
95% CI: 1.137 − 3.619
Overall Survival
Months
altered in Basal (N=24, NE=14, Mdn=39.9)
not altered in Basal (N=174, NE=67, Mdn=335.7)

Figure S18. Kaplan-Meier survival analysis for combinations of basal G9a interactors genes showing poor prognosis when co-overexpressed (mRNA expression Z score > median z score for all genes in the combination) in basal patients in both the TCGA and METABRIC datasets, Related to Figure 8.

Kaplan-Meier survival analysis indicates that altered mRNA expression of G9a interactor genes is prognostically significant in marking distinct patient subpopulations within single PAM50 subtypes. (**A, C, & E**) Overall survival (OS) plots of TCGA patients with the BLBC subtype (n=136). (**B, D, & F**) Overall survival (OS) plots of METABRIC patients with the BLBC subtype (n=198). The altered group (red line) is samples with mRNA co-overexpression (z-score > median z-score for all genes in the combination) for HNRNPF, ILF3, and MRPL39 (panels **A & B**), EHMT1, EHMT2, and ILF3 (panels **C & D**), and DDX56, FBL, and HNRNPF (panels **E & F**). The non-altered group (blue line) is the remaining samples not showing mRNA co-overexpression for the same genes. "N" refers to "Number of samples" and "NE" refers to "Number of Events". The number of events is for OS status = "DECEASED". "Mdn" indicates the median months survival. The log-rank p-value and Hazard Ratio (HR) with 95% Confidence Interval (CI) between the two groups are indicated in each plot.

Figure S19

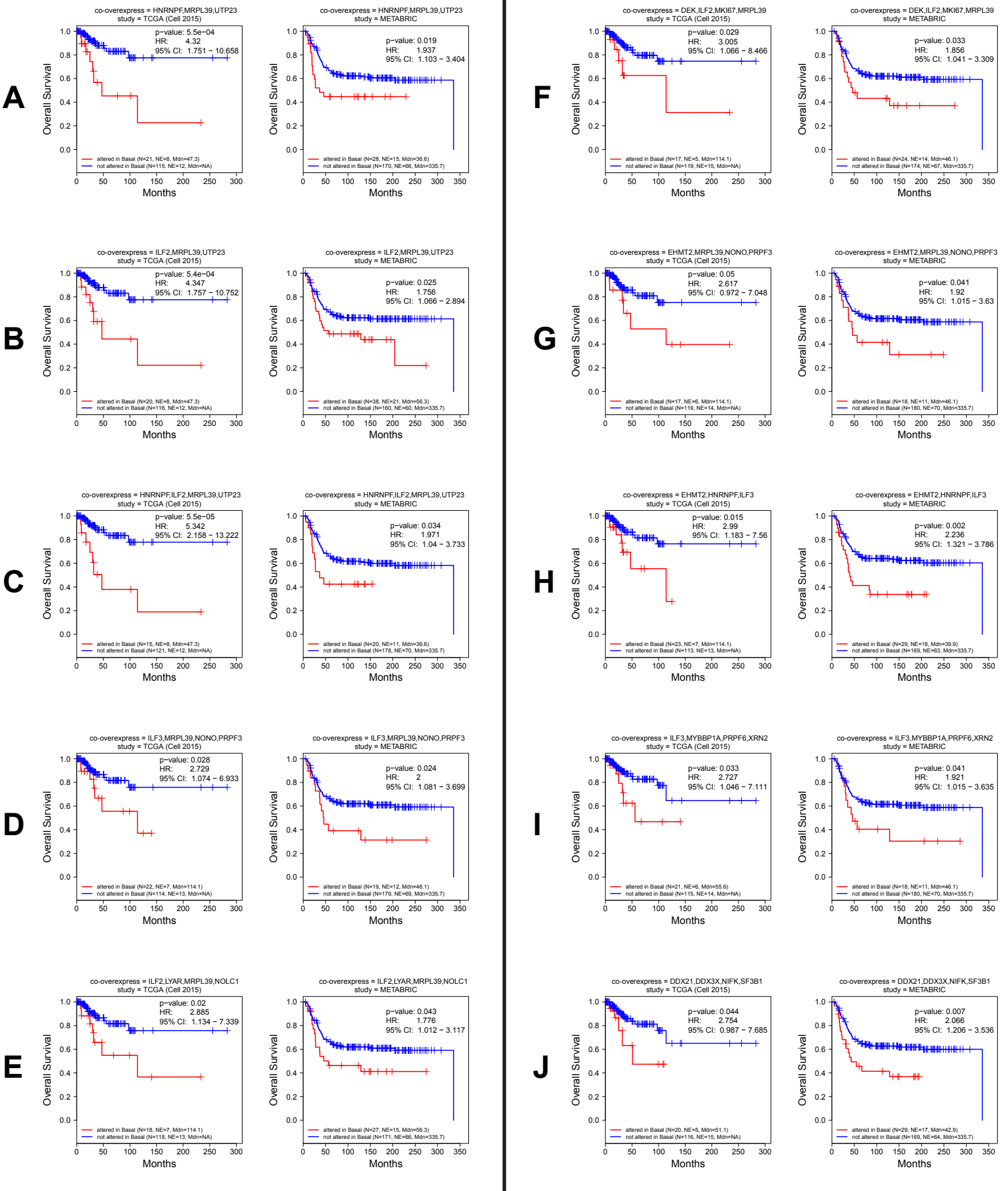
A
co-overexpress = HNRNPF,MRPL39,UTP23
study = TCGA (Cell 2015)
p−value: 5.5e−04
HR: 4.32
95% CI: 1.751 − 10.658
altered in Basal (N=21, NE=8, Mdn=47.3)
not altered in Basal (N=115, NE=12, Mdn=NA)
co-overexpress = HNRNPF,MRPL39,UTP23
study = METABRIC
p−value: 0.019
HR: 1.937
95% CI: 1.103 − 3.404
altered in Basal (N=28, NE=15, Mdn=36.6)
not altered in Basal (N=170, NE=66, Mdn=335.7)
B
co-overexpress = ILF2,MRPL39,UTP23
study = TCGA (Cell 2015)
p−value: 5.4e−04
HR: 4.347
95% CI: 1.757 − 10.752
altered in Basal (N=20, NE=8, Mdn=47.3)
not altered in Basal (N=116, NE=12, Mdn=NA)
co-overexpress = ILF2,MRPL39,UTP23
study = METABRIC
p−value: 0.025
HR: 1.756
95% CI: 1.066 − 2.894
altered in Basal (N=38, NE=21, Mdn=56.3)
not altered in Basal (N=160, NE=60, Mdn=335.7)
C
co-overexpress = HNRNPF,ILF2,MRPL39,UTP23
study = TCGA (Cell 2015)
p−value: 5.5e−05
HR: 5.342
95% CI: 2.158 − 13.222
altered in Basal (N=15, NE=8, Mdn=47.3)
not altered in Basal (N=121, NE=12, Mdn=NA)
co-overexpress = HNRNPF,ILF2,MRPL39,UTP23
study = METABRIC
p−value: 0.034
HR: 1.971
95% CI: 1.04 − 3.733
altered in Basal (N=20, NE=11, Mdn=36.6)
not altered in Basal (N=178, NE=70, Mdn=335.7)
D
co-overexpress = ILF3,MRPL39,NONO,PRPF3
study = TCGA (Cell 2015)
p−value: 0.028
HR: 2.729
95% CI: 1.074 − 6.933
altered in Basal (N=22, NE=7, Mdn=114.1)
not altered in Basal (N=114, NE=13, Mdn=NA)
co-overexpress = ILF3,MRPL39,NONO,PRPF3
study = METABRIC
p−value: 0.024
HR: 2
95% CI: 1.081 − 3.699
altered in Basal (N=19, NE=12, Mdn=46.1)
not altered in Basal (N=179, NE=69, Mdn=335.7)
E
co-overexpress = ILF2,LYAR,MRPL39,NOLC1
study = TCGA (Cell 2015)
p−value: 0.02
HR: 2.885
95% CI: 1.134 − 7.339
altered in Basal (N=18, NE=7, Mdn=114.1)
not altered in Basal (N=118, NE=13, Mdn=NA)
co-overexpress = ILF2,LYAR,MRPL39,NOLC1
study = METABRIC
p−value: 0.043
HR: 1.776
95% CI: 1.012 − 3.117
altered in Basal (N=27, NE=15, Mdn=56.3)
not altered in Basal (N=171, NE=66, Mdn=335.7)
F
co-overexpress = DEK,ILF2,MKI67,MRPL39
study = TCGA (Cell 2015)
p−value: 0.029
HR: 3.005
95% CI: 1.066 − 8.466
altered in Basal (N=17, NE=5, Mdn=114.1)
not altered in Basal (N=119, NE=15, Mdn=NA)
co-overexpress = DEK,ILF2,MKI67,MRPL39
study = METABRIC
p−value: 0.033
HR: 1.856
95% CI: 1.041 − 3.309
altered in Basal (N=24, NE=14, Mdn=46.1)
not altered in Basal (N=174, NE=67, Mdn=335.7)
G
co-overexpress = EHMT2,MRPL39,NONO,PRPF3
study = TCGA (Cell 2015)
p−value: 0.05
HR: 2.617
95% CI: 0.972 − 7.048
altered in Basal (N=17, NE=6, Mdn=114.1)
not altered in Basal (N=119, NE=14, Mdn=NA)
co-overexpress = EHMT2,MRPL39,NONO,PRPF3
study = METABRIC
p−value: 0.041
HR: 1.92
95% CI: 1.015 − 3.63
altered in Basal (N=18, NE=11, Mdn=46.1)
not altered in Basal (N=180, NE=70, Mdn=335.7)
H
co-overexpress = EHMT2,HNRNPF,ILF3
study = TCGA (Cell 2015)
p−value: 0.015
HR: 2.99
95% CI: 1.183 − 7.56
altered in Basal (N=23, NE=7, Mdn=114.1)
not altered in Basal (N=113, NE=13, Mdn=NA)
co-overexpress = EHMT2,HNRNPF,ILF3
study = METABRIC
p−value: 0.002
HR: 2.236
95% CI: 1.321 − 3.786
altered in Basal (N=29, NE=18, Mdn=39.9)
not altered in Basal (N=169, NE=63, Mdn=335.7)
I
co-overexpress = ILF3,MYBBP1A,PRPF6,XRN2
study = TCGA (Cell 2015)
p−value: 0.033
HR: 2.727
95% CI: 1.046 − 7.111
altered in Basal (N=21, NE=6, Mdn=55.6)
not altered in Basal (N=115, NE=14, Mdn=NA)
co-overexpress = ILF3,MYBBP1A,PRPF6,XRN2
study = METABRIC
p−value: 0.041
HR: 1.921
95% CI: 1.015 − 3.635
altered in Basal (N=18, NE=11, Mdn=46.1)
not altered in Basal (N=180, NE=70, Mdn=335.7)
J
co-overexpress = DDX21,DDX3X,NIFK,SF3B1
study = TCGA (Cell 2015)
p−value: 0.044
HR: 2.754
95% CI: 0.987 − 7.685
altered in Basal (N=20, NE=5, Mdn=51.1)
not altered in Basal (N=116, NE=15, Mdn=NA)
co-overexpress = DDX21,DDX3X,NIFK,SF3B1
study = METABRIC
p−value: 0.007
HR: 2.066
95% CI: 1.206 − 3.536
altered in Basal (N=29, NE=17, Mdn=42.9)
not altered in Basal (N=169, NE=64, Mdn=335.7)
Overall Survival
Months

Figure S19. Additional examples of Kaplan-Meier survival analysis for combinations of basal G9a interactors genes showing poor prognosis when co-overexpressed (mRNA expression Z score > median z score for all genes in the combination) in basal patients in both the TCGA and METABRIC datasets, Related to Figure 8.

Each panel represents a combination of basal G9a interactors with overall survival (OS) plots of TCGA patients with the BLBC subtype (N=136) displayed on the left and overall survival (OS) plots of METABRIC patients with the BLBC subtype (N=198) displayed on the right. The altered group (red line) is samples with mRNA co-overexpression (z-score > median z-score for all genes in the combination) for the indicated G9a interactor genes: (**A**) HNRNPF, MRPL39, and UTP23, (**B**) ILF2, MRPL39, and UTP23, (**C**) HNRNPF, ILF2, MRPL39, and UTP23, (**D**) ILF3, MRPL39, NONO, and PRPF3, (**E**) ILF2, LYAR, MRPL39, and NOLC1, (**F**) DEK, ILF2, MKI67, and MRPL39, (**G**) EHMT2, MRPL39, NONO, and PRPF3, (**H**) EHMT2, HNRNPF, and ILF3, (**I**) ILF3, MYBBP1A, PRPF6, and XRN2, (**J**) DDX21, DDX3X, NIFK, and SF3B1. The non-altered group (blue line) is the remaining samples not showing co-overexpression for the same genes. "N" refers to "Number of samples" and "NE" refers to "Number of Events". The number of events is for OS status = "DECEASED". "Mdn" indicates the median months survival. The log-rank p-value and Hazard Ratio (HR) with 95% Confidence Interval (CI) between the two groups are indicated in each plot.

Figure S20

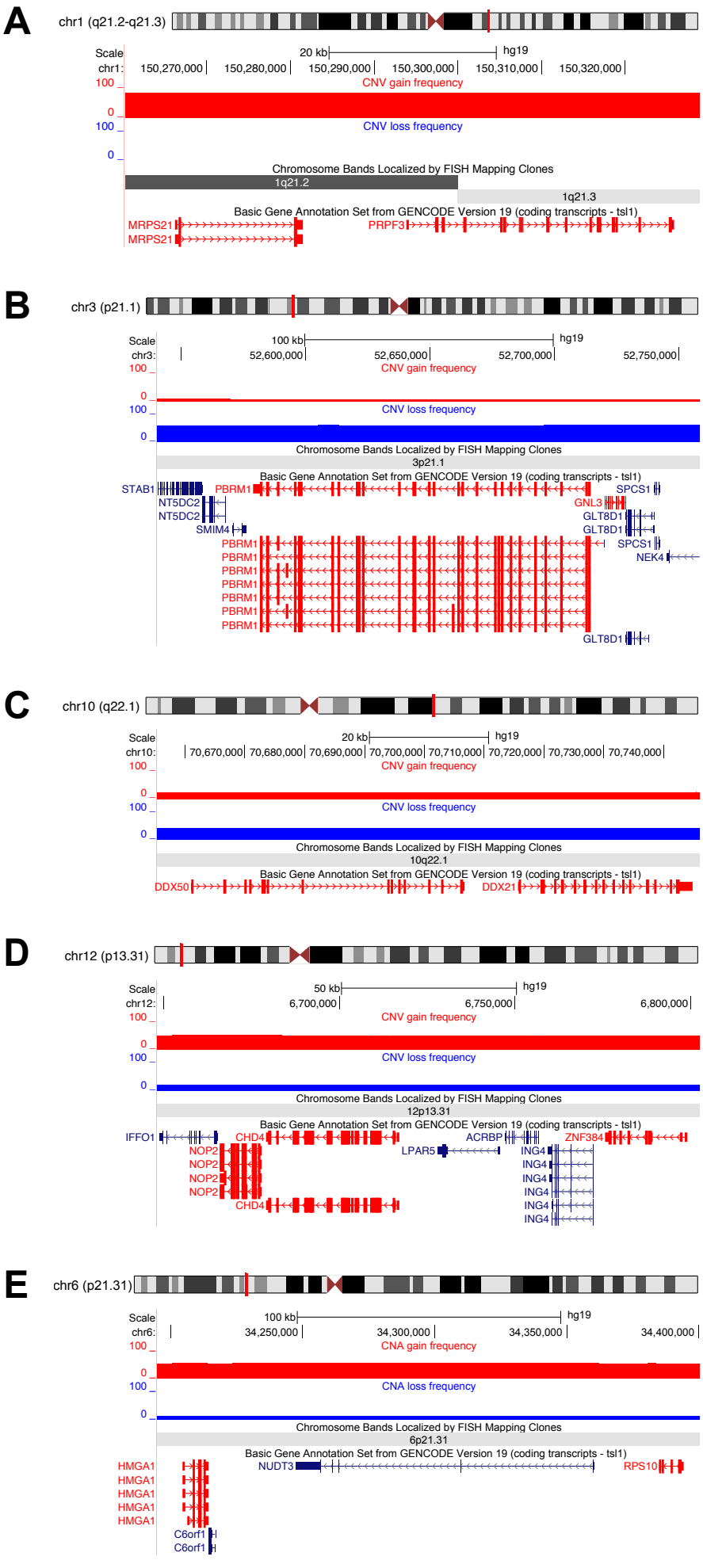
A
chr1 (q21.2-q21.3)
Scale
chr1:
20 kb
hg19
150,270,000
150,280,000
150,290,000
150,300,000
150,310,000
150,320,000
100
CNV gain frequency
0
100
CNV loss frequency
0
Chromosome Bands Localized by FISH Mapping Clones
1q21.2
1q21.3
Basic Gene Annotation Set from GENCODE Version 19 (coding transcripts - tsl1)
MRPS21
MRPS21
PRPF3
B
chr3 (p21.1)
Scale
chr3:
100 kb
hg19
52,600,000
52,650,000
52,700,000
52,750,000
100
CNV gain frequency
0
100
CNV loss frequency
0
Chromosome Bands Localized by FISH Mapping Clones
3p21.1
Basic Gene Annotation Set from GENCODE Version 19 (coding transcripts - tsl1)
STAB1
PBRM1
SPCS1
NT5DC2
NT5DC2
GNL3
GLT8D1
SMIM4
GLT8D1
PBRM1
SPCS1
NEK4
PBRM1
PBRM1
PBRM1
PBRM1
PBRM1
PBRM1
GLT8D1
C
chr10 (q22.1)
Scale
chr10:
20 kb
hg19
70,670,000
70,680,000
70,690,000
70,700,000
70,710,000
70,720,000
70,730,000
70,740,000
100
CNV gain frequency
0
100
CNV loss frequency
0
Chromosome Bands Localized by FISH Mapping Clones
10q22.1
Basic Gene Annotation Set from GENCODE Version 19 (coding transcripts - tsl1)
DDX50
DDX21
D
chr12 (p13.31)
Scale
chr12:
50 kb
hg19
6,700,000
6,750,000
6,800,000
100
CNV gain frequency
0
100
CNV loss frequency
0
Chromosome Bands Localized by FISH Mapping Clones
12p13.31
Basic Gene Annotation Set from GENCODE Version 19 (coding transcripts - tsl1)
IFFO1
CHD4
ACRBP
ZNF384
NOP2
LPAR5
ING4
NOP2
ING4
NOP2
ING4
NOP2
ING4
CHD4
ING4
ING4
E
chr6 (p21.31)
Scale
chr6:
100 kb
hg19
34,250,000
34,300,000
34,350,000
34,400,000
100
CNA gain frequency
0
100
CNA loss frequency
0
Chromosome Bands Localized by FISH Mapping Clones
6p21.31
Basic Gene Annotation Set from GENCODE Version 19 (coding transcripts - tsl1)
HMGA1
NUDT3
RPS10
HMGA1
HMGA1
HMGA1
HMGA1
C6orf1
C6orf1

Figure S20. **UCSC Genome Browser views of basal G9a interactors whose encoding genes are located directly adjacent to one another or nearby, Related to Figure 7.**

(**A**) MRPS21 directly adjacent to PRPF3 (1q21.2 - 1q21.3), (**B**) PBRM1 directly adjacent to GNL3 (3p21.1), (**C**) DDX50 directly adjacent to DDX21 (10q22.1), (**D**) NOP2 directly adjacent to CHD4, with ZNF384 located nearby (12p13.31), (**E**) HMGA1 located near to RPS10 (6p21.31). The G9a interactor genes are displayed in red. Where included the gene annotation track is shown for the "Basic Gene Annotation Set from GENCODE Version 19" filtered to show protein coding transcripts with transcription support level 1 (tsl1). For each view the frequency of basal TCGA samples with copy number gain (segmentation mean > 0.1) (red) and copy number loss (segmentation mean < -0.1) (blue) is indicated.

Figure S21

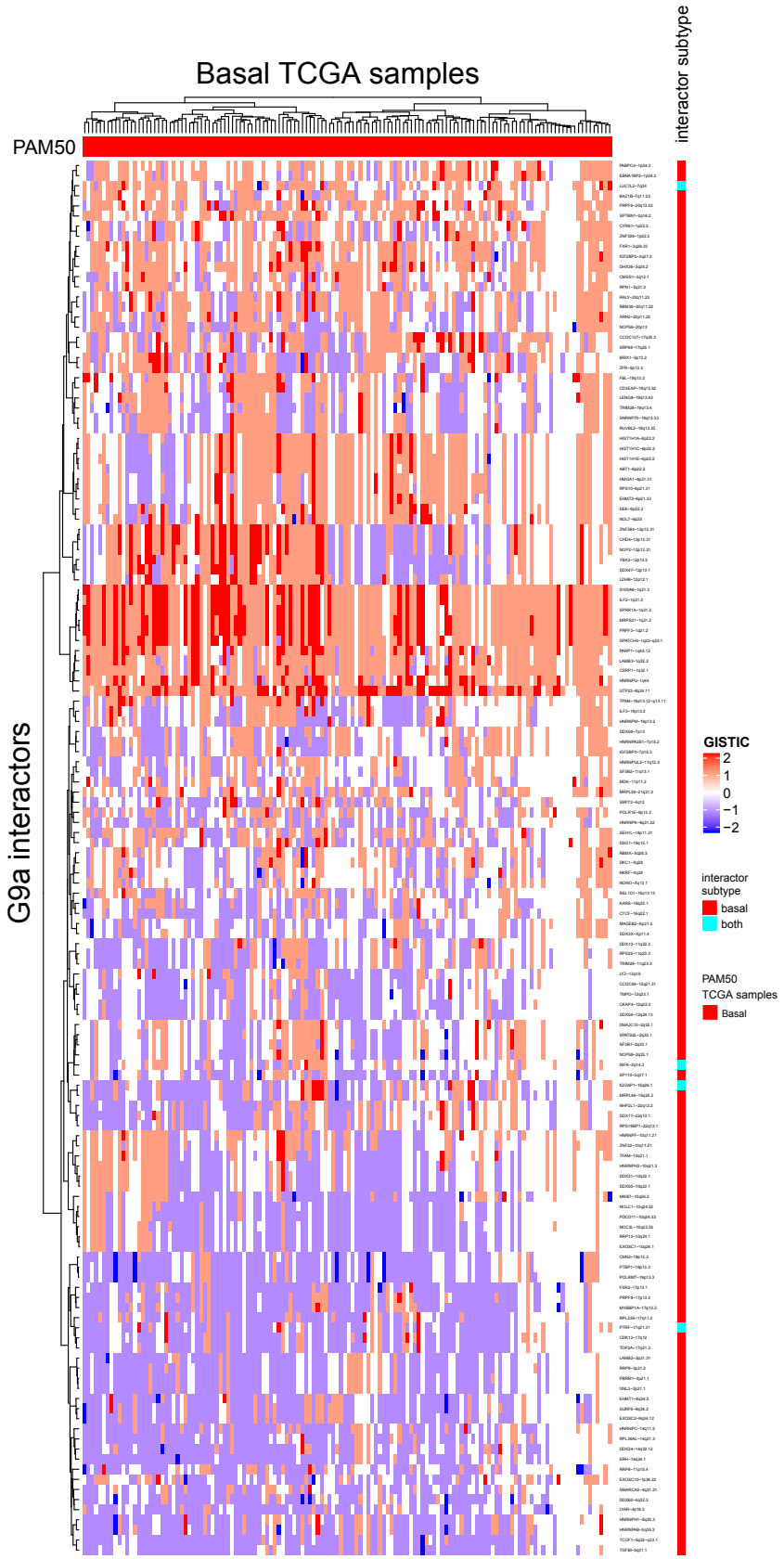

Figure S21. GISTIC copy number heatmap, Related to Figure 7.
Heatmap for basal G9a interactor genes (rows) with GISTIC copy number values from the TCGA sample set (columns). The TCGA samples and G9a interactor genes were clustered using unsupervised hierarchical clustering ("euclidean" distance and “ward” clustering method). The columns are annotated with PAM50 subtype of each TCGA patient. The rows are annotated with the proteomic subtype of G9a interactors.

TRANSPARENT METHODS

Chemicals and reagents. Antibodies against G9a (EHMT2) were from Abcam; antibodies against RBM47, NOP2, EBP2 (EBNA1BP2), TCOF1, ZNF326, DDX21, SF3B2, MKI67IP, BRIX1 (BXDV2), PTBP1, LYAR, and SMARCC1 were from Proteintech. Cell lines MCF10A, MCF7, MDA-MB-231, T47D, BT474, SUM159, and HCC1806 were purchased form ATCC (Manassas, VA). Human breast cancer frozen tissues with different receptor status were obtained from the Tissue Procurement Core Facility (TPF) at University of North Carolina.

Protein extraction. Cells were harvested at about 90% confluency. Each pellet of 10 million cells was homogenized in 10x cell pellet volume of hypotonic buffer (10 mM HEPES, pH 7.9, 1.5 mM $MgCl_2$, 10 mM KCl). After centrifugation for 10 min at 12,000 x g at 4^0C, the supernatant (cytosol) was discarded. The nuclear pellet was re-suspended in lysis buffer (50 mM Tris-HCl pH8.0, 150 mM NaCl, 0.5% CA630, protease inhibitor cocktail (Sigma-Aldrich), and 0.5 mM PMSF, sonicated and cleared by centrifugation for 20 min at 12000 x *g*. Protein concentration was determined by BCA assay. Frozen human tissue (approximately 0.1-0.2 g) was cut into small pieces and protein extraction was performed as above.

UNC0965 pull-down and ChaC sample processing. 1 mg nuclear protein extracted from either cell lines or clinical tissues was incubated overnight at 4°C with 2 nmole UNC0965 pre-coupled to 50 µl neutravidin-agarose (Thermo-Fisher), and washed three times with 1 ml lysis buffer to remove non-specific proteins. For on-beads sampling and processing, five additional washes with 50 mM Tris-HCl pH8.0, 150 mM NaCl were used to remove residual detergents. On-beads tryptic digestion was performed with 125 µl buffer containing 2 M urea, 50 mM Tris-HCl pH8.0, 1 mM DTT, 500 ng trypsin (Promega) for 30 min at room temperature on a mixer (Eppendorf). The tryptic digests were eluted twice with a 100 µl elution buffer containing 2 M urea, 50 mM Tris-HCl pH8.0, 5 mM iodoacetamide. Combined eluates were acidified with

trifluoroacetic acid at final concentration of 1% (TFA, mass spec grade, Thermo-Fisher) and desalted with a C18 stage tip.

LC-MS/MS analysis. Desalted peptide mixtures were dissolved in 30 µl 0.1% formic acid (Thermo-Fisher), of which 4 µl containing the peptides from 60-100 µg total protein was injected and analyzed by a ultra2D nanoLC system (Eksigent) coupled to a Velos LTQ Orbitrap mass spectrometer (Thermo Fisher Scientific, San Jose, CA) or an Easy nanoLC 1000 coupled to a Q-Exactive Orbitrap mass spectrometer (Thermo Fisher Scientific, San Jose, CA). In the nanoLC-Velos setup, peptides were first loaded on to a 2 mm × 0.5 mm reverse-phase (RP) C18 trap column (Eksigent) at a flow rate of 1 µl/min, then eluted, and fractionated on a 25 cm C18 RP column (25 cm × 75 µm ID, C18, 3 µm) with a gradient of 5-40% buffer B (ACN and 0.1% formic acid) at a constant flow rate of 250 nl/min over 180 min. In the Easy nanoLC- Q Exactive setup, peptides were loaded on to a 15 cm C18 RP column (15 cm × 75 µm ID, C18, 2 µm, Acclaim Pepmap RSLC, Thermo-Fisher) and eluted with a gradient of 2-30% buffer B at a constant flow rate of 300 nl/min for 70 min followed by 30% to 80% B in 5 min and 80% B for 10 min. The Velos LTQ Orbitrap was operated in the positive-ion mode with a data-dependent automatic switch between survey Full-MS scan (m/z 300-1800) (externally calibrated to a mass accuracy of <5 ppm and a resolution of 60,000 at *m/z* 400) and CID MS/MS acquisition of the top 15 most intense ions. The Q-Exactive was also operated in the positive-ion mode but with a data-dependent top 20 method. Survey scans were acquired at a resolution of 70,000 at m/z 200. Up to the top 20 most abundant isotope patterns with charge ≥ 2 from the survey scan were selected with an isolation window of 2.0 m/z and fragmented by HCD with normalized collision energies of 27. The maximum ion injection time for the survey scan and the MS/MS scans was 250 ms and 120 ms, respectively, and the ion target values were set to 1e6 and 2e5, respectively. Selected sequenced ions were dynamically excluded for 20 seconds.

Mass spec data and LFQ analysis. Mass spectral processing and peptide identification were performed on the Andromeda search engine in MaxQuant software (Version 1.5.2.8) against a human UniProt database. All searches were performed with a defined modification of cysteine carbamidomethylation, with methionine oxidation and protein amino-terminal acetylation as dynamic modifications. Peptides were confidently identified using a target-decoy approach with a peptide false discovery rate (FDR) of 1% and a protein FDR of 5%. A minimum peptide length of 7 amino acids was required, maximally two missed cleavages were allowed, initial mass deviation for precursor ion was up to 7 ppm, and the maximum allowed mass deviation for fragment ions was 0.5 Da.

LFQ-based LC-MS/MS experiments were performed with 2-3 biological replicates, each with three technical replicates, on two sets of seven BC cell lines of distinct PAM50-subtypes (luminal or BLBC/basal), or two tissue samples of the corresponding BC PAM50 subtypes paired with their adjacent non-malignant tissues. For LFQ analysis, a match between runs option was enabled and time window at 0.7 minutes. Data processing and statistical analysis were performed on Perseus (Version 1.5.1.6) (Cox and Mann, 2011). Protein quantitation was performed on biological replicate runs and a two sample t-test statistics was used with a p-value of 5% to report statistically significant expression fold-changes.

Analysis of functional category and networks of ISE-Interacting proteins. Similar to our recent report (Liu et al., 2014), the biological processes and molecular functions of the G9a-interacting proteins were categorized by IPA (http://www.ingenuity.com/), DAVID (http://david.abcc.ncifcrf.gov/), and STRING (http://string-db.org/).

TCGA and METABRIC data sets. All TCGA (Ciriello et al., 2015) and METABRIC (Curtis et al., 2012; Pereira et al., 2016) data used in our study were downloaded from the cBioPortal (Cerami et al., 2012; Gao et al., 2013) as files brca_tcga_pub2015.tar.gz for TCGA and

brca_metabric.tar.gz for METABRIC or retrieved by direct programmatic access from the cBioPortal using the 'cgdsr' R package (Jacobsen, 2015). For our analysis of TCGA data, we used complete samples with mutation, copy-number, and mRNA expression data provided (n = 816) from the TCGA cancer study brca_tcga_pub2015 (Breast Invasive Carcinoma) (Ciriello et al., 2015). The mRNA expression data set for G9a interactor genes was obtained from the data_RNA_Seq_v2_mRNA_median_Zscores.txt file (found in brca_tcga_pub2015.tar.gz), containing mRNA expression Z-scores compared with diploid tumors (diploid for each gene). The copy-number data set for G9a interactor genes was obtained from the data_CNA.txt file (found in brca_tcga_pub2015.tar.gz) for putative copy-number from GISTIC 2.0 for each gene. TCGA clinical data were obtained from the data_bcr_clinical_data_patient.txt and data_bcr_clinical_data_sample.txt files (found in brca_tcga_pub2015.tar.gz), which included overall survival data. Additional TCGA clinical information including the PAM50 subtype assigned to each patient was obtained from "Table S1" in the TCGA publication (Ciriello et al., 2015). For the METABRIC (Curtis et al., 2012; Pereira et al., 2016) data, we used: case list id = brca_metabric_cnaseq (samples with mRNA, GISTIC, mutational data) and gene profile = brca_metabric_mrna_U133_Zscores to retrieve clinical data and mRNA expression data programmatically from the cBioPortal. The METABRIC GISTIC data set was obtained from the data_CNA.txt file (found in brca_metabric.tar.gz). We used 1866 of the 2051 samples in the METABRIC case list for which there was survival data.

Heatmap construction. The heatmap of mRNA expression levels for G9a interactor genes from the TCGA BRCA datasets was constructed using the 'ComplexHeatmap' R package (Gu et al., 2016). Hierarchical clustering was performed using the euclidean distance method and the Ward clustering method (option ward.D2 in R's hclust function).

Statistical analyses. We used the Mann-Whitney-Wilcoxon Test with the wilcox.test function in R to determine significance for iCEP, mRNA vs. copy-number correlation, and mRNA vs. proliferation correlation. We used the Fisher's Exact Test for Count Data with the fisher.test function in R to determine significance for the copy-number amplification vs. proliferation correlation. For these tests, we included all genes in the TCGA data set (n = ~18,000) to obtain an adjusted p-value for multiple comparisons for the G9a interactor genes. The adjusted p-values were calculated by submitting all the p-values determined for each gene from the individual test to the p.adjust function in R using the 'fdr' method. We considered an adjusted p-value < 0.05 to be significant.

Kaplan-Meier survival analysis. Kaplan-Meier curve plotting and statistical analysis for differences of overall survival (OS) based on mRNA expression or GISTIC score of G9a interactor genes among TCGA and METABRIC BRCA samples were performed using the 'survival' R package (Therneau and Grambsch, 2000). Kaplan-Meier estimator and log-rank tests were performed using the survival functions Surv, survfit, and survdiff. Cox proportional hazard survival analysis was performed using the survival function coxph.

DATA AND SOFTWARE AVAILABILITY

The mass spectrometry proteomics data have been deposited to the ProteomeXchange Consortium via the PRIDE (Perez-Riverol et al., 2019) partner repository with the dataset identifier PXD013795. The files used for the analysis of the TCGA and METABRIC datasets are available online at Mendeley Data.

Supplemental References

Cox, J., and Mann, M. (2011). Quantitative, high-resolution proteomics for data-driven systems biology. Annual review of biochemistry *80*, 273-299.

Gu, Z., Eils, R., and Schlesner, M. (2016). Complex heatmaps reveal patterns and correlations in multidimensional genomic data. Bioinformatics (Oxford, England).

Jacobsen, A. (2015). cgdsr: R-Based API for Accessing the MSKCC Cancer Genomics Data Server (CGDS). R package version 1.2.5.

Perez-Riverol, Y., Csordas, A., Bai, J., Bernal-Llinares, M., Hewapathirana, S., Kundu, D.J., Inuganti, A., Griss, J., Mayer, G., Eisenacher, M.*, et al.* (2019). The PRIDE database and related tools and resources in 2019: improving support for quantification data. Nucleic acids research *47*, D442-D450.

Therneau, T.M., and Grambsch, P.M. (2000). Modeling survival data : extending the Cox model (New York: Springer).